

Unifying quantum heat transfer in a nonequilibrium spin-boson model with full counting statisticsChen Wang,^{1,*} Jie Ren,^{2,3,4,†} and Jianshu Cao^{5,‡}¹*Department of Physics, Hangzhou Dianzi University, Hangzhou, Zhejiang 310018, People's Republic of China*²*Center for Phononics and Thermal Energy Science, School of Physics Science and Engineering, Tongji University, 200092 Shanghai, People's Republic of China*³*China-EU Joint Center for Nanophonics, School of Physics Science and Engineering, Tongji University, 200092 Shanghai, People's Republic of China*⁴*Shanghai Key Laboratory of Special Artificial Microstructure Materials and Technology, School of Physics Science and Engineering, Tongji University, 200092 Shanghai, People's Republic of China*⁵*Department of Chemistry, Massachusetts Institute of Technology, 77 Massachusetts Avenue, Cambridge, Massachusetts 02139, USA*

(Received 12 December 2016; revised manuscript received 8 January 2017; published 13 February 2017)

To study the full counting statistics of quantum heat transfer in a driven nonequilibrium spin-boson model, we develop a generalized nonequilibrium polaron-transformed Redfield equation with an auxiliary counting field. This enables us to study the impact of qubit-bath coupling ranging from weak to strong regimes. Without external modulations, we observe maximal values of both steady-state heat flux and noise power in moderate coupling regimes, below which we find that these two transport quantities are enhanced by the finite-qubit-energy bias. With external modulations, the geometric-phase-induced heat flux shows a monotonic decrease upon increasing the qubit-bath coupling at zero qubit energy bias (without bias). While under the finite-qubit-energy bias (with bias), the geometric-phase-induced heat flux exhibits an interesting reversal behavior in the strong coupling regime. Our results unify the seemingly contradictory results in weak and strong qubit-bath coupling regimes and provide detailed dissections for the quantum fluctuation of nonequilibrium heat transfer.

DOI: [10.1103/PhysRevA.95.023610](https://doi.org/10.1103/PhysRevA.95.023610)**I. INTRODUCTION**

Efficient realization and smart control of quantum energy transfer are of fundamental importance in various fields, ranging from molecular electronics, to quantum heat engine, to quantum biology [1–5]. In particular, information and heat flow have been extensively studied in thermal functional devices, spawning phononics [6,7], where phonons are flexibly manipulated in analogy with electronic current in modern electronics [8–13]. In accordance with the second law of thermodynamics, it is known that heat energy will naturally transfer from a hot source to a cold drain driven by the thermodynamic bias (e.g., temperature), without an external driving field. Considering external modulations, the optimal mechanism of dynamical control can be unraveled in phononic thermal systems [14–17], even to pump heat against the temperature bias.

The prototype for describing nanoscale heat transfer mediated by quantum junctions is the nonequilibrium spin-boson (NESB) model [8,18], which was originally proposed in the study of quantum dissipation [19,20]. The NESB model is composed of a two-level system (i.e., qubit) interacting with two bosonic thermal baths under temperature bias. Many methods have been proposed to study the microscopic mechanism of quantum heat transfer in the NESB model. Particularly, the Redfield approach has been extensively applied to analyze the weak qubit-bath coupling regime, mainly due to the effective expression and clear physical picture [14,15]. The contribution of two thermal baths to the heat flux is additive,

which means that only incoherently sequential heat-exchange processes between the qubit and baths are considered. As such, the limitation of the Redfield approach is exposed in the strong qubit-bath coupling regime, where the heat flux is nonlinearly dependent on the system-bath coupling strength. In sharp contrast, the nonequilibrium noninteracting-blip approximation (NIBA) is applicable in the strong coupling limit to analytically treat multiphonon processes [9,21–23], where nonadditive and cooperative phonon transfer processes are included. Particularly, the appearance of turnover behavior of heat flux as a function of the qubit-bath coupling strength in the NESB model was confirmed by the NIBA, as well as by the multilayer multiconfiguration Hartree [24], quantum Monte Carlo schemes [18], and the nonequilibrium Green's function method [25–27]. Recently, the nonequilibrium polaron-transformed Redfield equation (NE-PTRE) has been proposed by the authors to analytically unify the steady-state heat flux in the weak and strong coupling limits, and the parity classified transfer processes have been unraveled [28].

From the dynamical control perspective, the time-dependent modulation of heat transfer in the NESB model has also attracted tremendous attention, enriching the transfer mechanisms [14–17,29–33]. The typical realization of the dynamical modulation is the adiabatic quantum pump, which was originally proposed by D. J. Thouless to study the effect of Berry-phase-induced quantization on closed-system transport [34]. In analogy, as the NESB model is adiabatically and periodically driven by control parameters (e.g., bath temperatures), a geometric-phase-induced heat flow will contribute to the heat transfer [15,16]. However, previous research unraveled the seemingly contradictory results that, in the weak qubit-bath coupling limit, the geometric-phase-induced heat flux remains finite, independent of the qubit-bath coupling strength under the unbiased condition [15], whereas

*wangchenyifang@gmail.com

†Xonics@tongji.edu.cn

‡jianshu@mit.edu

the counterpart in the strong coupling limit becomes strictly 0 [16]. The statement of seemingly contradiction or seemingly contradictory results below has the same meaning as expressed herein by default. Thus, natural questions are raised: What happens in the intermediate qubit-bath coupling regime? and Can we propose a theory to unify the geometric-phase-induced heat flux in the weak and strong coupling limits?

In the present paper, by including the full counting statistics, we introduce a generalized NE-PTRE to analyze the geometric-phase-induced heat flux in the NESB model. Our NE-PTRE is able to accommodate both the sequential transfer picture in the weak coupling limit and the multiphonon involved nonlinear collective transfer picture in the strong coupling regime. The geometric heat pump is investigated under both unbiased and biased conditions, and the seemingly contradictory results in the weak and strong coupling limits are clearly unified. Moreover, the effect of the qubit energy bias on the geometric heat pump is analyzed in typical system-bath coupling regimes. This work is organized as follows: in Sec. II, we introduce the NESB model and the NE-PTRE scheme that dissect the phonon transfer details. Then in Sec. III, by introducing the full counting statistics, we develop the generalized NE-PTRE and systematically analyze the counting measurements of NESB transport. In Sec. IV, first we investigate the steady-state heat flux and noise power as functions of the coupling strength and qubit energy bias. Then we focus on the geometric-phase-induced heat flux in both the unbiased and the biased cases, and comparisons with Redfield and nonequilibrium NIBA are clearly demonstrated. The final section (Sec. V) provides a concise summary.

II. NONEQUILIBRIUM SPIN-BOSON SYSTEM

A. Model

Following Ref. [28], the NESB model in Fig. 1, consisting of a two-level qubit coupled to two phononic thermal baths at different temperatures [8,15,18–20], is described as

$$\begin{aligned} \hat{H}_0 = & \frac{\epsilon_0}{2} \hat{\sigma}_z + \frac{\Delta}{2} \hat{\sigma}_x + \sum_{k;v=L,R} \omega_k \hat{b}_{k,v}^\dagger \hat{b}_{k,v} \\ & + \sum_{k;v=L,R} \hat{\sigma}_z (\lambda_{k,v} \hat{b}_{k,v}^\dagger + \lambda_{k,v}^* \hat{b}_{k,v}), \end{aligned} \quad (1)$$

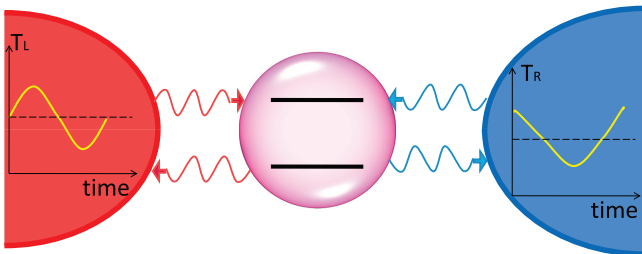


FIG. 1. Schematic of the nonequilibrium spin-boson model, composed of a central two-level qubit (purple circle) coupled to two individual thermal baths (red and blue regions), with temperatures T_L and T_R , respectively. Wavy red (blue) arrowed lines describe the interaction between the qubit and the L th (R th) bath. For the driven nonequilibrium spin-boson model, the system parameters appear to be time dependent, e.g., $T_L(t)$ and $T_R(t)$.

where the qubit is specified by the Pauli operators $\hat{\sigma}_z = |1\rangle\langle 1| - |0\rangle\langle 0|$ and $\hat{\sigma}_x = |1\rangle\langle 0| + |0\rangle\langle 1|$, with $|1(0)\rangle$ the excited (ground) state. ϵ_0 is the energy bias, and Δ is the tunneling strength between two states. $\hat{b}_{k,v}^\dagger$ ($\hat{b}_{k,v}$) creates (annihilates) one phonon with energy ω_k and momentum k in the v th bath, and $\lambda_{k,v}$ describes the coupling strength between the qubit and the v th bath.

To study the qubit-bath interaction beyond the weak coupling limit, it is helpful to transform the original Hamiltonian \hat{H}_0 in Eq. (1) under the polaron framework by $\hat{H} = \hat{U}^\dagger \hat{H}_0 \hat{U}$ [9,16,35], where the unitary operator is given by $\hat{U} = e^{i\hat{\sigma}_z \hat{B}/2}$, with the collective phononic momentum operator $\hat{B} = 2i \sum_{k;v=L,R} (\frac{\lambda_{k,v}}{\omega_k} \hat{b}_{k,v}^\dagger - \frac{\lambda_{k,v}^*}{\omega_k} \hat{b}_{k,v})$. Thus, the transformed Hamiltonian becomes $\hat{H} = \hat{H}_s + \hat{H}_b + \hat{V}_{sb}$. Specifically, the reorganized two-level qubit is shown as

$$\hat{H}_s = \frac{\epsilon_0}{2} \hat{\sigma}_z + \frac{\eta \Delta}{2} \hat{\sigma}_x, \quad (2)$$

where the renormalization factor is given by [9,16]

$$\begin{aligned} \eta = & \langle \cos \hat{B} \rangle \\ = & \exp \left(- \sum_v \int_0^\infty d\omega \frac{J_v(\omega)}{\pi \omega^2} [n_v(\omega) + 1/2] \right), \end{aligned} \quad (3)$$

with the v th bath spectral function $J_v(\omega) = 4\pi \sum_k |\lambda_{k,v}|^2 \delta(\omega - \omega_k)$, the Bose-Einstein distribution $n_v(\omega) = 1/[\exp(\beta_v \omega) - 1]$, and the inverse of the v th bath temperature $\beta_v = 1/k_B T_v$. The noninteracting phonon baths are characterized as $\hat{H}_b = \sum_{v=L,R} \hat{H}_v$, with $\hat{H}_v = \sum_k \omega_k \hat{b}_{k,v}^\dagger \hat{b}_{k,v}$. The qubit-bath interaction is expressed as

$$\hat{V}_{sb} = \frac{\Delta}{2} [(\cos \hat{B} - \eta) \hat{\sigma}_x + \sin \hat{B} \hat{\sigma}_y], \quad (4)$$

of which the thermal average vanishes, i.e., $\langle \hat{V}_{sb} \rangle = 0$. Hence, it may be appropriate to perturbatively obtain the equation of motion for the two-level qubit in the polaron picture. It should be noted that in many traditional approaches including many-phonon processes, e.g., the NIBA, the system-bath interaction $\hat{V} = \frac{\Delta}{2} (\cos \hat{B} \hat{\sigma}_x + \sin \hat{B} \hat{\sigma}_y)$ is directly perturbed [9,16]. However, actually \hat{V} should not be treated as a perturbation due to the nonnegligible contribution of $\langle \hat{V} \rangle \neq 0$. In contrast, $\hat{V}_{sb} = \hat{V} - \langle \hat{V} \rangle$ in Eq. (4) may be properly perturbed in accordance with the perturbation theory [28].

In this paper, the spectral function of phonon baths is characterized as $J_v(\omega) = \pi \alpha_v \omega^s \omega_{c,v}^{1-s} e^{-\omega/\omega_{c,v}}$, which is typically considered in quantum transfer studies of nanojunction systems [20,35–39]. α_v is the system-bath coupling strength of the order $\alpha_v \sim |\lambda_{k,v}|^2$, and $\omega_{c,v}$ is the cutoff frequency of the v th phonon bath. Without loss of generality, we consider the superohmic spectrum $s = 3$ in this study. Hence, the renormalization factor is specified as $\eta = \exp\{-\sum_{v=L,R} \alpha_v [-1 + \frac{2}{(\beta_v \omega_{c,v})^2} \psi_1(1/\beta_v \omega_{c,v})]/2\}$, with the trigamma function $\psi_1(x) = \sum_{n=0}^\infty \frac{1}{(n+x)^2}$. Moreover, in the weak coupling limit $\alpha_v \ll 1$, the normalization factor η becomes 1, while in the strong coupling regime $\alpha_v \gg 1$, it vanishes ($\eta = 0$).

B. Nonequilibrium polaron-transformed Redfield equation

We note that the PTRE method was originally developed to study quantum dissipative dynamics [35–38,40], with a single bath. Here we handle a system coupled to at least two baths at nonequilibrium. It is known that the reorganized system-bath interaction \hat{V}_{sb} can be treated as a perturbation [28]. Based on the Born-Markov approximation and the second-order perturbation theory, we obtain the NE-PTRE as

$$\frac{\partial \hat{\rho}}{\partial t} = -i[\hat{H}_s, \hat{\rho}] + \sum_{l=e,o} \sum_{\omega, \omega'=0, \pm\Lambda} \Gamma_l(\omega) [\hat{P}_l(\omega) \hat{\rho}, \hat{P}_l(\omega')] + \text{H.c.}, \quad (5)$$

where $\hat{\rho}$ is the reduced density matrix of the qubit in the polaron picture, $\Lambda = \sqrt{\epsilon_0^2 + \eta^2 \Delta^2}$ is the energy gap in the eigenbasis, and $\hat{P}_{e(o)}(\omega)$ is the eigenstate transition projector (see [41]), of which the relation to Pauli matrices is given by $\hat{\sigma}_{x(y)}(-\tau) = \sum_{\omega=0, \pm\Lambda} \hat{P}_{e(o)}(\omega) e^{i\omega\tau}$. The transition rates are

$$\Gamma_o(\omega) = \left(\frac{\eta\Delta}{2}\right)^2 \int_0^\infty d\tau e^{i\omega\tau} \sum_{n=0}^\infty \frac{Q(\tau)^{2n+1}}{(2n+1)!}, \quad (6)$$

$$\Gamma_e(\omega) = \left(\frac{\eta\Delta}{2}\right)^2 \int_0^\infty d\tau e^{i\omega\tau} \sum_{n=1}^\infty \frac{Q(\tau)^{2n}}{(2n)!}, \quad (7)$$

with the collective phonon propagator $Q(\tau) = \sum_{v=L,R} Q_v(\tau)$, and

$$Q_v(\tau) = \int_0^\infty d\omega \frac{J_v(\omega)}{\pi\omega^2} \{n_v(\omega) e^{i\omega\tau} + [1 + n_v(\omega)] e^{-i\omega\tau}\}. \quad (8)$$

From expressions of the correlation functions $\Gamma_{e(o)}(\omega)$, it is clearly shown that phonon transfer processes are classified by the even- and odd-parity contributions. Specifically, $\Gamma_o(\tau)$ describes the transfer processes including odd phonon numbers from two baths. The lowest order term $\Gamma_o^{(1)}(\omega)$ contains the terms $\frac{(\eta\Delta)^2}{8} [Q_L(\omega) + Q_R(\omega)]$, with the individual bath contribution $Q_v(\omega) = \int_{-\infty}^\infty d\tau e^{i\omega\tau} Q_v(\tau)$ at the transition energy $\omega = \pm\Lambda$, so that the lowest odd parity exhibits sequential-tunneling behavior depicted in Figs. 2(a) and 2(b) [8,15] while $\Gamma_e(\omega)$ shows cooperative heat transfer processes involving even phonon

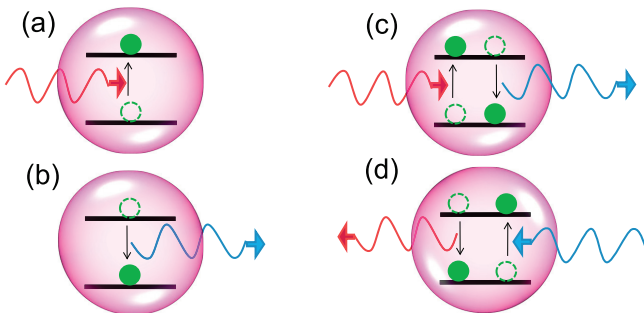


FIG. 2. Representative processes involving phonons in quantum heat transfer: (a), (b) single-phonon sequentially incoherent processes, $Q_L(\omega)$ and $Q_R(-\omega)$, respectively; (c), (d) two-phonon cotunneling processes, $Q_L(\omega)Q_R(-\omega)$ and $Q_R(\omega)Q_L(-\omega)$, respectively.

numbers. The corresponding lowest order even term $\Gamma_e^{(1)}(0)$ describes the cotunneling effect at Figs. 2(c) and 2(d) [42], which contains $\frac{(\eta\Delta)^2}{8\pi} \int_{-\infty}^\infty d\omega Q_L(\omega)Q_R(-\omega) = \frac{(\eta\Delta)^2}{8\pi} \int_0^\infty d\omega [Q_L(\omega)Q_R(-\omega) + Q_R(\omega)Q_L(-\omega)]$. This demonstrates the physical picture that as the left bath releases thermal energy ω , the right bath gains the equivalent quanta simultaneously, and the two-level system only has the virtual processes of excitation and relaxation so that it remains intact. Apparently, these contributions from two baths are involved nonadditively. Moreover, we can obtain an arbitrary order contribution to heat transfer processes systematically by applying the Taylor expansion.

Particularly, without bias ($\epsilon_0 = 0$) the steady-state densities can be obtained analytically in the local basis, where the diagonal and off-diagonal terms are [28]

$$P_{11} = P_{00} = 1/2, \quad (9)$$

$$P_{10} = P_{01} = \frac{1 \operatorname{Re}[\Gamma_o(-\Lambda)] - \operatorname{Re}[\Gamma_o(\Lambda)]}{2 \operatorname{Re}[\Gamma_o(-\Lambda)] + \operatorname{Re}[\Gamma_o(\Lambda)]}, \quad (10)$$

with the element $P_{ij} = \lim_{t \rightarrow \infty} \langle i | \hat{\rho}(t) | j \rangle$ ($|i\rangle$ depicts the qubit state), energy gap $\Lambda = \eta\Delta$, and $\operatorname{Re}[\Gamma_{o(e)}(\omega)]$ the real part of $\Gamma_{o(e)}(\omega)$.

III. FULL COUNTING STATISTICS OF THE NESB MODEL

We study the statistics of the transported heat $\Delta q_\tau = \sum_k \omega_k \Delta n_{k,v}$ in the NESB model, from the system to the v th phonon bath during a time interval τ , with $\Delta n_{k,v}$ the change in phonon number to the initial one with momentum k . The specific measurement of Δq_τ can be conducted as follows: Initially at time $t = 0$, we introduce a projector $\hat{K}_{q_0} = |q_0\rangle\langle q_0|$ to measure the quantity $\hat{H}_v = \sum_k \omega_k \hat{b}_{k,v}^\dagger \hat{b}_{k,v}$ in the v th bath, giving $q_0 = \sum_k \omega_k n_{k,v}(0)$. After a finite time τ of evolution of the system coupled to thermal baths, we again perform the projection $\hat{K}_{q_\tau} = |q_\tau\rangle\langle q_\tau|$ to obtain the measurement outcome $q_\tau = \sum_k \omega_k n_{k,v}(\tau)$. Hence, the number difference is given by $\Delta n_{k,v} = n_{k,v}(\tau) - n_{k,v}(0)$. Meanwhile, the joint probability of measuring q_0 at $t = 0$ and q_τ at $t = \tau$ is defined as [43]

$$\operatorname{Pr}[q_\tau, q_0] = \operatorname{Tr}_{s,b} \{ \hat{K}_{q_\tau} e^{-i\hat{H}_0\tau} \hat{K}_{q_0} \hat{\rho}_0 \hat{K}_{q_0} e^{i\hat{H}_0\tau} \hat{K}_{q_\tau} \}, \quad (11)$$

with the trace over both the qubit and the thermal baths. Based on the joint probability $\operatorname{Pr}[q_\tau, q_0]$, we introduce the probability of measuring Δq_τ during the time interval τ as

$$\operatorname{Pr}_\tau(\Delta q_\tau) = \sum_{q_\tau, q_0} \delta(\Delta q_\tau - (q_\tau - q_0)) \operatorname{Pr}[q_\tau, q_0]. \quad (12)$$

Then the cumulant generating function of the statistics can be defined as

$$G_\tau(\chi) = \ln \int d\Delta q_\tau \operatorname{Pr}_\tau(\Delta q_\tau) e^{i\chi \Delta q_\tau}, \quad (13)$$

with χ the counting-field parameter.

To quantitatively express the cumulant generating function, we introduce the NE-PTRE accompanied by the full counting statistics. Assuming that the quantum system is connected to two baths (labeled L and R), we measure the transported heat from the system to the R th bath, in the context of the χ -dependent NE-PTRE. Then we add the counting projector

to the Hamiltonian \hat{H}_0 in Eq. (1) to generate $\hat{H}_0(\chi) = e^{i\chi\hat{H}_R/2}\hat{H}_0e^{i\chi\hat{H}_R/2}$ [43,44], written as

$$\hat{H}_0(\chi) = \frac{\epsilon_0}{2}\hat{\sigma}_z + \frac{\Delta}{2}\hat{\sigma}_x + \sum_{k,v=L,R} \omega_k \hat{b}_{k,v}^\dagger \hat{b}_{k,v} + \sum_{k,v=L,R} \hat{\sigma}_z (e^{i\chi\omega_k\delta_{v,R}/2} \lambda_{k,v} \hat{b}_{k,v}^\dagger + \text{H.c.}). \quad (14)$$

Similarly to the transformation scheme in the NE-PTRE [28], we perform a generalized polaron transformation resulting in $\hat{H}_\chi = \hat{U}_\chi^\dagger \hat{H}_0(\chi) \hat{U}_\chi$, with the unitary operator $U_\chi = e^{i\hat{\sigma}_z \hat{B}_\chi/2}$ and χ -dependent phonon collective momentum $\hat{B}_\chi = 2i \sum_{k,v} (e^{i\chi\omega_k\delta_{v,R}/2} \frac{\lambda_{k,v}}{\omega_k} \hat{b}_{k,v}^\dagger - \text{H.c.})$. As such, the transformed Hamiltonian is expressed as $\hat{H}_\chi = \hat{H}_s + \hat{H}_b + \hat{V}_{sb}(\chi)$. Particularly, the reorganized qubit-bath coupling is modified by the counting field as

$$\hat{V}_{sb}(\chi) = \frac{\Delta}{2} [(\cos \hat{B}_\chi - \eta)\hat{\sigma}_x + \sin \hat{B}_\chi \hat{\sigma}_y], \quad (15)$$

which includes both the information on the counting measurement and the multiphonon nonlinear processes. Whereas \hat{H}_s and \hat{H}_b remain unchanged, it should be noted that the thermal average of the interaction term vanishes $\langle \hat{V}_{sb}(\chi) \rangle = 0$ due to the parity symmetry. Moreover, the magnitude of the second-order correlated contribution of $\hat{V}_{sb}(\chi)$ is quite small, compared to \hat{H}_s at Eq. (2). Hence, the perturbation of $\hat{V}_{sb}(\chi)$ can be properly carried out, like the derivation of Eq. (5). Considering the Born-Markov approximation, we perturb $\hat{V}_{sb}(\chi)$ up to second order and obtain the generalized NE-PTRE in the context of full counting statistics,

$$\frac{\partial \hat{\rho}_\chi}{\partial t} = -i[\hat{H}_s, \hat{\rho}_\chi] + \sum_{l=e,0} \sum_{\omega, \omega'=\pm\Lambda} \{[\Gamma_{l,-}^\chi(\omega) + \Gamma_{l,+}^\chi(\omega')] \times \hat{P}_l(\omega') \hat{\rho}_\chi \hat{P}_l(\omega) - [\Gamma_{l,+}(\omega) \hat{P}_l(\omega') \hat{P}_l(\omega) \hat{\rho}_\chi + \text{H.c.}]\}, \quad (16)$$

where $\hat{\rho}_\chi$ is the reduced two-level system (qubit) density operator under the counting field, $\hat{P}_l(\omega)$ is the eigenstate transition projector [41], and the energy gap is $\Lambda = \sqrt{\epsilon_0^2 + \eta^2 \Delta^2}$. The transition rates are expressed as

$$\Gamma_{e,\sigma}^\chi(\omega) = \left(\frac{\eta\Delta}{2}\right)^2 \int_0^\infty d\tau e^{i\omega\tau} [\cosh Q(\sigma\tau - \chi) - 1], \quad (17)$$

$$\Gamma_{o,\sigma}^\chi(\omega) = \left(\frac{\eta\Delta}{2}\right)^2 \int_0^\infty d\tau e^{i\omega\tau} \sinh Q(\sigma\tau - \chi), \quad (18)$$

where the modified single-phonon propagator becomes $Q(\tau - \chi) = Q_L(\tau) + Q_R(\tau - \chi)$.

IV. RESULTS AND DISCUSSION

In this section, we apply the generalized nonequilibrium polaron-transformed Redfield equation with an auxiliary counting field, to study the steady-state heat transfer, as well as the geometric-phase-induced heat transfer under adiabatic time-dependent modulations.

A. Steady-state heat transfer

By rearranging the NE-PTRE in the Liouville space [28], the equation of motion for the two-level qubit in Eq. (16) is expressed as

$$\frac{\partial}{\partial t} |\rho_\chi\rangle = -\hat{\mathcal{L}}_\chi |\rho_\chi\rangle, \quad (19)$$

where the vector form of the density matrix is $|\rho_\chi\rangle = [P_{11}^\chi, P_{00}^\chi, P_{10}^\chi, P_{01}^\chi]^T$ with $P_{ij}^\chi = \langle i | \hat{\rho}_\chi | j \rangle$, and $\hat{\mathcal{L}}_\chi$ is the Liouvillian superoperator. In the absence of the counting-field parameter ($\chi = 0$), the element of the density operator P_{ij}^χ reduces to the conventional P_{ij} . Based on the dynamical equation, (19), the reduced density matrix at time t is given by $|\rho_\chi(t)\rangle = \exp(-\hat{\mathcal{L}}_\chi t) |\rho_\chi(0)\rangle$, with $|\rho_\chi(0)\rangle$ the initial state. Hence, the cumulant function can be expressed as $\mathcal{Z}_\chi(t) = \langle \mathbb{I} | \rho_\chi(t) \rangle$ [44], with the unit vector defined as $\langle \mathbb{I} | = [1, 1, 0, 0]$. Consequently, the cumulant generating function after long-time evolution can be obtained by $G_t(\chi) = \frac{1}{t} \ln \mathcal{Z}_\chi(t)$, and the corresponding n th cumulant of heat current fluctuations can be generated as $J^{(n)}(t) = \langle \hat{Q}^n \rangle / t = \frac{\partial^n G_t(\chi)}{\partial (i\chi)^n} |_{\chi=0}$. When external modulation is absent, i.e., \mathcal{L}_χ is time independent, if we focus on the steady-state solution, the cumulant generating function is simplified to $G(\chi) = -E_0(\chi)$, where $E_0(\chi)$ is the ground-state energy of the superoperator $\hat{\mathcal{L}}_\chi$. The corresponding left and right eigenvectors are denoted $\langle \Phi_\chi |$ and $|\Psi_\chi\rangle$, which fulfill the normalization relation $\langle \Phi_\chi | \Psi_\chi \rangle = 1$. In particular, the steady-state heat flux is the first cumulant $J = -\frac{\partial E_0(\chi)}{\partial (i\chi)} |_{\chi=0}$, and the noise power is the second cumulant $J^{(2)} = -\frac{\partial^2 E_0(\chi)}{\partial (i\chi)^2} |_{\chi=0}$.

1. Unbiased condition: $\epsilon_0 = 0$

We first investigate the steady-state heat transfer in Fig. 3, where the system parameters are time independent. Without bias ($\epsilon_0 = 0$), the authors have shown in Ref. [28] that the heat flux can be analytically solved over a wide system-bath coupling regime by applying the NE-PTRE.

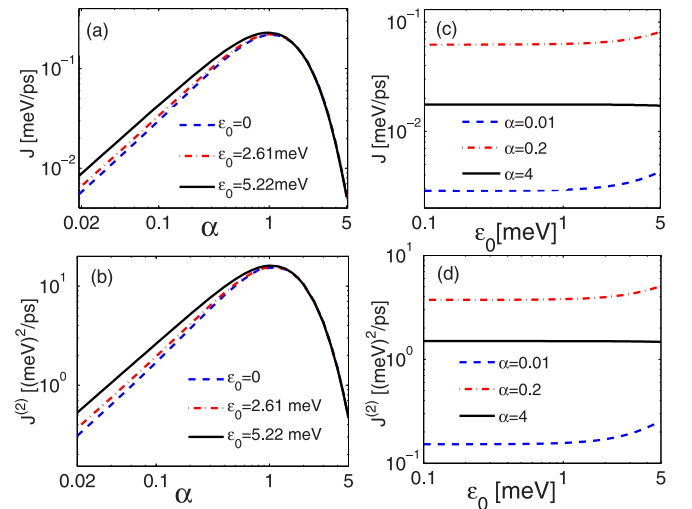


FIG. 3. Behaviors of the steady-state heat flux and noise power: (a), (b) with varying system-bath coupling strengths and (c), (d) with tuning of the qubit energy bias, respectively. Other parameters are $\Delta = 5.22$ meV, $\omega_c = 26.1$ meV, $T_L = 150$ K, and $T_R = 90$ K.

Here, we show the full counting statistics of heat transfer at steady state by analytically exhibiting the counting field based on the cumulant generating function (G_χ). Since G_χ corresponds to the ground-state energy ($E_0(\chi) = -G_\chi$), based on the analysis in Appendix A, we obtain the ground eigensolution in Liouville space as

$$E_0(\chi) = (X_e - X_e^\chi) + \frac{Y - \sqrt{Y^2 - (X_o^\chi)^2 + (X_o)^2}}{2}. \quad (20)$$

The contributing term from the even parity is

$$X_e^\chi = \Gamma_{e,+}^\chi(0) + \Gamma_{e,-}^\chi(0), \quad (21)$$

and $X_e = X_e^\chi|_{\chi=0}$, with the transition rate $\Gamma_{l,\sigma}^\chi(\omega)$ given in Eq. (16). The terms from the odd parity are given by

$$Y_\chi = \sum_{\sigma=\pm, \omega=\pm\Lambda} \Gamma_{o,\sigma}^\chi(\omega), \quad (22)$$

$$X_o^\chi = \sum_{\sigma=\pm, \omega=\pm\Lambda} \text{sgn}(\omega)\sigma \Gamma_{o,\sigma}^\chi(\omega), \quad (23)$$

with $\text{sgn}(\pm\Lambda) = \pm 1$ and $\Lambda = \eta\Delta$. $Y = Y_\chi|_{\chi=0}$ and $X_o = X_o^\chi|_{\chi=0}$. Consequently, the heat flux can be expressed as

$$J = \frac{\Lambda^2}{8\pi} \int_{-\infty}^{\infty} \left[\frac{\text{Re}[\Gamma_o(\Lambda)]C_o(-\Lambda, \omega') + \text{Re}[\Gamma_o(-\Lambda)]C_o(\Lambda, \omega')}{\text{Re}[\Gamma_o(\Lambda)] + \text{Re}[\Gamma_o(-\Lambda)]} + C_e(0, \omega') \right] \omega' d\omega', \quad (24)$$

$$J^{(2)} = \frac{\Lambda^2}{8\pi} \left\{ \int_{-\infty}^{\infty} d\omega \left[\frac{\text{Re}[\Gamma_o(-\Lambda)]C_o(\Lambda, \omega) + \text{Re}[\Gamma_o(\Lambda)]C_o(-\Lambda, \omega)}{\text{Re}[\Gamma_o(\Lambda)] + \text{Re}[\Gamma_o(-\Lambda)]} + C_e(0, \omega) \right] \omega^2 - \frac{\int_{-\infty}^{\infty} d\omega [C_o(\Lambda, \omega) - C_o(-\Lambda, \omega)] \omega}{(\text{Re}[\Gamma_o(\Lambda)] + \text{Re}[\Gamma_o(-\Lambda)])^3} [\text{Re}[\Gamma_o(-\Lambda)]^2 \int_{-\infty}^{\infty} \frac{d\omega}{\pi} C_o(\Lambda, \omega) \omega - \text{Re}[\Gamma_o(\Lambda)]^2 \int_{-\infty}^{\infty} \frac{d\omega}{\pi} C_o(-\Lambda, \omega) \omega] \right\}. \quad (27)$$

We find that the first term on the right-hand side of Eq. (27) is the main contribution to the shot noise, of which the spectral distribution is the same as that for the heat flux in Eq. (24). Hence, the nonmonotonic turnover behavior is quite similar to the heat flux, as shown in Fig. 3(b).

2. Biased condition: $\epsilon_0 \neq 0$

Next, we extend our analysis of steady-state behaviors to the biased condition ($\epsilon_0 \neq 0$). The heat flux shows the same nonmonotonic turnover behavior as α increases, i.e., the flux increases in the weak and moderate coupling strength regimes ($\alpha \lesssim 1$) and decreases in the strong coupling regimes ($\alpha \gtrsim 1$), shown in Fig. 3(a). Interestingly, in the weak coupling regime ($\alpha \lesssim 1$), the heat flux is enhanced by enlarging the qubit energy bias ϵ_0 , whereas as the coupling strength enters into the strong regime ($\alpha \gtrsim 1$), the heat flux remains constant for changing energy bias. To confirm these results, we select typical coupling strengths to clearly demonstrate the influence of the energy bias on the heat flux, in Fig. 3(c).

Moreover, we look into the second-cumulant heat fluctuation, i.e., the noise power, in Fig. 3(b). Similarly to the steady-state flux, the shot noise of the heat flux also exhibits the same turnover behavior. As the system-bath coupling strength increases, the noise power is enhanced by the energy bias in

where the rate probability densities are specified as

$$C_e(\omega, \omega') = \int_{-\infty}^{\infty} d\chi e^{-i\chi\omega'} \int_{-\infty}^{\infty} d\tau e^{i\omega\tau} [\cosh Q(\tau - \chi) - 1], \quad (25)$$

$$C_o(\omega, \omega') = \int_{-\infty}^{\infty} d\chi e^{-i\chi\omega'} \int_{-\infty}^{\infty} d\tau e^{i\omega\tau} \sinh Q(\tau - \chi) \quad (26)$$

at energy $\omega = 0, \pm\Lambda$. This analytical expression, Eq. (24), of the steady-state heat flux without bias is found to be identical to the counterpart in Ref. [28]; the turnover behavior of the coupling strength is exhibited in Fig. 3(a) (dashed blue line). Physically, $C_e(0, \omega')$ and $C_o(\pm\Lambda, \omega')$ describe the even- and odd-parity components of the transfer process, respectively. For example, $C_o(\Lambda, \omega')$ describes the process in which the qubit releases energy Λ by relaxing from the excited eigenstate to the ground one, so that the right bath absorbs energy ω' and the left one obtains the left $\Lambda - \omega'$. As such, the number of the state change of the qubit is odd, e.g., n times excitation and $n + 1$ times relaxation lead to a relaxation as the final action. And $C_e(0, \omega')$ describes the process where the qubit has an even number of virtual state changes, i.e., n times relaxation and n times excitation, so that the central qubit remains intact and undergoes no energy change. But still, the right bath absorbs energy ω' and the left bath gains $-\omega'$ (i.e., releases ω').

Similarly, the shot noise is obtained as

the weak coupling regime, whereas the noise power becomes nearly independent of the bias in the strong coupling regime. These behaviors are clearly depicted in Fig. 3(d). Therefore, we conclude that both the steady-state heat flux and the noise power are tuned in a similar way by either qubit-bath coupling or qubit energy bias.

B. Geometric-phase-induced heat flux

As the system is periodically driven by external fields, e.g., modulated by two bath temperatures $T_{L(R)}(t)$, as schematically shown in Fig. 1, the Liouville superoperator becomes time dependent $\hat{\mathcal{L}}_\chi(t)$. The effect of the geometric phase will additionally contribute to the heat flux [15,16,45–48], demonstrated in Appendix B. Thus, in the adiabatic modulation limit, there clearly exist two components making up the generating function as

$$\lim_{t \rightarrow \infty} \mathcal{Z}_\chi(t) = e^{G_\chi t} = \exp([G_{\text{dyn}}(\chi) + G_{\text{geom}}(\chi)]t), \quad (28)$$

Specifically, the average dynamical phase is expressed as $G_{\text{dyn}}(\chi) = -\frac{1}{T_p} \int_0^{T_p} dt E_0(\chi, t)$, where T_p is the driving period, and $E_0(\chi, t)$ is the eigenvalue of $\hat{\mathcal{L}}_\chi(t)$ with the minimal real part. It results in the dynamical heat flux $J_{\text{dyn}} = \frac{\partial}{\partial(i\chi)} G_{\text{dyn}}(\chi)|_{\chi=0}$. The geometric phase contribution

of the generating function is described by Eq. (B9) in Appendix B,

$$G_{\text{geom}}(\chi) = -\frac{1}{T_p} \int_0^{T_p} dt \langle \Phi_\chi(t) | \frac{\partial}{\partial t} | \Psi_\chi(t) \rangle, \quad (29)$$

where $|\Psi_\chi(t)\rangle$ ($\langle \Phi_\chi(t) |$) is the corresponding right (left) eigenvector of $E_0(\chi, t)$. Assuming that the two system parameters $u_1(t)$ and $u_2(t)$ are periodically modulated [which are two driving bath temperatures $T_{L(R)}(t)$ in this work], the geometric phase in Eq. (29) is specified as $G_{\text{geom}}(\chi) = -\frac{1}{T_p} \oint [du_1 \langle \Phi_\chi | \frac{\partial}{\partial u_1} | \Psi_\chi \rangle + du_2 \langle \Phi_\chi | \frac{\partial}{\partial u_2} | \Psi_\chi \rangle]$. According to the Stocks theorem, $G_{\text{geom}}(\chi)$ can be reexpressed as

$$G_{\text{geom}}(\chi) = -\frac{1}{T_p} \iint_{u_1, u_2} du_1 du_2 \mathcal{F}_\chi(u_1, u_2), \quad (30)$$

where

$$\mathcal{F}_\chi(u_1, u_2) = \langle \partial_{u_1} \Phi_\chi | \partial_{u_2} \Psi_\chi \rangle - \langle \partial_{u_2} \Phi_\chi | \partial_{u_1} \Psi_\chi \rangle. \quad (31)$$

It is noteworthy [49] that $\mathcal{F}_\chi(u_1, u_2)$ has the meaning of curvature in the parameter space (u_1, u_2) of the ground state of the quantum Liouville superoperator $\hat{\mathcal{L}}_\chi$. It is of pure geometric interpretation and independent of the driving speed (in the adiabatic limit). Mathematically, $G_{\text{geom}}(\chi)$ is an analog of the adiabatic Berry phase in quantum mechanics [50], where in the latter case the wave function obtains an extra phase after a cyclic evolution. Similarly, in the full counting statistics of our driven systems, the cumulant generating function $G_{\text{geom}}(\chi)$ (analog of phase) in the exponent of the characteristic function \mathcal{Z}_χ (analog of wave function) also obtains an additional term. Both extra terms share a similar geometric origin from the nontrivial curvature in the system's parameter space. As such $\mathcal{F}_\chi(u_1, u_2)$ is a Berry-like curvature and we term $G_{\text{geom}}(\chi)$ the geometric phase contribution, which generates the n th cumulant of the geometric-phase-induced heat current fluctuation, as [15,16,45]

$$\begin{aligned} J_{\text{geom}}^{(n)} &= \left. \frac{\partial^n G_{\text{geom}}(\chi)}{\partial (i\chi)^n} \right|_{\chi=0} \\ &= -\frac{1}{T_p} \iint_{u_1, u_2} du_1 du_2 \frac{\partial^n}{\partial (i\chi)^n} \mathcal{F}_\chi(u_1, u_2) \Big|_{\chi=0}. \end{aligned} \quad (32)$$

The geometric heat flux is given by the first cumulant $J_{\text{geom}} = J_{\text{geom}}^{(1)}$.

1. Unbiased condition: $\epsilon_0 = 0$

Here, we first investigate the geometric heat flux without bias ($\epsilon_0 = 0$). It is known that in the weak qubit-bath coupling regime, the geometric-phase-induced heat flux is finite and independent of the coupling strength [15]. This mainly results from the fact that with weak qubit-bath coupling the transition rates between the two-level qubit and the phononic baths are linearly dependent on the coupling strength, exhibiting additive transfer processes. On the contrary, the geometric heat flux vanishes in the strong qubit-bath coupling regime upon applying the nonequilibrium NIBA method [16]. The left and right eigenvectors corresponding to the ground-state energy are given by $|\Psi_\chi\rangle = \frac{1}{2}[1, 1, 0, 0]^T$ and $\langle \Phi_\chi | = [1, 1, 0, 0]$, which are clearly independent of the system parameters and result in the zero geometric heat flux according to Eq. (30). It was proposed

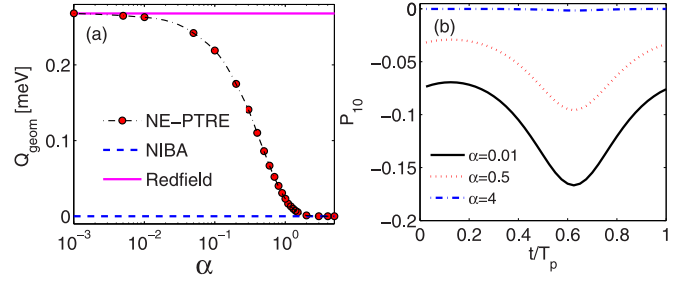


FIG. 4. Adiabatic modulation by two bath temperatures without bias ($\epsilon_0 = 0$): (a) geometric-phase-induced heat pump $Q_{\text{geom}} = J_{\text{geom}} * T_p$; (b) coherence (P_{10}) in the local basis. The two bath temperatures are specified as $T_L(\tau) = (150 + 90 \cos \Omega_p \tau)$ K and $T_R(\tau) = (150 + 90 \sin \Omega_p \tau)$ K, with the period $T_p = 1$ ns. Other parameters are $\Delta = 5.22$ meV and $\omega_c = 26.1$ meV.

that these two approaches describe different physical pictures within the same NESB system and do not conflict with each other [16,28].

Based on the χ -dependent NE-PTRE, Eq. (16), we try to explicitly unify these limiting results, as shown in Fig. 4(a). In the weak system-bath coupling regime, the geometric heat flux approaches the upper limit within the Redfield scheme. As the coupling strength increases, the geometric heat flux is strongly suppressed and asymptotically decreases to 0, which finally becomes identical to the result in the nonequilibrium NIBA. The underlying mechanism can be understood by analyzing the coherence $P_{10}(t)$, since the populations (P_{00}, P_{11}) are constant. We find in Fig. 4(b) that the coherence is suppressed monotonically by increasing the qubit-bath coupling strength, finally resulting in the constant quasi-steady state in the strong coupling limit [16]. It is proposed that without bias ($\epsilon_0 = 0$), multiphonon processes degrade the formation of the geometric phase. Therefore, this seeming contradiction is clearly solved within the framework of the NE-PTRE accompanied by a counting field.

Moreover, compared to the dynamical heat flux [28], the system-bath coupling plays a distinct role in the geometric heat flux. For the dynamical flux, in the weak and intermediate coupling regimes, multiphonon processes are helpful in generating steady-state heat flux, mainly due to the robustness of the transition rates. However, in the strong coupling limit, the large system-bath interaction weakens the transition rates due to the quantum Zeno-like effect and, finally, suppresses the heat flux. Hence, the nonmonotonic behavior of the dynamical heat flux is clearly demonstrated. For geometric flux, increasing the system-bath coupling strength will only monotonically decrease the geometric heat flux, which implies that the instantaneous state of the qubit is inclined to remain intact, which is independent of temperature modulations, as we have discussed above.

2. Biased condition: $\epsilon_0 \neq 0$

Next, we analyze the geometric heat flux under finite energy bias ($\epsilon_0 \neq 0$), as shown in Fig. 5(a). In the weak coupling limit, the geometric heat flux is equal to that from the Redfield scheme. The existence of coherence P_{10} is also crucial to enhance the geometric-phase-induced heat flux, which is similar to the unbiased case in Fig. 4. As the coupling strength

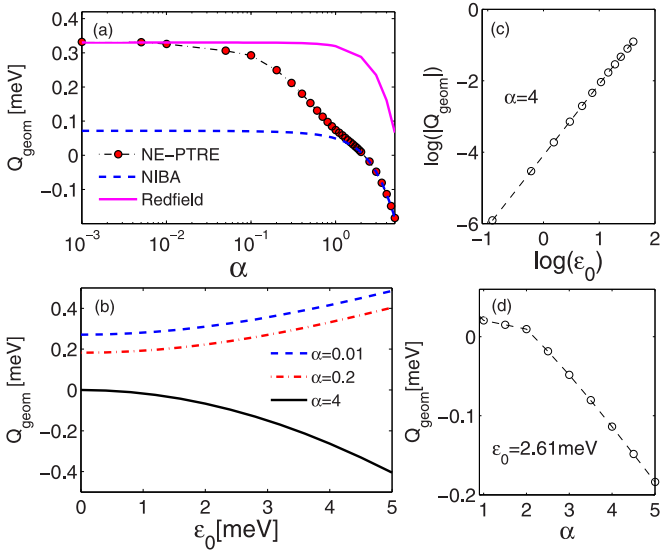


FIG. 5. (a) Geometric-phase-induced heat pump $Q_{\text{geom}} = J_{\text{geom}} \times T_p$ under finite energy bias of the qubit ($\epsilon_0 = 2.61$ meV); (b) influence of the qubit energy bias on the geometric-phase-induced heat pump, with modulation of the two bath temperatures; (c) log-log relation between ϵ_0 and Q_{geom} in the strong coupling regime ($\alpha = 4$); (d) linear relation between Q_{geom} and α in the strong coupling regime. Parameters are the same as in Fig. 4.

increases, the geometric heat flux decreases sharply and even becomes negative. The corresponding coherence is strongly suppressed, which leaves only the populations to contribute to the geometric heat flux. Then the behavior of the geometric heat flux is consistent with the result within the nonequilibrium NIBA in the strong coupling regime [16]. As a result, we conclude that the NE-PTRE is also applicable to unify limiting coupling results beyond the unbiased condition.

Next, we turn to analyze the influence of the qubit energy bias on the geometric heat pump in Fig. 5(b). In the weak qubit-bath coupling regime (e.g., $\alpha = 0.01$), the geometric heat pump shows monotonic enhancement with an increase in the energy bias. As the interaction strength is modulated to the intermediate coupling regime (e.g., $\alpha = 0.2$), the geometric heat pump is also positively enhanced by the increasing energy bias, which is similar to the counterpart in the weak coupling case. If we further increase the coupling strength (e.g., $\alpha = 4$), the geometric heat pump becomes negatively enhanced, which is quantitatively distinct from that in the weak coupling regime. This observation clearly demonstrates different physical pictures in these two limiting interaction regimes.

We admit that it is beyond our ability to analytically provide a comprehensive picture in a wide system-bath coupling regime for the biased case. Here, to understand the geometric heat flux reversal, we focus on the strong interaction limit, which is consistent with the nonequilibrium NIBA framework. Combined with the counting field, the equation of motion for the qubit is expressed as

$$\frac{d}{dt} \begin{pmatrix} P_{11}^{\chi} \\ P_{00}^{\chi} \end{pmatrix} = - \begin{pmatrix} K(\epsilon_0) & -K_-(\chi) \\ -K_+(\chi) & K(-\epsilon_0) \end{pmatrix} \begin{pmatrix} P_{11}^{\chi} \\ P_{00}^{\chi} \end{pmatrix}, \quad (33)$$

with the population $P_{ii}^{\chi} = \langle i | \hat{\rho}_{\chi}(t) | i \rangle$. The transition rates are given by

$$K^{\pm}(\chi) = (\Delta/2)^2 \int_{-\infty}^{\infty} dt \eta^2 e^{\pm i\epsilon_0 t + Q_L(t) + Q_R(t-\chi)}, \quad (34)$$

with $K(\pm\epsilon_0) = K_{\pm}(\chi)|_{\chi=0}$, η and $Q_v(t)$ given in Eq. (3) and Eq. (8), respectively. Thus, the eigenstate energies are directly obtained as

$$E_{\pm}(\chi) = \frac{1}{2} \{ [K(\epsilon_0) + K(-\epsilon_0)] \pm \sqrt{[K(\epsilon_0) - K(-\epsilon_0)]^2 + 4K_+(\chi)K_-(\chi)} \}. \quad (35)$$

The corresponding right eigenstates are given by

$$|\Psi_{\chi}^{\pm}\rangle = [2K_-(\chi), A_{\pm}(\chi)]^T, \quad (36)$$

with the coefficients $A_{\pm}(\chi) = [K(\epsilon_0) - K(-\epsilon_0)] \mp \sqrt{[K(\epsilon_0) - K(-\epsilon_0)]^2 + 4K_+(\chi)K_-(\chi)}$. Accordingly, the left eigenstates are

$$\langle \Phi_{\chi}^{\pm} | = \frac{[2K_+(\chi), A_{\pm}(\chi)]}{A_{\pm}^2(\chi) + 4K_+(\chi)K_-(\chi)}. \quad (37)$$

In the strong qubit-bath coupling limit, it is known that the Marcus approximation becomes applicable [9,51]. Marcus's theory was originally proposed for the electron transfer rate in the donor-acceptor species. And it works at high temperatures $k_B T > \epsilon_0$ and/or the strong qubit-bath coupling regime [52]. It can be approached by the short-time expansion of $Q_v(t)$ in Eq. (8) as $Q_v(t) = \frac{\Gamma_v T_v}{\omega_{c,v}^2} - \Gamma_v T_v t^2 - i\Gamma_v t$ [54], with the effective coupling strength $\Gamma_v = \int \frac{J_v(\omega)}{\pi\omega} d\omega = 2\alpha_v \omega_{c,v}$. Consequently, the transition rates combined with the counting parameter are simplified as $K_{\pm}(\chi) = K(\pm\epsilon_0)M_{\pm}(\chi)$, with the standard rates

$$K(\pm\epsilon_0) = \frac{\Delta^2}{4} \sqrt{\frac{\pi}{\Gamma_L T_L + \Gamma_R T_R}} \exp \left[-\frac{(\epsilon_0 \mp \Gamma_L \mp \Gamma_R)^2}{4(\Gamma_L T_L + \Gamma_R T_R)} \right] \quad (38)$$

and the factor

$$M_{\pm}(\chi) = e^{\pm i\epsilon_0 \chi - \frac{\Gamma_L T_L \Gamma_R T_R}{\Gamma_L T_L + \Gamma_R T_R} [i\chi(\frac{1}{T_L} + \frac{\pm\epsilon_0 - \Gamma_R}{\Gamma_R T_R}) + \chi^2]}. \quad (39)$$

In the absence of the counting field ($\chi = 0$), the factor $M_{\pm}(\chi = 0) = 1$, and the modified transition rates $K_{\pm}(\chi)$ decrease back to the standard expressions $K(\pm\epsilon_0)$ in Eq. (38), respectively. Moreover, we consider the weak qubit energy bias regime, i.e., $\epsilon_0 \ll \{\Gamma_v, k_B T_v\}$. Then the transition rate in Eq. (38) can be approximately expanded up to first order of ϵ_0 as

$$K(\pm\epsilon_0) \approx K_0 \left[1 \pm \frac{\epsilon_0}{2(\Gamma_L T_L + \Gamma_R T_R)} (\Gamma_L + \Gamma_R) \right], \quad (40)$$

with $K_0 = \frac{\Delta^2}{4} \sqrt{\frac{\pi}{\Gamma_L T_L + \Gamma_R T_R}} \exp[-\frac{(\Gamma_L + \Gamma_R)^2}{4(\Gamma_L T_L + \Gamma_R T_R)}]$. According to the definition in Eq. (32), the geometric-phase-induced heat flux is obtained as

$$J_{\text{geom}} = -\frac{\epsilon_0^2}{T_p} \iint_{T_L, T_R} dT_L dT_R \frac{\Gamma_L \Gamma_R (\Gamma_L + \Gamma_R)^3}{8(\Gamma_L T_L + \Gamma_R T_R)^4}. \quad (41)$$

This expression clearly confirms the reversal (negative) behavior of the heat flux in the strong coupling limit, shown in Fig. 5(a). Moreover, the power-law feature of the energy bias

is analytically exhibited in Eq. (41), which is in excellent agreement with the numerical result as $J_{\text{geom}} \sim -\epsilon_0^{2.0 \pm 0.02}$, shown in Fig. 5(c). If the system-bath couplings are identically selected as $\alpha_L = \alpha_R = \alpha$, the geometric heat flux is expressed as $J_{\text{geom}} \sim -\alpha\epsilon_0^2$ based on Eq. (41), and numerically confirmed in Fig. 5(d), which coincides with the numerical results in Fig. 2 of Ref. [16], that J_{geom} is linearly dependent on the coupling strength α and quadratically dependent on the qubit energy bias ϵ_0 .

V. CONCLUSION

In summary, we have investigated the geometric-phase-induced heat pump in the nonequilibrium spin-boson model by periodically modulating the temperatures of two thermal baths, which is beyond the traditional Redfield and nonequilibrium NIBA schemes. With the development of the nonequilibrium polaron-transformed Redfield equation (NE-PTRE) approach in the context of full counting statistics, the cumulant generating function is clearly demonstrated; it consists of both dynamical phase and geometric phase contributions. In the absence of an external driving field, the influences of qubit energy bias on the steady-state heat flux and the corresponding noise power have been analyzed. In the weak and moderate coupling regimes, the energy bias monotonically enhances both the steady state heat flux and the noise power, while in the strong coupling regime, these two observables become independent of the energy bias. This clearly demonstrates the same role of the energy bias in affecting the heat flux and the noise power.

Next, we have analyzed the geometric heat pump without bias by varying the qubit-bath coupling strength over a wide regime. In the weak system-bath coupling limit, the geometric heat flux is positive finite, which is equivalent to the counterpart within the Redfield scheme [15]. As the coupling strength increases, the geometric heat flux shows a monotonic decrease and, finally, approaches strictly 0, which is identical to the result based on the nonequilibrium NIBA [16]. We have also studied the geometric heat pump under the biased condition. We found that the geometric heat pump decreases quickly as the qubit-bath coupling increases and shows reversal behavior in the strong coupling regime. Moreover, the analytical relations of the geometric heat flux with the system-bath coupling and the energy bias have been obtained. The results based on the NE-PTRE also show consistency with the counterparts from the Redfield and nonequilibrium NIBA schemes, in the weak and strong coupling regimes, respectively.

Therefore, we conclude that this unified theory is applicable to obtain the geometric heat flux in the nonequilibrium spin-boson model, under both unbiased and biased conditions. Moreover, we have analyzed the influence of the qubit energy bias on the geometric heat pump. The geometric heat flux is negatively enhanced in the strong qubit-bath coupling regime, which is in sharp contrast with its counterpart in the weak coupling case, exhibiting positive stabilization. We hope that these results will have broad implications for smart control of energy transfer in low-dimensional nanodevices.

ACKNOWLEDGMENTS

C.W. is supported by the National Natural Science Foundation of China under Grants No. 11547124 and No. 11574052. J.R. acknowledges the National Youth 1000 Talents Program in China and the 985 startup grant (No. 205020516074) at Tongji University.

APPENDIX A: ANALYTICAL EXPRESSION OF THE STEADY-STATE CUMULANT GENERATING FUNCTION WITHOUT BIAS

Without bias ($\epsilon_0 = 0$), the Liouvillian dynamics of the reduced density matrix in Eq. (19) under the framework of full counting statistics is expressed as $\frac{d}{dt}|\rho_\chi\rangle = -\hat{L}_\chi|\rho_\chi\rangle$, where the evolution matrix is specified as

$$\hat{L}_\chi = \begin{pmatrix} a & -a_\chi & b_\chi & c_\chi \\ -a_\chi & a & c_\chi & b_\chi \\ d_\chi & e_\chi & a & f_\chi \\ e_\chi & d_\chi & f_\chi & a \end{pmatrix}. \quad (\text{A1})$$

The matrix elements are written as $a_\chi = X_e^\chi + \frac{Y_\chi}{2}$, $b_\chi = -\frac{1}{2}(X_{o,+}^\chi + X_{o,-}^\chi)$, $c_\chi = \frac{1}{2}(X_{o,+}^\chi + X_{o,-}^\chi)$, $d_\chi = \frac{1}{2}(X_{o,+}^\chi - X_{o,-}^\chi)$, $e_\chi = \frac{1}{2}(X_{o,+}^\chi - X_{o,-}^\chi)$, $f_\chi = -X_e^\chi + \frac{Y_\chi}{2}$, and $a = a_\chi|_{\chi=0}$, with the coefficients

$$X_e^\chi = \Gamma_{e,+}^\chi(0) + \Gamma_{e,-}^\chi(0), \quad (\text{A2})$$

$$Y_\chi = \Gamma_{o,+}^\chi(\Lambda) + \Gamma_{o,+}^\chi(-\Lambda) + \Gamma_{o,-}^\chi(\Lambda) + \Gamma_{o,-}^\chi(-\Lambda), \quad (\text{A3})$$

$$X_{o,\pm}^\chi = \Gamma_{o,\pm}^\chi(\Lambda) - \Gamma_{o,\pm}^\chi(-\Lambda), \quad (\text{A4})$$

and $X_{o,\pm} = X_{o,\pm}^\chi|_{\chi=0}$. The modified transition rates $\Gamma_{e(o)}^\chi(\omega)$ are shown in Eq. (16).

To find the eigenvalues of the evolution matrix, we set $\det(\mathbf{L}_\chi - \lambda\mathbf{I}) = 0$, which results in

$$(a - \lambda)^2 = (a_\chi f_\chi + b_\chi d_\chi + c_\chi e_\chi) \pm [(a_\chi - f_\chi)(a - \lambda) + (c_\chi d_\chi + b_\chi e_\chi)]. \quad (\text{A5})$$

For one branch, the solution is given by

$$\lambda_\pm^p = (X_e - X_e^\chi) + \frac{Y}{2} \mp \sqrt{Y_\chi^2 - (X_{o,+}^\chi - X_{o,-}^\chi)^2 + (X_{o,+} - X_{o,-})^2}/2, \quad (\text{A6})$$

and for the other branch, it is given by

$$\lambda_\pm^m = (X_e + X_e^\chi) + \frac{Y}{2} \mp \sqrt{Y_\chi^2 - (X_{o,+}^\chi + X_{o,-}^\chi)^2 + (X_{o,+} + X_{o,-})^2}/2. \quad (\text{A7})$$

Hence, the ground-state energy is obtained as $E_0(\chi) = \lambda_+^p$. Since the cumulant generating function is given by $G_\chi = -E_0(\chi)$, it is specified as

$$G_\chi = (X_e^\chi - X_e) - \frac{Y}{2} + \sqrt{Y_\chi^2 - (X_{o,+}^\chi)^2 + (X_{o,-})^2}/2, \quad (\text{A8})$$

with $X_o^\chi = X_{o,+}^\chi - X_{o,-}^\chi$ and $X_o = X_o^\chi|_{\chi=0}$.

APPENDIX B: INTRODUCTION OF THE GEOMETRIC PHASE AND CUMULANT GENERATING FUNCTION

Considering the time-dependent superoperator $\hat{L}_\chi(t)$ with the counting parameter, which is not Hermitian, we obtain the quasi-eigensolution as

$$\begin{aligned}\hat{L}_\chi(t)|\psi_n(\chi,t)\rangle &= E_n(\chi,t)|\psi_n(\chi,t)\rangle, \\ \langle\phi_n(\chi,t)|\hat{L}_\chi(t) &= \langle\phi_n(\chi,t)|E_n(\chi,t),\end{aligned}\quad (\text{B1})$$

where $\lambda_n(\chi,t)$ is the instantaneous eigenvalue of $\hat{L}_\chi(t)$, and $|\psi_n(\chi,t)\rangle$ ($\langle\phi_n(\chi,t)|$) is the corresponding normalized right (left) eigenvector, which obeys the relation $\langle\phi_n(\chi,t)|\psi_m(\chi,t)\rangle = \delta_{n,m}$. In analogy with the seminal Berry's solution, we can express the wave function in the basis $\{|\psi_n(\chi,t)\rangle\}$ as

$$|\rho_\chi(t)\rangle = \sum_n a_n(t) \exp\left[-\int_0^t E_n(\chi,\tau)d\tau\right]|\psi_n(\chi,t)\rangle. \quad (\text{B2})$$

By substituting Eq. (B2) into the dynamical equation, (19), we obtain the evolution equation of $a_n(t)$:

$$\begin{aligned}\sum_n \frac{da_n(t)}{dt} \exp\left[-\int_0^t E_n(\chi,\tau)d\tau\right]|\psi_n(\chi,t)\rangle \\ = -\sum_n a_n(t) \exp\left[-\int_0^t E_n(\chi,\tau)d\tau\right]\left|\frac{d}{dt}\psi_n(\chi,t)\right\rangle.\end{aligned}\quad (\text{B3})$$

Then, by left-multiplying the eigenvector $\langle\phi_m(\chi,t)|$ by Eq. (B3), we find that

$$\begin{aligned}\frac{da_m(t)}{dt} = -a_m(t)\left\langle\phi_m(\chi,t)\left|\frac{d}{dt}\psi_m(\chi,t)\right.\right\rangle \\ - \sum_{n \neq m} a_n(t) \exp\left(-\int_0^t [E_n(\chi,\tau) - E_m(\chi,\tau)]d\tau\right) \\ \times \left\langle\phi_m(\chi,t)\left|\frac{d}{dt}\psi_n(\chi,t)\right.\right\rangle.\end{aligned}\quad (\text{B4})$$

It should be noted that the eigenvalue $E_n(\chi,t)$ generally is a complex value. Hence, the long-time behavior of the reduced qubit system is mastered by only the eigenmode $m=0$, of which the eigenvalue $E_0(\chi,t)$ owns the smallest real part.

In the adiabatic limit, the second term on the right-hand side of Eq. (B4) can be approximately ignored due to the decay factor $\exp(-\int_0^t [E_n(\chi,\tau) - E_0(\chi,\tau)]d\tau)$ ($\text{Re}[E_n(\chi,\tau) - E_0(\chi,\tau)] > 0$ for $n \neq 0$). We obtain the expression of $a_n(t)$ after long-time evolution ($t \rightarrow \infty$) as

$$a_0(t) = \exp\left(-\int_0^t \left\langle\phi_0(\chi,\tau)\left|\frac{d}{d\tau}\psi_0(\chi,\tau)\right.\right\rangle d\tau\right)a_0(0), \quad (\text{B5})$$

with $a_0(0)$ the initial-state coefficient. Then, if we consider the adiabatic cyclic evolution over a long time period T_p , the wave function can be specified as

$$\begin{aligned}|\rho_\chi(t)\rangle = \exp\left(-\frac{t}{T_p} \int_0^{T_p} d\tau \left[E_0(\chi,\tau) \right. \right. \\ \left. \left. + \left\langle\phi_0(\chi,\tau)\left|\frac{d}{d\tau}\psi_0(\chi,\tau)\right.\right\rangle\right]\right)a_0(0)|\rho_\chi(0)\rangle.\end{aligned}\quad (\text{B6})$$

Consequently, the generating function can be obtained as

$$\begin{aligned}\mathcal{Z}_\chi(t) = \langle\mathbb{I}|\rho_\chi(t)\rangle \\ \approx \exp\left(-\frac{t}{T_p} \int_0^{T_p} d\tau \left[E_0(\chi,\tau) \right. \right. \\ \left. \left. + \left\langle\phi_0(\chi,\tau)\left|\frac{d}{d\tau}\psi_0(\chi,\tau)\right.\right\rangle\right]\right)a_0(0)\langle\mathbb{I}|\rho_\chi(0)\rangle.\end{aligned}\quad (\text{B7})$$

Finally, the cumulant generating function in the long-time limit can be described by two contributing terms as

$$G(\chi) = \lim_{t \rightarrow \infty} \frac{\ln \mathcal{Z}_\chi(t)}{t} = G_{\text{dyn}}(\chi) + G_{\text{geom}}(\chi), \quad (\text{B8})$$

and the factor $\lim_{t \rightarrow \infty} \frac{1}{t} \ln(a_0(0)\langle\mathbb{I}|\rho_\chi(0)\rangle)$ becomes negligible. Here, $G_{\text{dyn}}(\chi)$ is the dynamical phase factor, written as $G_{\text{dyn}}(\chi) = -\frac{1}{T_p} \int_0^{T_p} E_0(\chi,\tau)d\tau$, while $G_{\text{geom}}(\chi)$ originates from the geometric phase contribution, written as $G_{\text{geom}}(\chi) = -\frac{1}{T_p} \int_0^{T_p} \langle\phi_0(\chi,\tau)\left|\frac{d}{d\tau}\psi_0(\chi,\tau)\right.\rangle d\tau$. In the text, we use $|\Psi_\chi(t)\rangle$ ($\langle\Phi_\chi(t)|$) in Eq. (29) to replace $|\psi_0(\chi,t)\rangle$ ($\langle\phi_0(\chi,t)|$). The geometric-phase-induced cumulant generating function is reexpressed as

$$G_{\text{geom}}(\chi) = -\frac{1}{T_p} \int_0^{T_p} \left\langle\Phi_\chi(\tau)\left|\frac{d}{d\tau}\Psi_\chi(\tau)\right.\right\rangle d\tau. \quad (\text{B9})$$

-
- [1] Y. Dubi and M. Di Ventra, *Rev. Mod. Phys.* **83**, 131 (2011).
[2] M. A. Ratner, *Nat. Nanotechnol.* **8**, 378 (2013).
[3] P. Nalbach and M. Thorwart, *Proc. Natl. Acad. Sci. USA* **110**, 2693 (2013).
[4] M. Mohseni, Y. Omar, G. S. Engel, and M. B. Plenio, *Quantum Effects in Biology* (Cambridge University Press, Cambridge, UK, 2014).
[5] D. Z. Xu and J. S. Cao, *Front. Phys.* **11**, 110308 (2016).
[6] N. B. Li, J. Ren, L. Wang, G. Zhang, P. Hänggi, and B. W. Li, *Rev. Mod. Phys.* **84**, 1045 (2012).
[7] J. Ren and B. W. Li, *AIP Adv.* **5**, 053101 (2015).
[8] D. Segal and A. Nitzan, *Phys. Rev. Lett.* **94**, 034301 (2005).
[9] D. Segal, *Phys. Rev. B* **73**, 205415 (2006).
[10] C. W. Chang, D. Okawa, A. Majumdar, and A. Zettl, *Science* **314**, 1121 (2006).
[11] L. Wang and B. W. Li, *Phys. Rev. Lett.* **99**, 177208 (2007).
[12] L. F. Zhang, J. Ren, J. S. Wang, and B. W. Li, *Phys. Rev. Lett.* **105**, 225901 (2010).
[13] E. Taylor and D. Segal, *Phys. Rev. Lett.* **114**, 220401 (2015).
[14] D. Segal, *Phys. Rev. Lett.* **101**, 260601 (2008).
[15] J. Ren, P. Hanggi, and B. W. Li, *Phys. Rev. Lett.* **104**, 170601 (2010).
[16] T. Chen, X. B. Wang, and Jie Ren, *Phys. Rev. B* **87**, 144303 (2013).
[17] C. Uchiyama, *Phys. Rev. E* **89**, 052108 (2014).
[18] K. Saito and T. Kato, *Phys. Rev. Lett.* **111**, 214301 (2013).
[19] A. J. Leggett, S. Chakravarty, A. T. Dorsey, M. P. A. Fisher, A. Garg, and W. Zwerger, *Rev. Mod. Phys.* **59**, 1 (1987).
[20] U. Weiss, *Quantum Dissipative Systems* (World Scientific, Singapore, 2008).
[21] L. Nicolin and D. Segal, *J. Chem. Phys.* **135**, 164106 (2011).
[22] L. Nicolin and D. Segal, *Phys. Rev. B* **84**, 161414 (2011).

- [23] D. Segal, *Phys. Rev. E* **90**, 012148 (2014).
- [24] L. A. Velizhanin, H. Wang, and M. Thoss, *Chem. Phys. Lett.* **460**, 325 (2008).
- [25] J. J. Liu, H. Xu, and C. Q. Wu, *Chem. Phys.* **481**, 42 (2016).
- [26] J. J. Liu, H. Xu, B. W. Li, and C. Q. Wu, *arXiv:1609.05598*.
- [27] B. K. Agarwalla and D. Segal, *arXiv:1612.01008*.
- [28] C. Wang, J. Ren, and J. S. Cao, *Sci. Rep.* **5**, 11787 (2015).
- [29] S. Gasparinetti, P. Solinas, A. Braggio, and M. Sassetti, *New J. Phys.* **16**, 115001 (2014).
- [30] G. Guarnieri, C. Uchiyama, and B. Vacchini, *Phys. Rev. A* **93**, 012118 (2016).
- [31] J. Cerrillo, M. Buser, and T. Brandes, *Phys. Rev. B* **94**, 214308 (2016).
- [32] M. Carrega, P. Solinas, M. Sassetti, and U. Weiss, *Phys. Rev. Lett.* **116**, 240403 (2016).
- [33] L. Ferialdi, *Phys. Rev. A* **95**, 020101(R) (2017).
- [34] D. J. Thouless, *Phys. Rev. B* **27**, 6083 (1983).
- [35] A. Nazir, *Phys. Rev. Lett.* **103**, 146404 (2009).
- [36] S. Jang, Y. C. Cheng, D. R. Reichman, and J. D. Eaves, *J. Chem. Phys.* **129**, 101104 (2008).
- [37] P. Nalbach, J. Eckel, and M. Thorwart, *New J. Phys.* **12**, 065043 (2010).
- [38] C. K. Lee, J. M. Moix, and J. S. Cao, *J. Chem. Phys.* **142**, 164103 (2015).
- [39] D. Z. Xu, C. Wang, Y. Zhao, and J. S. Cao, *New J. Phys.* **18**, 023003 (2016).
- [40] R. J. Silbey and T. Harris, *J. Chem. Phys.* **80**, 2615 (1984).
- [41] In the eigenbasis $\{| \pm \rangle\}$ with $\hat{H}_s | \pm \rangle = \pm \Lambda/2 | \pm \rangle$, the transition projectors are given by $\hat{P}_e(\Lambda) = \cos \theta | + \rangle \langle - |$, $\hat{P}_e(0) = \sin \theta (| + \rangle \langle + | - | - \rangle \langle - |)$, $\hat{P}_e(-\Lambda) = \cos \theta | - \rangle \langle + |$, $\hat{P}_o(\Lambda) = -i | + \rangle \langle - |$, $\hat{P}_o(0) = 0$, and $\hat{P}_o(-\Lambda) = i | - \rangle \langle + |$, with $\theta = \tan^{-1}(\eta \Delta / \epsilon_0)$.
- [42] T. Ruokola and T. Ojanen, *Phys. Rev. B* **83**, 045417 (2011).
- [43] M. Esposito, U. Harbola, and S. Mukamel, *Rev. Mod. Phys.* **81**, 1665 (2009).
- [44] M. Campisi, P. Hanggi, and P. Talkner, *Rev. Mod. Phys.* **83**, 771 (2011).
- [45] N. A. Sinitsyn and I. Nemenman, *Europhys. Lett.* **77**, 58001 (2007).
- [46] N. A. Sinitsyn and I. Nemenman, *Phys. Rev. Lett.* **99**, 220408 (2007).
- [47] T. Sagawa and H. Hayakawa, *Phys. Rev. E* **84**, 051110 (2011).
- [48] T. Yuge, T. Sagawa, A. Sugita, and H. Hayakawa, *Phys. Rev. B* **86**, 235308 (2012).
- [49] J. Ren, S. Liu, and B. Li, *Phys. Rev. Lett.* **108**, 210603 (2012).
- [50] M. V. Berry, *Proc. R. Soc. London A* **392**, 45 (1984).
- [51] R. A. Marcus, *J. Chem. Phys.* **24**, 966 (1956).
- [52] We note that the Marcus theory not only is valid in the high-temperature (classic) limit $k_B T > \omega_c$, but also is valid in the relative “high” -temperature regime $\omega_c > k_B T > \epsilon_0$ (high compared to the qubit’s energy scale). Under the latter regime, both the thermal fluctuation ($-\Gamma_v T_v t^2$) and the quantum dissipation ($-i\Gamma_v t$) terms of the correlation function $Q_v(t)$ coexist, which forms the basis of our discussion. Therefore, the Marcus theory can be carried out in this whole regime “ $k_B T > \epsilon_0$ ” in our work. Related discussions can also be found preceding Eq. (37) in Ref. [21], following Eq. (18) in Ref. [22], and in subsection 5.2 in Ref. [53].
- [53] L. A. Pachón and P. Brumer, *Phys. Chem. Chem. Phys.* **14**, 10094 (2012).
- [54] Please note here that $Q_v(t)$ is different from the expression used in Ref. [16] and in Ref. [9]. This is caused by the renormalization factor η we extracted. They are consistent when we consider η .

Non-canonical distribution and non-equilibrium transport beyond weak system-bath coupling regime: A polaron transformation approach

Dazhi Xu, Jianshu Cao[†]

Department of Chemistry, Massachusetts Institute of Technology, Cambridge, MA 02139, USA

Corresponding author. E-mail: [†]jianshu@mit.edu

Received October 12, 2015; accepted February 2, 2016

The concept of polaron, emerged from condense matter physics, describes the dynamical interaction of moving particle with its surrounding bosonic modes. This concept has been developed into a useful method to treat open quantum systems with a complete range of system-bath coupling strength. Especially, the polaron transformation approach shows its validity in the intermediate coupling regime, in which the Redfield equation or Fermi's golden rule will fail. In the polaron frame, the equilibrium distribution carried out by perturbative expansion presents a deviation from the canonical distribution, which is beyond the usual weak coupling assumption in thermodynamics. A polaron transformed Redfield equation (PTRE) not only reproduces the dissipative quantum dynamics but also provides an accurate and efficient way to calculate the non-equilibrium steady states. Applications of the PTRE approach to problems such as exciton diffusion, heat transport and light-harvesting energy transfer are presented.

Keywords polaron transformation, strong coupling, quantum transport, non-equilibrium steady state

PACS numbers 71.38.-k, 66.10.C-, 05.60.Gg, 05.70.Ln

Contents		5.3 Energy transfer via three-level heat engine model	
1	Introduction	1	12
2	Polaron transformation of the spin-boson model	3	6 Summary
3	Equilibrium distribution of the SBM via the polaron approach	4	Acknowledgements
3.1	Accuracy of the perturbation theory in the polaron frame	4	Appendix A Correlation functions in Eq. (18)
3.2	Non-canonical equilibrium distribution	6	Appendix B Redfield tensor in Eqs. (42) and (43)
4	Polaron transformed Redfield equation	7	Appendix C Details in non-equilibrium energy flux of Eq. (48)
4.1	Steady states and equilibrium distribution	7	References
4.2	Validity of the PTRE	8	
4.3	Weak and strong coupling limits	8	
5	Applications of PTRE to exciton diffusion, heat transport and energy transfer	9	
5.1	Coherent exciton transport in disordered systems	9	
5.2	Non-equilibrium heat transfer through quantum dot	10	

*Special Topic: Progress in Open Quantum Systems: Fundamentals and Applications.

property of equilibrium states and the negligible back action from the system to the bath. In this case, the second-order perturbation theory leads to a master equation of the Redfield or the Lindblad type [1–4], which is convenient for analytical investigation and not computationally expensive for numerical implementation. However, in many physical systems of current interest, the system-bath coupling (SBC) is comparable to the system internal couplings, hence the weak coupling approximation is not justified. The typical examples are the excitation energy transfer process in solid quantum dots [5, 6] and photosynthetic complexes [7–10]. There are a number of non-perturbative techniques to obtain the numerically exact dynamics; examples include the hierarchy master equation [11, 12], the quasi-adiabatic propagator path integral (QUAPI) [13], the density matrix renormalization group [14], the numerical renormalization group [15], the multi-configuration time-dependent Hartree approach [16, 17] and the stochastic path integrals [18, 19]. However, these methods are computationally demanding and non-trivial to implement for large systems. In addition, much of the recent efforts focus on the short-time non-Markovian dynamics (i.e., dynamical coherence), which is relevant for laser-induced coherence but not for the long-time behavior.

Therefore, we need a method which is formally simple and physically transparent, meanwhile goes beyond weak SBC regime without losing accuracy. Polaron, a basic concept in condensed matter physics, which describes the quantum (quasi-) particle interacting with the deformed lattices through electromagnetic interaction [20, 21] (as illustrated in Fig. 1), is exploited to achieve this goal. Initiated by Silbey and coworkers, a variational polaron transformation method was applied to study the bath renormalisation effects on the tunneling matrix elements in the spin-boson model (SBM) [22, 23]. Further, this approach is used to investigate the excitation migration in molecular crystals, covering both the coherent and incoherent transport preterites [24]. Recently, a polaron transformed second-order master equation has been derived to study the dynamics of open quantum

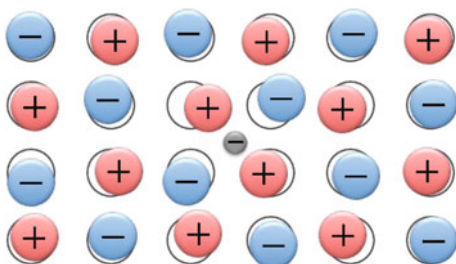


Fig. 1 Illustration of polaron formed with a charged particle surrounded by a polarized crystal medium.

systems at strong coupling [25–28]. This approach extends the regime of validity of the master equation to stronger system-bath couplings, provided that the internal couplings (or tunneling matrix elements) are small compared to the typical bath frequency (i.e., the bath response is fast on the system time-scale). The main idea of the polaron transformation approach is to describe the system in the polaron frame such that the system is dressed by the environment. The dressed system (or polaron) takes the major effects of the system-bath interaction into consideration, hence the reduced SBC is weakened to the regime that the second-order perturbation theory is applicable.

In this review, we mainly focus on the polaron effects on the equilibrium and non-equilibrium steady states of multiple-level open quantum systems. The transient dynamics of an open quantum system reveals its dissipative and dephasing properties, as well as the short-time behavior in the presence of control or driving against the noise. However, many systems such as the natural photosynthetic complexes and the artificial quantum nano-devices, the open systems continuously operate at their equilibrium or non-equilibrium steady states. In these cases, we are only interested in the long-time states of the open quantum system whose properties are constant, two aspects of which will be addressed in this paper:

(i) To investigate properties of the equilibrium steady state beyond the weak SBC regime, the polaron transformation can be directly applied to the canonical density of matrix of the total system. Then a perturbative expansion with respect to the normalized SBC reveals the polaron effects on the reduced density of matrix (RDM) of the open system [29, 30], which results in the non-canonical state of the reduced system [30–32].

(ii) Another interesting issue arises when the quantum system is surrounded by the non-equilibrium environment. The characteristics of the non-equilibrium steady state are closely related with the transport quantities, such as the diffusion constant [28], the energy transfer flux [33] and the transfer efficiency [34]. The polaron transformed Redfield equation (PTRE) is suitable for these non-equilibrium problems. The SBC effectively obtained from the polaron transformation is weak enough to introduce the perturbative approach, then the resulting Redfield equation is easily manipulated to yield both the dynamics and the steady states in a broad SBC regime.

In Section 2, we present the general expression for the variational polaron transformation using the SBM as example. The full polaron transformation which is accurate for the fast bath case is straightforwardly obtained by setting the variational parameter equals to the SBC

strength. In Section 3, we obtain the equilibrium steady state by the perturbative expansion in the variational polaron frame. The comparisons with other perturbative methods and the exact numerical calculation are also presented to clarify the valid parameter regimes. The PTRE is introduced in Section 4, by which both the dynamics and the non-equilibrium steady states can be studied beyond weak coupling regime. In Section 5, three specific topics on the excitation transport and energy transfer are studied via the PTRE: the coherent quantum transport in disordered systems, non-equilibrium energy transfer via a two-level quantum dot, and non-equilibrium properties of a three-level heat engine model. We summarize the polaron approach and its application in Section 6.

2 Polaron transformation of the spin-boson model

We introduce the polaron transformation via the SBM, which is the simplest dissipative model used to investigate the energy transfer in light harvesting systems [35, 36], decoherence in atom-photon interaction systems [37], tunneling phenomena in condensed media [38, 39], charge transfer [40], and quantum phase transitions [41, 42]. The SBM describes a two-level system (TLS) coupled with a multi-mode harmonic bath. The SBM Hamiltonian is written as (we set $\hbar = 1$ in the following)

$$H_{tot} = \frac{\epsilon}{2}\sigma_z + \frac{\Delta}{2}\sigma_x + \sum_k \omega_k b_k^\dagger b_k + \sigma_z \sum_k g_k (b_k^\dagger + b_k), \quad (1)$$

where σ_i ($i = x, y, z$) are the Pauli matrices, ϵ is the energy splitting between the two local energy levels, and Δ is the tunneling matrix element. The bath is modeled as a set of harmonic oscillators labeled by their frequencies ω_k , and their coupling strength to the TLS are denoted by g_k .

Though the SBM model is formally simple, it displays the competition between coherent (tunneling dominates) and incoherent (bath dominates) effects. Despite its simplicity, the SBM has not been solved exactly so far. Comparing with the non-trivial analytical investigation base on path integrals [38, 39] and the numerically exact but computationally demanding methods (such as the hierarchy master equation [11] and the QUAPI [13]), the polaron transformation method is clear in physical pictures, accurate in a broad range of SBC strength, and can be easily extended to multilevel systems.

For generality, the variational approach of polaron transformation is adopted here, which extends the valid-

ity of the original full polaron method to the slow bath regime [22, 23, 43]. The variational polaron transformation is generated by

$$U = \exp(-i\sigma_z B/2) \quad (2)$$

with the bath operator $B = 2i \sum_k \frac{f_k}{\omega_k} (b_k^\dagger - b_k)$, which displaces the bath oscillators in the positive or negative direction depending on the state of the TLS. The variational parameter f_k determines the magnitude of the displacement of each mode, when $f_k = 0$ the displacement is zero. If we set $f_k = g_k$, the variational polaron transformation reduces to the full polaron transformation. The variational method allows us to determine an optimal value of f_k between 0 and g_k , making the transformation valid over a wide range of parameters. The effects of the polaron transformation act on the SBM can be illustrated by a double-well in the coordinate space (see Fig. 2). The polaron transformation displaces the effective potential for each local state, and further renormalizes the tunneling rate and the SBC strength. By choosing f_k properly (see below), the high-order SBC are involved in these renormalized parameters, thus the second-order perturbative calculation with the effective SBC is able to give the accurate result.

Applying the transformation to the total Hamiltonian in Eq. (1), we have

$$\tilde{H}_{tot} = U H_{tot} U^\dagger = \tilde{H}_0 + \tilde{H}_I, \quad (3)$$

where the free Hamiltonian is $\tilde{H}_0 = \tilde{H}_S + \tilde{H}_B$. The transformed system Hamiltonian is given by

$$\tilde{H}_S = \frac{\epsilon}{2}\sigma_z + \frac{\Delta}{2}\sigma_x + \sum_k \frac{f_k}{\omega_k} (f_k - 2g_k) \quad (4)$$

and the bath Hamiltonian remains unaffected, $\tilde{H}_B = \sum_k \omega_k b_k^\dagger b_k$. The last term in Eq. (4) is a constant hence can be removed. The tunneling rate is renormalized by the expectation value of the bath displacement operator,

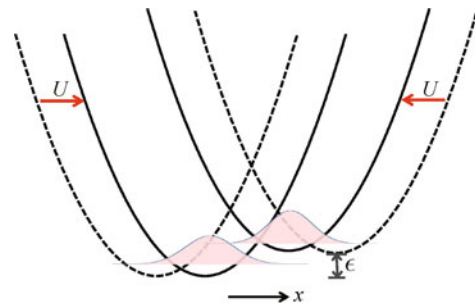


Fig. 2 Polaron effects in the SBM in the coordinate space. The dashed line illustrates the effective potentials for the local states, which are induced by the boson bath and presented as harmonic wells. The polaron transformation U displaces the potential wells (solid line) and renormalizes both the tunneling rate and the SBC strength.

$\Delta_\kappa = \kappa\Delta$, where

$$\begin{aligned} \kappa &= \langle \cos B \rangle_{\tilde{H}_B} \\ &= \exp \left[-2 \sum_k \frac{f_k^2}{\omega_k^2} \coth \left(\frac{\beta\omega_k}{2} \right) \right] \end{aligned} \quad (5)$$

and $\langle \cdot \rangle_{\tilde{H}_B}$ represents the average over the bath canonical density matrix $\rho_B = e^{-\beta\tilde{H}_B} / \text{Tr}_B[e^{-\beta\tilde{H}_B}]$. The transformed interaction Hamiltonian becomes

$$\tilde{H}_I = \sigma_x V_x + \sigma_y V_y + \sigma_z V_z \quad (6)$$

where

$$V_x = \frac{\Delta}{2} (\cos B - \kappa), \quad (7)$$

$$V_y = \frac{\Delta}{2} \sin B, \quad (8)$$

$$V_z = \sum_k (g_k - f_k) (b_k^\dagger + b_k). \quad (9)$$

The interaction Hamiltonian is constructed such that its thermal average is zero, $\text{Tr}_B[\tilde{H}_I \exp(-\beta\tilde{H}_B)] = 0$.

Following Silbey and Harris [22, 23], we determine the optimal values for the set $\{f_k\}$ by minimizing the Gibbs-Bogoliubov–Feynman upper bound on the free energy [44–46]

$$A_B = -\frac{1}{\beta} \ln \text{Tr}_{S+B}[e^{-\beta\tilde{H}_0}] + \langle \tilde{H}_I \rangle_{\tilde{H}_0}, \quad (10)$$

where $\langle \cdot \rangle_{\tilde{H}_0}$ denotes the average over the canonical state with respect to \tilde{H}_0 . Since $\langle \tilde{H}_I \rangle_{\tilde{H}_0} = 0$, the upper bound is solely determined by the free Hamiltonian \tilde{H}_0 . The variational theorem states that $A_B \geq A_F$ where A_F is the true free energy of \tilde{H}_{tot} . Therefore, we seek for the minimal of A_B with respect to f_k by solving $dA_B/df_k = 0$. The minimization condition leads to

$$f_k = g_k F(\omega_k), \quad (11)$$

$$F(\omega_k) = \left[1 + \frac{\Delta_\kappa^2}{\omega_k \Lambda} \coth \left(\frac{\beta\omega_k}{2} \right) \tanh \left(\frac{\beta\Lambda}{2} \right) \right]^{-1}, \quad (12)$$

where $\Lambda = \sqrt{\epsilon^2 + \Delta_\kappa^2}$. In the continuum limit, the renormalization constant can be written as

$$\kappa = \exp \left[-2 \int_0^\infty \frac{d\omega}{\pi} \frac{J(\omega)}{\omega^2} F(\omega)^2 \coth \left(\frac{\beta\omega}{2} \right) \right], \quad (13)$$

where the bath spectral density $J(\omega) = \pi \sum_k g_k^2 \delta(\omega - \omega_k)$. Throughout the paper, we use a super-ohmic spectral density with an exponential cut-off,

$$J(\omega) \propto \gamma \omega^3 \omega_c^{-2} e^{-\omega/\omega_c}, \quad (14)$$

where γ is the dimensionless SBC strength. The cut-off

frequency is denoted by ω_c , which governs the bath relaxation time $\tau_B \propto \omega_c^{-1}$.

Since $F(\omega)$ is also a function of κ , the set of $\{f_k\}$ must be solved self-consistently via Eqs. (11) and (12). Nevertheless, without numerical calculation, the expressions of $F(\omega)$ and κ have already shown insightful physics in two limits: (i) When the bath is slow ($\Delta \gg \omega_c$) or the SBC is weak ($\gamma \ll 1$), we find $F(\omega) \approx 0$ and $f_k \approx 0$, the polaron picture is obviously not applicable in this limit since the bath modes cannot follow the fast coherent oscillation of the system, thus the bath oscillators are barely displaced. (ii) When the bath is fast ($\Delta \ll \omega_c$) or the SBC is strong ($\gamma \gg 1$), we find $F(\omega) \approx 1$ and $f_k \approx g_k$, i.e., the full polaron transformation is recovered. Therefore, when dealing with the open system with fast bath, we can apply the full polaron transformation by setting $f_k = g_k$ for simplicity without losing much accuracy (see Section 3.1).

3 Equilibrium distribution of the SBM via the polaron approach

This section is dedicated to study the equilibrium state of the SBM in the polaron frame, which is motivated mainly for two reasons: (i) The calculation of the equilibrium state of the SBM provides a benchmark to assess the accuracy of only the second-order perturbation theory (2nd-PT) in the polaron frames, without involving additional approximations, such as factorized initial conditions and the Born-Markov approximation which are generally invoked in the quantum master equation. This investigation can clearly demonstrate how accurate does the polaron approach depend on the bath properties, namely, the bath relaxation time and the coupling strength. (ii) Equilibrium canonical distribution in statistical mechanics assumes weak SBC, while under real physical conditions this assumption is usually invalid, thus the equilibrium statistics is generally non-canonical. By exploiting the polaron transformation with perturbation theory, an analytical treatment is advocated to study non-canonical statistics of the SBM at arbitrary temperature and for arbitrary SBC strength.

3.1 Accuracy of the perturbation theory in the polaron frame

First, we briefly introduce the second-order correction to the equilibrium state of the system in the polaron frame. The exact equilibrium RDM can be formally defined as

$$\tilde{\rho}_S = \frac{\text{Tr}_B[e^{-\beta\tilde{H}_{tot}}]}{\text{Tr}_{S+B}[e^{-\beta\tilde{H}_{tot}}]}. \quad (15)$$

In this review, the operator with a tilde denotes it is defined in the polaron frame, for example $\tilde{\rho} = U^\dagger \rho U$, where ρ is the density matrix in the untransformed frame. Using the Kubo identity [47, 48], the operator $\exp[-\beta\tilde{H}_{tot}]$ is expanded up to the second order in \tilde{H}_I as

$$e^{-\beta\tilde{H}_{tot}} \approx e^{-\beta\tilde{H}_0} \left[1 - \int_0^\beta d\beta' e^{\beta'\tilde{H}_0} \tilde{H}_I e^{-\beta'\tilde{H}_0} + \int_0^\beta \int_0^{\beta'} d\beta' d\beta'' e^{\beta'\tilde{H}_0} \tilde{H}_I e^{-(\beta'-\beta'')\tilde{H}_0} \tilde{H}_I e^{-\beta''\tilde{H}_0} \right]. \quad (16)$$

The above expansion is similar to the Dyson expansion, with β treated as imaginary time. Since $\langle \tilde{H}_I \rangle_{\tilde{H}_0} = 0$, the leading order correction to $\tilde{\rho}_S$ is of the second order in \tilde{H}_I . Inserting the above expression into Eq. (15) and keeping terms up to the second order, the system equilibrium state is approximated as

$$\begin{aligned} \tilde{\rho}_S &= \tilde{\rho}_S^{(0)} + \tilde{\rho}_S^{(2)} + \dots, \\ \tilde{\rho}_S^{(0)} &= e^{-\beta\tilde{H}_S} / Z_S^{(0)}, \\ \tilde{\rho}_S^{(2)} &= \frac{A}{Z_S^{(0)}} - \frac{Z_S^{(2)}}{[Z_S^{(0)}]^2} e^{-\beta\tilde{H}_S}, \end{aligned} \quad (17)$$

where

$$\begin{aligned} A &= \sum_{n,m=x,y,z} \int_0^\beta \int_0^{\beta'} d\beta' d\beta'' C_{nm}(\beta' - \beta'') \\ &\quad \times e^{-\beta\tilde{H}_S} \sigma_n(\beta') \sigma_m(\beta''), \\ Z_S^{(0)} &= \text{Tr}_S[e^{-\beta\tilde{H}_S}], \\ Z_S^{(2)} &= \text{Tr}_S[A], \end{aligned} \quad (18)$$

and $C_{nm}(\tau) = \langle V_n(\tau) V_m \rangle_{\tilde{H}_B}$ is the imaginary-time bath correlation function. The operators in imaginary time are defined as $O(\beta) \equiv e^{\beta\tilde{H}_0} O e^{-\beta\tilde{H}_0}$. The expressions for the non-vanishing bath correlation functions are shown in Appendix A. The full polaron result can be conveniently obtained by setting $F(\omega) = 1$, then the only non-vanishing correlation functions are C_{xx} and C_{yy} . Furthermore, in this extremely strong coupling limit $\gamma \rightarrow \infty$, it can be seen from Eq. (13) that $\kappa \rightarrow 0$ and the system becomes incoherent since the coherent tunneling element vanishes. As a result, all of the correlation functions and the second-order corrections to $\tilde{\rho}_S$ vanish; hence the equilibrium density matrix is only determined by the energy splitting of the two local energy levels, $\tilde{\rho}_S \propto \exp(-\epsilon\beta\sigma_z/2)$. In the opposite limit, $F(\omega) = 0$ which corresponds to no transformation is performed and C_{zz} is the only non-zero correlation function.

Since the populations of the TLS are not affected by the transformation, $\text{Tr}_S[\sigma_z \rho_S] = \text{Tr}_S[\sigma_z \tilde{\rho}_S] \equiv \langle \sigma_z \rangle$, we can directly compare the expectation value $\langle \sigma_z \rangle$ from

2nd-PT in the original frame [$F(\omega) = 0$], the full polaron frame [$F(\omega) = 1$], and the variational polaron frame [$F(\omega)$ in Eq. (12)] with those obtained from the numerically exact imaginary-time path integral calculations. Results of the transformed zeroth-order density matrix, $\tilde{\rho}_S^{(0)}$, which depend only on the renormalized system Hamiltonian \tilde{H}_S , are also included.

In order to get a good perspective on the accuracy of 2nd-PT in different frames depends on the properties of the bath, we calculate the relative errors over the entire range of the bath parameters. The relative error is defined as

$$\left| \frac{\langle \sigma_z \rangle_{\text{Pert}} - \langle \sigma_z \rangle_{\text{PI}}}{\langle \sigma_z \rangle_{\text{PI}}} \right|, \quad (19)$$

where the subscripts ‘‘Pert’’ and ‘‘PI’’ denote the perturbative calculation and path integral calculation, respectively. Figure 1 displays the respective errors of second-order perturbation in the three different frames as a function of the cut-off frequency ω_c and the coupling strength γ . As seen in Fig. 3(a), the usual 2nd-PT without transformation breaks down at large γ . It is also less accurate when the cut-off frequency is small, which corresponds to a highly non-Markovian bath. On the other hand, the 2nd-PT in the full polaron frame fails at small γ and ω_c [see Fig. 3(b)]. These two approaches provide complementary behavior as a function of the coupling strength; the full polaron method is essentially exact for large γ , while the usual 2nd-PT is exact for small γ . The variational calculation is valid over a much broader range of parameters [see Fig. 3(c)], and combines the regimes of validity of the full polaron result and the 2nd-PT in the original frame. It becomes only slightly less accurate in the slow bath regime around a narrow region of coupling strength.

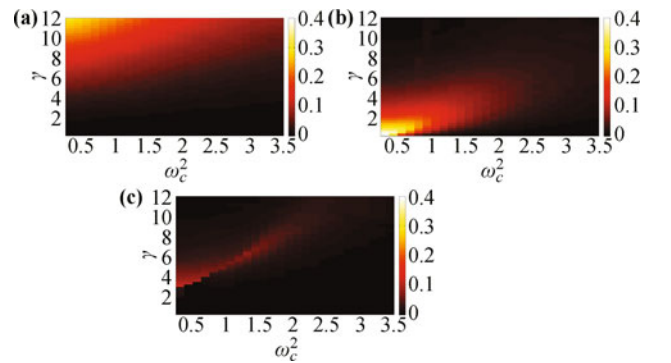


Fig. 3 At $\Delta = 3$, the relative errors of the second-order perturbation theory, compared with the exact stochastic path integral result as defined in Eq. (19), in (a) the original frame, (b) the full polaron frame, and (c) the variational polaron frame. Obviously, the variational polaron method is of high accuracy in the fast bath regime over the entire range of coupling strength. Reproduced from Ref. [29].

The exact numerical method we applied here as benchmark is based on imaginary-time path integrals [18]. For the SBM, following the well-known Feynman-Vernon influence functional [49] with the Hubbard-Stratonovich transformation [39], it was shown that the influence functional is unraveled by an auxiliary stochastic field. The ensuing imaginary-time evolution of the density matrix may then be interpreted as one governed by a time-dependent Hamiltonian with a stochastic field. A primary benefit of this approach is that it generates the entire RDM from one Monte Carlo simulation. Additionally, any form for the bath spectral density $J(\omega)$ can be used. The details of the numerical algorithm can be found in Ref. [18].

In the following of this paper, we will only consider the bath with large cut-off frequency such that the full polaron transformation can be safely applied. Without making ambiguity, from now on when we use the word “polaron transformation”, it actually implies the “full polaron transformation” for brevity.

3.2 Non-canonical equilibrium distribution

To investigate the non-canonical statistics of the TLS at arbitrary temperature and arbitrary SBC strength, both the population and coherence of the RDM should be compared with the canonical density matrix. In particular, we use the RDM in the system eigenbasis to quantify the non-canonical statistics as well as the quantumness of the open system. The agreement of the analytical treatment based on the polaron transformation with the exact stochastic path integral result is also verified.

Different from the diagonal elements ρ_S^{11} and ρ_S^{22} , which are given above by $(1 \pm \langle \sigma_z \rangle)/2$, the off-diagonal element ρ_S^{12} in the polaron picture is more involved because the σ_z operator does not commute with the polaron transformation operator U . Nevertheless, we find

$$\rho_S^{12} = \text{Tr}[\sigma_- \rho_{tot}] = \text{Tr}[\tilde{\sigma}_- \tilde{\rho}_{tot}] = \text{Tr}[\sigma_- \cos B \tilde{\rho}_{tot}] \quad (20)$$

indicating that ρ_S^{12} can still be obtained from $\tilde{\rho}_{tot}$, but not from $\tilde{\rho}_S$. Because of the correlation between the system and the bath, the first-order contribution of \tilde{H}_I to $\exp[-\beta \tilde{H}_{tot}]$ and hence to $\tilde{\rho}_{tot}$ is already nonzero (upon thermal averaging). As such, it suffices to consider a first-order perturbation theory in imaginary time for the total density matrix in the polaron frame. With details elaborated in Ref. [30], we obtain $\rho_S^{12} \approx \rho_{S,(0)}^{12} + \rho_{S,(1)}^{12}$, with

$$\rho_{S,(0)}^{12} = -\frac{\kappa \Delta \kappa}{2A} \tanh(\beta A/2), \quad (21)$$

$$\rho_{S,(1)}^{12} = -\sum_{n=x,y} \int_0^\beta d\tau S_n(\tau) K_n(\tau). \quad (22)$$

Here $S_n(\tau) = \langle \sigma_n(\tau) \sigma_- \rangle_{\tilde{H}_S}$ and $K_n(\tau) = \langle V_n(\tau) \cos B \rangle_{\tilde{H}_B}$ are the correlation functions of the system and the bath, respectively, which are given in Appendix A.

Instead of examining all the RDM elements, a single quantity is used to characterize non-canonical statistics: the smallest possible angle θ . It is the angle rotated (in radians) on the Bloch sphere to reach the eigenstates of H_S from the diagonal representation of the RDM. As a function of the SBC strength γ for a fixed temperature, the theoretical results (solid line) are plotted in Fig. 4(a). For small values of γ , θ is small, so the RDM’s diagonal representation is relatively close to that of H_S . This is expected, because for weak SBC strength, the equilibrium statistics should be canonical. As γ increases, θ increases, indicating that the RDM diagonal representation continuously and monotonously rotates away from the eigenstates of H_S . To further elucidate the continuous change in θ , an analogous angle, namely, the angle that the RDM diagonal representation should be rotated to reach the eigenstates of H_I , is also plotted with dashed line in Fig. 4(a). For large values of γ , we find $\kappa \rightarrow 0$, the SBM reduces to a pure dephasing model. Therefore, the RDM diagonal representation is seen to approach that of H_I (or σ_z), and the system equilibrium state approaches $\exp(-\epsilon \beta \sigma_z/2)$. For a varying SBC strength, either weak or strong, the 2nd-PT polaron approach and the numerically exact results agree, which confirms that our analytical treatment for the RDM off-diagonal elements performs equally well in the regime valid

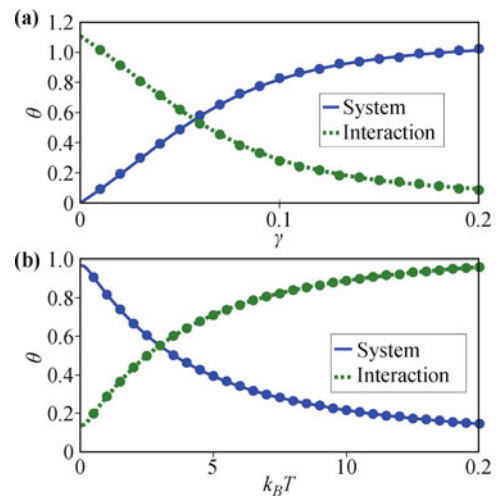


Fig. 4 (a) Coupling strength dependence of the angle to be rotated on the Bloch sphere to reach eigenstates of \tilde{H}_S (solid line) or \tilde{H}_I (dashed line) from eigenstates of equilibrium RDM, for $\beta = 1$, $\epsilon = 0.5$, and $\omega_c = 5$ (in units of Δ). (b) Temperature dependence of the angle to be rotated on the Bloch sphere to reach eigenstates of \tilde{H}_S (solid line) or \tilde{H}_I (dashed line) from eigenstates of equilibrium RDM, for $\gamma = 0.1$, $\epsilon = 0.5$, and $\omega_c = 5$. Solid dots are numerically exact stochastic path integral results. Reproduced from Ref. [30].

for treating the RDM diagonal elements.

The equilibrium RDM considered here reminds us the preferred basis discussed in decoherence dynamics [50]: An equilibrium RDM is an asymptotic result of quantum dissipation. Due to this interesting connection, the particular diagonal representations of RDM as a result of the non-canonical statistics can also be understood as a remarkable outcome of nature’s superselection in open quantum systems [51–54].

The temperature dependence of non-canonical statistics at a fixed intermediate SBC strength γ is depicted in Fig. 4(b). For temperature lower than $k_B T = 1$, the RDM diagonal representation is further rotated from that of H_S (solid line) but becomes closer to that of H_I (dashed line). Therefore, the non-canonical statistics becomes more pronounced when temperature decreases. When temperature increases, the deviation angle continuously changes in opposite directions, showing that the RDM diagonal representation gradually moves away from the eigen-representation of H_I but smoothly approaches that of H_S . Numerically exact Monte Carlo simulation results (solid dots) are also presented in Fig. 4(b), further supporting our theory.

4 Polaron transformed Redfield equation

Besides solving the equilibrium states, the polaron transformation is also a powerful tool to study the dynamics of open quantum systems at strong coupling via the second-order master equation. Applying the polaron method to study the dynamics of open quantum systems was first proposed by Grover and Silbey [24], and it has gained a renewed attention due to the recent interest in coherent energy transfer in light harvesting systems [25–27] and has been extended to study non-equilibrium quantum system [33, 34], which we will introduce in Sec.V. For non-equilibrium steady state, the non-Markovian effect is less significant so we will adopt the secular and Markov approximation.

After the transformation, the system is dressed by polaron, then the master equation is obtained by applying perturbation theory to the transformed system-bath interaction. This approach extends the regime of validity of the quantum master equation to stronger SBC, provided that the tunneling matrix elements are small compared to the bath cut-off frequency ($\Delta < \omega_c$).

In this subsection, we use the SBM as example to introduce the PTRE approach. For a multi-level system, the PTRE can be generalized straightforwardly following the same procedure [28]. The Hamiltonian of the SBM after the full polaron transformation is given in Eq. (3) with

$f_k = g_k$. The strength of the SBC is effectively weakened by the polaron transformation. Specifically, \tilde{H}_I is of the order of bath fluctuation and its thermal average is zero, hence \tilde{H}_I is a reliable perturbative parameter. Based on this consideration, the Born–Markov approximation is applied to derive the PTRE for SBM in the Schrodinger picture:

$$\frac{d\tilde{\rho}_S(t)}{dt} = -i[\tilde{H}_S, \tilde{\rho}_S(t)] - \int_0^\infty ds \text{Tr}_B \{ [\tilde{H}_I, [\tilde{H}_I(-s), \tilde{\rho}_S(t) \otimes \rho_B]] \}, \quad (23)$$

which can be further written as

$$\frac{d\tilde{\rho}_S}{dt} = -i[\tilde{H}_S, \tilde{\rho}_S] - \sum_{\alpha, \beta=z, \pm} [\Gamma_{\alpha\beta}^+ \tau_\alpha \tau_\beta \tilde{\rho}_S + \Gamma_{\beta\alpha}^- \tilde{\rho}_S \tau_\beta \tau_\alpha - \Gamma_{\beta\alpha}^- \tau_\alpha \tilde{\rho}_S \tau_\beta - \Gamma_{\alpha\beta}^+ \tau_\beta \tilde{\rho}_S \tau_\alpha]. \quad (24)$$

Here we use a new set of Pauli operators τ_α with respect to the eigenbasis of the Hamiltonian $\tilde{H}_S = \Lambda \tau_z$:

$$\tau_z = |+\rangle \langle +| - |-\rangle \langle -|, \quad (25)$$

$$\tau_+ = |+\rangle \langle -|, \quad \tau_- = |-\rangle \langle +|. \quad (26)$$

The eigenbasis are defined with the local basis $|1\rangle$ and $|2\rangle$ as

$$|+\rangle = \cos \frac{\theta}{2} |1\rangle + \sin \frac{\theta}{2} |2\rangle, \quad (27)$$

$$|-\rangle = \sin \frac{\theta}{2} |1\rangle - \cos \frac{\theta}{2} |2\rangle, \quad (28)$$

where $\tan \theta = \Delta_\kappa / \epsilon$. The dissipation rates $\Gamma_{\alpha\beta}^\pm$ are related to the half-side Fourier transformation of the bath correlation functions

$$\Gamma_{\alpha\beta}^\pm = \frac{\Delta^2}{4} \int_0^\infty dt \langle \xi_\alpha(\pm t) \xi_\beta(0) \rangle, \quad (29)$$

with

$$\xi_z(t) = \sin \theta [\cos B(t) - \kappa], \quad (30)$$

$$\xi_\pm(t) = -e^{\pm i \Lambda t} \{ \cos \theta [\cos B(t) - \kappa] \mp i \sin B(t) \}. \quad (31)$$

Therefore, the steady state of the system can be easily obtained from Eq. (24) by solving $d\tilde{\rho}_S/dt = 0$.

4.1 Steady states and equilibrium distribution

The expectations of the operators τ_α in the steady state, which contain all the information of the TLS in SBM are displayed in Fig. 5. The dependence of the population difference $\langle \tau_z \rangle$ on the coupling strength γ is plotted with the blue solid line. It is found that the steady

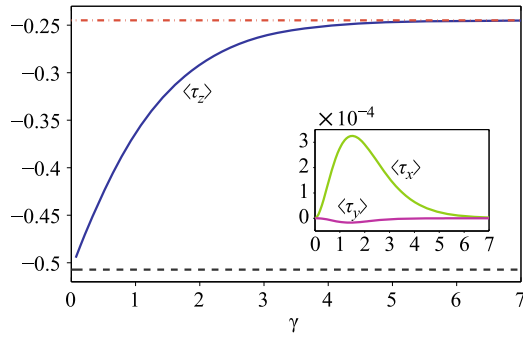


Fig. 5 The steady state of TLS as a function of the SBC strength γ . The steady states of the PTRE follow the canonical distribution in the polaron transformed basis, which rotates with the coupling strength γ . In the weak coupling limit, the system steady state is the canonical distribution in the eigen basis (black dash line); while in the strong coupling limit, the steady state is the canonical distribution in the localized basis (red dot-dash line). The inset shows the coherent term of the steady state, which is small in the polaron transformed basis. We choose the parameters in units of Δ : $\epsilon = 0.5$, $\omega_c = 5$ and $\beta = 1$. Reproduced from Ref. [34].

state RDM obtained from the PTRE coincides with the zeroth-order perturbation result of the equilibrium state in Eq. (17). The steady state distribution of the TLS follows the Boltzmann distribution with respect to the eigenbasis in the polaron frame

$$\langle \tau_z \rangle = -\tanh\left(\frac{1}{2}\beta\Lambda\right). \quad (32)$$

It is reduced to the canonical distribution with respect to the eigenbasis of H_S as $\lim_{\gamma \rightarrow 0} \langle \tau_z \rangle = -\tanh[\beta\sqrt{\epsilon^2 + \Delta^2}/2]$, and is reduced to $\lim_{\gamma \rightarrow \infty} \langle \tau_z \rangle = -\tanh[\beta\epsilon/2]$ in the strong coupling limit, which is the Boltzmann distribution in the local basis $|1\rangle$ and $|2\rangle$.

4.2 Validity of the PTRE

For an unbiased two-level system, we compare the result

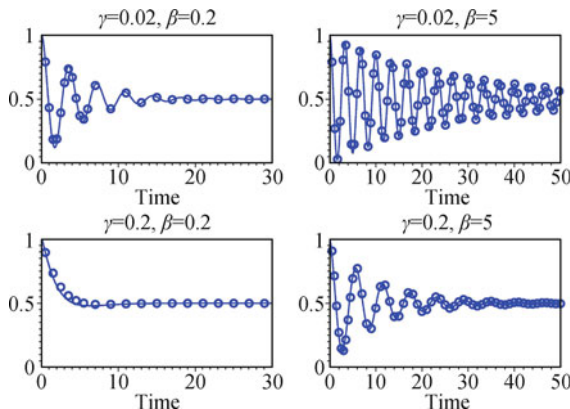


Fig. 6 Time evolution of the population dynamics of the state $|1\rangle$ calculated from the PTRE Eq. (24) (symbols) and the time-convolutionless second-order polaron master equation used in Ref. [55] (solid lines). The parameters used are $\epsilon_1 - \epsilon_2 = 0$, $\Delta = 2$ and $\omega_c = 3$. Reproduced from Ref. [28].

obtained from the above PTRE Eq. (24) with that from the time-convolutionless second-order polaron master equation without the secular and Markov approximations [55]. The results are plotted in Fig. 6, they show remarkably good agreements for different temperature and coupling strength. Moreover, as shown below, the PTRE recovers the Redfield equation in the weak coupling limit and the Fermi's golden rule (or Förster theory) in the strong coupling limit.

4.3 Weak and strong coupling limits

In the weak coupling limit, we have $\kappa \approx 1$, thus the eigenbasis $|\pm\rangle$ of the polaron transformed Hamiltonian \tilde{H}_S become the eigenbasis of $H_S = \frac{\epsilon}{2}\sigma_z + \frac{\Delta}{2}\sigma_x$. In this case the master equation in Eq. (24) with secular approximation is reduced to the Redfield equation

$$\frac{d\rho_S^{++}}{dt} = -\Gamma[1 + N(\Lambda_0)]\rho_S^{++} + \Gamma N(\Lambda_0)\rho_S^{--}, \quad (33)$$

$$\frac{d\rho_S^{+-}}{dt} = -i\Lambda_0\rho_S^{+-} - \Gamma\left[\frac{1}{2} + N(\Lambda_0)\right]\rho_S^{+-}, \quad (34)$$

where $\Gamma = \frac{1}{2}J(\Lambda_0)\sin^2\theta$, $\Lambda_0 = \sqrt{\epsilon^2 + \Delta^2}$ and $N(\omega) = 1/[\exp(\beta\omega) - 1]$. In the strong coupling limit, the coherence is quickly destroyed by dissipation, thus we only need to consider the equations of the population. Additionally, $\kappa \approx 0$ for large γ , i.e., the eigenbasis of \tilde{H}_S coincide with the local basis $|1\rangle$ and $|2\rangle$. As a result, Eq. (24) becomes a kinetic equation governing the population dynamics, which can be written as

$$\frac{d\rho_S^{11}}{dt} = -\Gamma_{11}\rho_S^{11} + \Gamma_{12}\rho_S^{22}, \quad (35)$$

where

$$\Gamma_{11} = \frac{1}{2}\kappa^2\Delta^2 \int_0^\infty d\tau \Re \left[e^{i\epsilon\tau} \left(e^{Q(\tau)} - 1 \right) \right], \quad (36)$$

$$\Gamma_{12} = \frac{1}{2}\kappa^2\Delta^2 \int_0^\infty d\tau \Re \left[e^{-i\epsilon\tau} \left(e^{Q(\tau)} - 1 \right) \right], \quad (37)$$

and

$$Q(\tau) = \int_0^\infty d\omega \frac{J(\omega)}{\pi\omega^2} [\cos(\omega\tau) \coth(\beta\omega/2) - i \sin(\omega\tau)]. \quad (38)$$

The above transition rates Γ_{11} and Γ_{12} are the same as predicted from the Fermi's golden rule. In summary, the PTRE smoothly connects the weak and strong limits, and provides a useful tool to study the intermediate coupling region where there is usually no reliable approximation method.

5 Applications of PTRE to exciton diffusion, heat transport and energy transfer

The PTRE cannot only be used in calculating the steady state and the dynamics of equilibrium systems, but also apply to non-equilibrium problems such as exciton diffusion in disordered system, heat transport through quantum dot and energy transfer in heat engine model. The steady states of these non-equilibrium processes are usually of special interests as they are closely related to the measurable quantities in experiments. The PTRE is a proper tool to study these problems in order to bridge the gap between the standard Redfield equation in weak coupling regime and the Fermi's golden rule or the noninteracting-blip approximation (NIBA) in strong coupling regime.

5.1 Coherent exciton transport in disordered systems

Quantum transport in disordered systems governs a host of fundamental physical processes including the efficiency of light harvesting systems, organic photovoltaics, conducting polymers, and J-aggregate thin films [56–65]. The PTRE approach to quantum transport allows us to bridge coherent band-like transport governed by the Redfield equation to incoherent classical hopping transport described by the Fermi's golden rule. The results reveal that a non-monotonic dependence of the diffusion coefficient can be observed as a function of temperature and system-phonon coupling strength.

The system is extended from single TLS to a tight binding model, described by the Anderson Hamiltonian (see Fig. 7)

$$H_S = \sum_n \epsilon_n |n\rangle \langle n| + \sum_{m \neq n} J_{mn} |m\rangle \langle n|, \quad (39)$$

where $|n\rangle$ denotes the site basis and J_{mn} is the electronic coupling between site m and site n . Here, we consider one dimensional system with nearest-neighbor coupling such that $J_{mn} = J(\delta_{m,n+1} + \delta_{m+1,n})$. The static disorder is

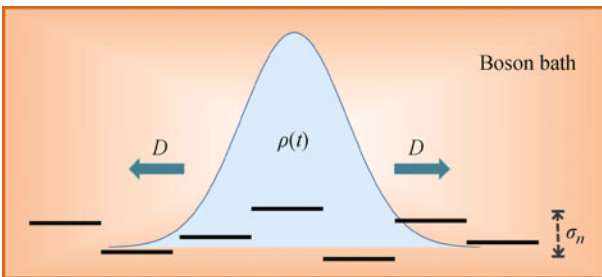


Fig. 7 Illustration of the diffusion of a single excitation in one dimensional system with static disorder and local bosonic noise.

introduced by taking the site energies ϵ_n to be independent, identically distributed Gaussian random variables characterized by their variance $\sigma_n^2 = \overline{\epsilon_n \epsilon_n}$. The overline is used throughout to denote the average over static disorder. We assume that each site is independently coupled to its own phonon bath in the local basis. Thus,

$$H_B = \sum_{nk} \omega_{nk} b_{nk}^\dagger b_{nk}, \quad (40)$$

$$H_I = \sum_{nk} g_{nk} |n\rangle \langle n| (b_{nk}^\dagger + b_{nk}), \quad (41)$$

where ω_{nk} and b_{nk}^\dagger (b_{nk}) are the frequency and the creation (annihilation) operator of the k th mode of the bath attached to site n with coupling strength g_{nk} , respectively.

Applying the full polaron transformation and following the same procedure in Section 4, a second-order PTRE in terms of the transformed SBC with Markov and secular approximations is given by

$$\frac{d\tilde{\rho}_{\nu\nu}(t)}{dt} = \sum_{\nu'} R_{\nu\nu,\nu'\nu'} \tilde{\rho}_{\nu'\nu'}(t), \quad (42)$$

$$\frac{d\tilde{\rho}_{\mu\nu}(t)}{dt} = (-i\omega_{\nu\mu} + R_{\mu\nu,\mu\nu}) \tilde{\rho}_{\mu\nu}(t), \quad \nu \neq \mu. \quad (43)$$

The Greek indices denote the eigenstates of the polaron transformed system Hamiltonian, i.e., $\tilde{H}_S |\mu\rangle = \tilde{E}_\mu |\mu\rangle$ and $\omega_{\mu\nu} = \tilde{E}_\mu - \tilde{E}_\nu$. The Redfield tensor $R_{\mu\nu,\mu'\nu'}$ describes the phonon-induced relaxation, the detailed expressions are given in Appendix B. For the transport properties studied here, only the population dynamics is needed which is invariant under the polaron transformation since $\tilde{\rho}_{nn}(t) = \rho_{nn}(t)$. In the presence of both disorder and dissipation, we find empirically that after an initial transient time approximately proportional to $J^3\beta/\gamma$, the mean square displacement $\langle R^2(t) \rangle = \sum_n n^2 \rho_{nn}(t)$ grows linearly with time, where the origin is defined such that $\langle R^2(0) \rangle = 0$. Within the timescale of the simulations, the number of sites is sufficient such that no significant boundary effect is observed. Then the diffusion constant D can be defined as $\lim_{t \rightarrow \infty} \langle R^2(t) \rangle = 2Dt$.

The effect of the dissipation strength on the diffusion constant is revealed as a non-monotonic dependence on D as a function of γ in Fig. 8, which is consistent with the studies using the Haken–Strobl model [66, 67]. The dissipation destroys the phase coherence that gives rise to Anderson localization in one-dimensional disordered system, allowing for transport to occur. Therefore, in the weak coupling regime, the transport coefficient D increases linearly with γ , which is apparent from the Redfield tensor $R_{\mu\nu,\mu'\nu'}$. In the opposite regime of strong coupling, the dissipation strength effectively acts as

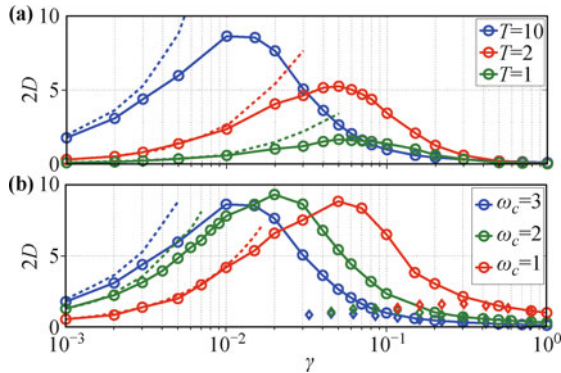


Fig. 8 The diffusion constant as a function of the dissipation strength γ . The dashed lines display the corresponding results from the secular Redfield equation, while diamond symbols depict the results of the Fermi's golden rule rates. **(a)** Results for different temperatures and a fast bath $\omega_c = 3$. **(b)** Results for different cut-off frequencies and $T = 10$. The electronic coupling $J = 1$ sets the energy scale. Reproduced from Ref. [28].

classical friction that impedes the transport leading D to behave as a decreasing function of γ . Thus the coherence generated between sites is quickly destroyed and the quantum transport reduces to a classical hopping dynamics between neighboring sites. The interplay between static disorder and dissipation thus gives rise to an optimal dissipation strength for transport. In Fig. 8(a), it is seen that the maximal diffusive rate both increases and shifts to smaller coupling strengths as the temperature increases, since thermal fluctuations also assist the quantum system to overcome the localization barriers in the weak coupling regime. For comparison, we also include the results from the standard secular Redfield equation in the weak coupling regime. For small γ and T , the secular Redfield equation provides a reliable description of the transport properties but starts to breakdown as γ (or T) increases leading to an unphysical $D \propto \gamma$.

Figure 8(b) depicts D as a function of γ for different bath cut-off frequencies. It is found that the large γ scaling of D is highly dependent on the relaxation time of the bath. For a fast bath, the rates decrease approximately as $1/\gamma$. However, as the bath frequency decreases, a transition from the $1/\gamma$ dependence to $1/\sqrt{\gamma}$ dependence is observed. This can be rationalized by noting that in the high temperature and strong damping regime, the dynamics is incoherent and can be described by classical hopping between nearest neighbors. Then, the hopping rate between sites m and n is accurately determined from Fermi's golden rule,

$$k_F(\Delta_{mn}) = J_{mn}^2 \kappa_{mn}^2 \Re \int_{-\infty}^{\infty} dt e^{i\Delta_{mn}t} [e^{g(t)} - 1], \quad (44)$$

and

$$g(t) = 2 \int_0^{\infty} d\omega \frac{J(\omega)}{\pi\omega} [\cos(\omega t) \coth(\beta\omega/2) - i \sin(\omega t)], \quad (45)$$

where $\Delta_{mn} = \epsilon_m - \epsilon_n$ is the activation barrier. In the slow bath limit, the above expression reduces to the Marcus rate

$$k_M(\Delta) \approx \frac{\pi}{2} J^2 \sqrt{\frac{\beta}{\gamma\omega_c^3}} \exp\left[-\frac{\beta(\pi\Delta - 4\gamma\omega_c^3)^2}{16\pi\gamma\omega_c^3}\right], \quad (46)$$

which captures the correct $1/\sqrt{\gamma T}$ dependence of the rate. Defining the energy transfer time as the inverse of the rate, $\tau_F(\Delta) = 1/k_F(\Delta)$, static disorder can be introduced by averaging $\tau_F(\Delta)$ over the Gaussian distribution of static disorder: $\overline{\tau_F} = \int d\Delta P(\Delta) \tau_F(\Delta)$ where $P(\Delta) = (\sigma'\sqrt{2\pi})^{-1} \exp(-\Delta^2/2\sigma'^2)$ and $\sigma'^2 = \Delta_{mn}^2 = 2\sigma^2$. The disorder-averaged golden rule rate can then be obtained using $\overline{k_F} = 1/\overline{\tau_F}$ and is plotted in Fig. 8(b). While it is seen to capture the correct scaling of D in the overdamped regime, it significantly underestimates the transport in the small and intermediate damping regimes. As the dynamics becomes more coherent, the classical hopping rate between sites provides a qualitatively incorrect description of the transport.

5.2 Non-equilibrium heat transfer through quantum dot

In presence of multiple baths with different temperatures, non-equilibrium transport phenomena can also be studied using the PTRE. For typical energy transport far from equilibrium, two baths should be included with a temperature bias, as shown in Fig. 9. The TLS with Hamiltonian H_S in Eq. (1) couples to the two baths by

$$H_I = \sigma_z \sum_{k;v=L,R} g_{k,v} (b_{k,v}^\dagger + b_{k,v}), \quad (47)$$

where $b_{k,v}^\dagger$ ($b_{k,v}$) creates (annihilates) one boson of mode k in the v th bath. The Hamiltonian of the left (L) and right (R) baths is given by $H_B = \sum_{k;v=L,R} \omega_{k,v} b_{k,v}^\dagger b_{k,v}$. This non-equilibrium spin-boson model (NESB) has been used to describe the electromagnetic transport through superconducting circuits [68], photonic waveguides with

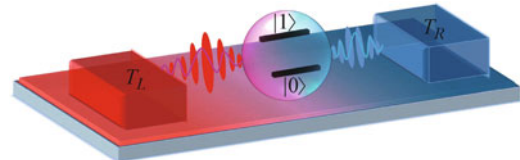


Fig. 9 Schematic illustration of the non-equilibrium spin-boson model composed by central two-level nano-device connecting to two separate bosonic baths with temperature T_L and T_R respectively. Reproduced from Ref. [33].

a local impurity [69], phononic energy transfer [70–74] and Caldeira–Leggett model [75] in phononics [76], Kondo physics and non-equilibrium phase transitions [77, 78] in the field of condense matter physics, and even exciton transfer embedded in the photosynthetic complexes [10, 60, 79–81]. Moreover, as a minimal prototype, it provides crucial insights into the optimal design and potential applications of low-dimensional nano-devices.

The PTRE approach provides a unified interpretation of several observations, including coherence-enhanced heat flux and negative differential thermal conductance (NDTC). Despite many approaches have been proposed to explore energy transfer in NESB, each approach has limitations. Typically, the Redfield equation only applies in the weak spin-boson coupling regime [72, 74], whereas the non-equilibrium version of the noninteracting-blip approximation (NIBA) equation applies in the strong spin-boson coupling regime.

Combining the polaron transformation and the counting field [74, 82], we obtain the energy flux as

$$\mathcal{J} = \frac{\Delta_\kappa^2}{8\pi} \int_{-\infty}^{\infty} d\omega \omega [C_e(0, \omega) + \frac{\phi_o(\Delta_\kappa)C_o(-\Delta_\kappa, \omega) + \phi_o(-\Delta_\kappa)C_o(\Delta_\kappa, \omega)}{\phi_o(\Delta_\kappa) + \phi_o(-\Delta_\kappa)}], \quad (48)$$

where $C_{e(o)}(\omega, \omega')$ describes that when the TLS releases energy ω by relaxing from the excited state to the ground one, the right bath absorbs energy ω' and the left one obtains the left $\omega - \omega'$ if $\omega > \omega'$ or supply the compensation if $\omega < \omega'$. And $C_{e(o)}(-\omega, \omega')$ describes similar dynamical processes for the TLS jumping from the ground state to the exciting one. While $\phi_{e(o)}(\omega)$ is the summation behavior of these corresponding microscopic processes. The details of the functions $\phi_{o(e)}$ and $C_{o(e)}$ can be found in Appendix C. Different from the single bath SBM case, here the renormalization κ is actually a product of the ones from each bath: $\kappa = \kappa_L \kappa_R$.

In the weak coupling limit, the renormalization factor is simplified to $\kappa \approx 1$, then the unified energy flux reduces to the resonant energy transfer expression

$$\mathcal{J}_w = \frac{\Delta}{2} \frac{J_L(\Delta)J_R(\Delta)(n_L - n_R)}{J_L(\Delta)(1 + 2n_L) + J_R(\Delta)(1 + 2n_R)}, \quad (49)$$

with the average phonon number $n_v = n_v(\Delta)$ of the v th bath, which is consistent with previous results of the Redfield approach [72, 74]. In the strong coupling limit, multiple bosons are excited from baths, and both the renormalization factor κ and the eigen-energy gap of the TLS Δ_κ become zero. Hence, the energy flux can be finally expressed as

$$\mathcal{J}_w = \frac{\Delta^2}{8\pi} \int_{-\infty}^{\infty} d\omega \omega C_L(-\omega)C_R(\omega), \quad (50)$$

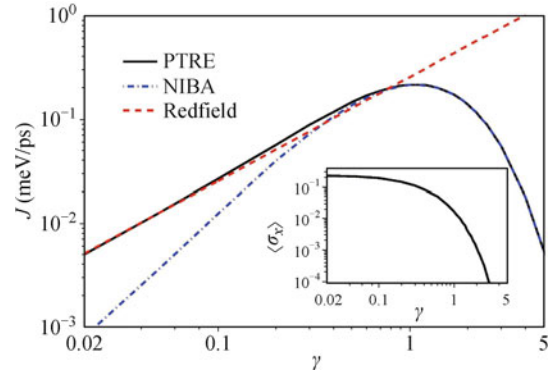


Fig. 10 The energy flux and quantum coherence represented by $\langle \sigma_x \rangle$, as functions of the coupling strength. The solid black line is from the PTRE, which unifies the Redfield result at the weak coupling (*the red dashed line*) and the NIBA result at the strong coupling (*the dot-dashed blue line*). The deviation of the unified energy flux from the NIBA result at small γ is characterized by the quantum coherence σ_x (inset). Parameters are given by $\epsilon = 0$, $\Delta = 5.22$ meV, $\omega_c = 26.1$ meV, $T_L = 150$ K and $T_R = 90$ K. Reproduced from Ref. [33].

with the probability density of the v th bath $C_v(\omega)$ correctly recovering the non-equilibrium NIBA result.

The energy flux of Eq. (48) is plotted in Fig. 10, which first shows linear increase with the SBC in the weak regime, consistent with the Redfield. After reaching a maximum, the energy flux decreases monotonically in the strong coupling regime, and coincides with the NIBA result. The discrepancy of the NIBA and our PTRE is due to the improper ignorance of quantum coherence σ_x of the TLS in NIBA. This coherence term describes the effective tunneling within TLS so that it enhances the energy transfer compared to the NIBA that ignores it. Therefore, we conclude that the unified energy flux expression of Eq. (48) provides a comprehensive interpretation for energy transfer in NESB, because the fluctuation-decoupling scheme not only describes the coherent SBC from the weak to strong coupling regime, but also correctly captures the coherence within the TLS.

For the NDTC, the non-equilibrium NIBA scheme predicts its appearance in the strong coupling for NESB, whereas the Redfield scheme predicts its absence in the weak coupling. The NDTC can also be investigated by the PTRE to identify its absence over the wide range of temperature bias, even in the intermediate and strong coupling regimes, which correct the previous observation of NDTC under the NIBA in the classical limit. By tuning one bath temperature, NDTC is absent across a wide range of the temperature bias in the NESB model even in the strong SBC limit. It should also be noted, if we change two temperatures simultaneously, NDTC can still occur in NESB. The detail discussion about the NDTC via PTRE can be found in reference [33].

5.3 Energy transfer via three-level heat engine model

Taking a three-level system as a generic theoretical model, many interesting mechanisms can be well demonstrated and understood. Recently, the sunlight-induced exciton coherence is studied in a V-configuration three-level model [83, 84]. An interesting idea is to consider the energy transfer process from the perspective of heat engine [85]. For example, the coherence introduced by an auxiliary energy level can enhance the heat engine power [86, 87]. The early work considering a three-level maser model as a Carnot engine was carried out by Scovil and Schulz-DuBois [88, 89], yielding the heat engine efficiency η_0 and its relation with the Carnot efficiency. Later papers elaborately reexamined the dynamics of this model by the Lindblad master equation and showed that the thermodynamic efficiency η_0 is achieved when the output light-field is strongly coupled with the system [90–92].

We consider the energy transfer process in the three-level system illustrated in Fig. 11. The site energy of the ground state $|0\rangle$ is set to zero. The two excited energy levels $|1\rangle$ and $|2\rangle$ form a TLS, the Hamiltonian of which is the same as H_S in Eq. (1). The energy transfer takes place in the single excitation subspace: The three-level system is firstly excited to state $|1\rangle$ by a photon field, then the excitation is transferred to state $|2\rangle$ through Δ (mediated by phonon modes), and finally the excitation decays to the ground state $|0\rangle$ via spontaneous radiation. The pumping and trapping processes are modeled by the interaction with the two independent photon baths, which are coupled separately with two transitions $|0\rangle \leftrightarrow |1\rangle$ and $|0\rangle \leftrightarrow |2\rangle$. The Hamiltonian of the photon baths and their interactions with the three-level system are given by

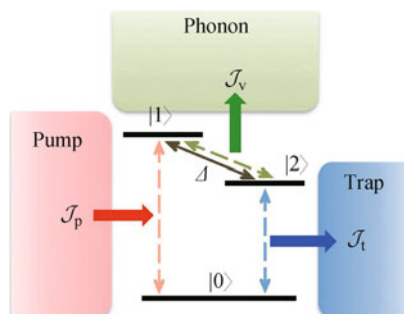


Fig. 11 The system is modeled by a three-level system: its ground state $|0\rangle$ and the excited state $|1\rangle$ ($|2\rangle$) is coupled with the pumping (trapping) bath; the excited states $|1\rangle$ and $|2\rangle$ are diagonal-coupled with the phonon bath; the internal transition strength between $|1\rangle$ and $|2\rangle$ is characterized by Δ . The energy fluxes \mathcal{J}_p , \mathcal{J}_v and \mathcal{J}_t describe the energy exchange rate of the system with the pumping, the phonon and the trapping baths, respectively. The flux into the system is defined as the positive direction. Reproduced from Ref. [34].

$$H_p = \sum_k \omega_{pk} a_{pk}^\dagger a_{pk} + (g_{pk} a_{pk}^\dagger |0\rangle \langle 1| + \text{h.c.}), \quad (51)$$

$$H_t = \sum_k \omega_{tk} a_{tk}^\dagger a_{tk} + (g_{tk} a_{tk}^\dagger |0\rangle \langle 2| + \text{h.c.}), \quad (52)$$

where ω_{ik} ($i = p, t$) is the eigen frequency of the bath mode described by the creation (annihilation) operator a_{ik}^\dagger (a_{ik}), and its coupling strength to the excited state is g_{ik} . We note that the rotating wave approximation is applied in the system-bath interaction term. A phonon bath with creation and annihilation operators b_k^\dagger and b_k of the bath mode ω_{vk} is coupled to the TLS via diagonal interaction with the coupling strength of f_k . Thus, the phonon part is described by

$$H_v = \sum_k \omega_{vk} b_k^\dagger b_k + (|1\rangle \langle 1| - |2\rangle \langle 2|) \sum_k (f_k b_k^\dagger + \text{h.c.}). \quad (53)$$

The steady state of the three-level system can be easily obtained from PTRE and the steady state energy fluxes defined are straightforwardly given as

$$\mathcal{J}_p = \epsilon_1 \gamma_p [n_p \rho_{00} - (n_p + 1) \rho_{11}] - \frac{\Delta \gamma_p}{2} (n_p + 1) \Re[\rho_{12}], \quad (54)$$

$$\mathcal{J}_t = \epsilon_2 \gamma_t [n_t \rho_{00} - (n_t + 1) \rho_{22}] - \frac{\Delta \gamma_t}{2} (n_t + 1) \Re[\rho_{12}], \quad (55)$$

where the steady state elements of RDM is denoted by $\rho_{ij} = \langle i | \rho_S(\infty) | j \rangle$ for brevity, γ_i and n_i are the corresponding decay rate and average photon number for the i th bath. In Fig. 12 we present the dependence of energy fluxes on the coupling strength γ . In the extreme case that the system bath coupling is switched off ($\gamma = 0$), there is no loss of excitation energy, which results in $|\mathcal{J}_p| = |\mathcal{J}_t|$, suggesting the input energy flux from the pump completely flows into the trap through the three-level system. When the coupling turns on, a portion of energy flux leaks into the phonon bath thus $|\mathcal{J}_p| > |\mathcal{J}_t|$. Both the pumping and trapping energy fluxes reach their optimal values in the intermediate coupling region and decrease to zero when the coupling strength is strong.

The energy transfer efficiency is defined as $\eta \equiv |\mathcal{J}_t / \mathcal{J}_p|$. When the coupling strength $\gamma = 0$, the energy transfer efficiency $\eta = 1$ because there is no loss of energy flux. When the coupling strength gradually increases, the efficiency decreases. However, after reaching its minimum value, the efficiency starts to rise with γ , which is shown in Fig. 12(a). The increase of efficiency assisted by noise was studied extensively in the context of energy transfer in light-harvesting systems [93, 94]. As we further increase γ , the efficiency grows beyond the

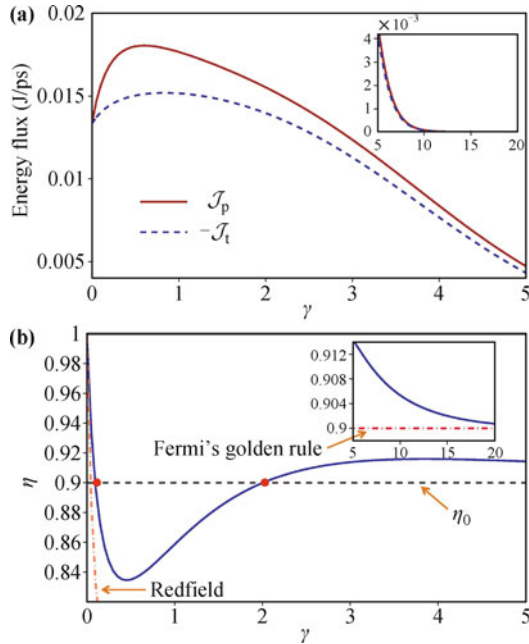


Fig. 12 (a) The steady state pumping (red solid line) and trapping (blue dashed line) energy fluxes versus γ . Both fluxes show a maximal value in the weak coupling case and then quickly decreases to zero when γ increases. (b) The steady states efficiency η is plotted with blue solid line as a function of γ . The dashed line indicates the strong coupling limit η_0 . The results given by the Redfield equation and the Fermi's golden rule are shown with the dashed-dot lines. The strong coupling regions are plotted in the insets. We choose the parameters in units of Δ : $\epsilon = 0.5$, $\omega_c = 5$, $\beta_v = 1$, $\beta_p = 0.02$, $\beta_t = 1$, and $\gamma_p = \gamma_t = 0.01$. Reproduced from Ref. [34].

strong coupling limit η_0 and then gradually approaches this limit from above. The strong coupling region is plotted in the inset of Fig. 12(a).

It is interesting to notice that the first term on the right side of Eqs. (54) and (55) depends only on the populations of the three-level system, and the second term represents the contribution of the off-diagonal terms (coherence in the local basis). In the strong coupling limit, the steady state coherence in the local bases ρ_{12} vanishes, then the efficiency is completely determined by the populations:

$$\eta \approx -\frac{\epsilon_2 \gamma_t [(n_t + 1) \rho_{22} - n_t \rho_{00}]}{\epsilon_1 \gamma_p [(n_p + 1) \rho_{11} - n_p \rho_{00}]} = \frac{\epsilon_2}{\epsilon_1}. \quad (56)$$

This result indicates that when the coherence is negligible due to the strong system-phonon coupling, the energy transfer efficiency η approaches η_0 , which is consistent with the key result of Ref. [91]. We notice that Eq. (56) shows that the net rate of pumping one excitation to $|1\rangle$ equals to the net rate of trapping one excitation from $|2\rangle$ to $|0\rangle$. When the coupling strength decreases, the efficiency is generally related to the phonon bath induced coherence of the excited states [95]. If we require the sys-

tem outputs positive energy, i.e., $\gamma_t(n_t + 1)\rho_{22} > \gamma_t n_t \rho_{00}$, then $\Re[\rho_{12}] > 0$ leads to the result $\eta > \eta_0$ and vice versa.

In the local basis, the population and coherence are coupled with each other due to the polaron effects: The population inversion happens when $\Re[\rho_{12}] < 0$ [Fig. 12(b)], hence $\eta < \eta_0$. We plot the population difference between states $|1\rangle$ and $|2\rangle$ in Fig. 12(b). In the intermediate coupling region indicated between the two red dots, the steady state population satisfies $\rho_{11} < \rho_{22}$ (the effective temperature associates with these two states is positive), the corresponding efficiency η is less than η_0 as shown in Fig. 12(a). On the contrary, outside this intermediate region, i.e., when the coupling is either very weak or very strong, the populations are inverted $\rho_{11} > \rho_{22}$ (the effective temperature is negative); meanwhile η increases beyond η_0 .

As we discussed in Section 3, the non-negligible SBC strength can induce the non-canonical equilibrium states, which will further affect the heat engine performance. In this section we show the PTRE is also a powerful tool to evaluate the performance of a three-level heat engine model beyond the weak coupling limit. In particular, the non-negligible system-bath entanglement not only modifies the steady state, resulting in population inversion, but also introduces a finite steady state coherence that optimizes the energy transfer flux and efficiency. Remarkably, there exists a quantitative relationship between the efficiency and the steady-state coherence, which in turn is proportional to the degree of population inversion. Taking into account of the behavior of both the flux and efficiency, we are able to optimize coupling and temperature in designing optimal artificial energy transfer systems.

6 Summary

In this review article, we systematically introduce the polaron transformation approach to describe non-canonical equilibrium distribution and non-equilibrium steady states in the open quantum system. By applying the polaron transformation, the open system of interest is dressed by the surrounding environment which is described by a set of displaced harmonic modes. The residue coupling between the polaron transformed system and the bath is thus suppressed to the weak coupling regime, even though the SBC in the original frame of reference is strong. Such advantages give rise to the possibility of introducing the usual methods used in the weak coupling open system in the polaron frame.

We studied the non-canonical equilibrium state of the SBM. The second-order perturbation theory in the po-

laron frame is used to obtain the equilibrium density matrix. The second-order results in the original frame are accurate only for weak SBC, whereas the full polaron results are accurate in the entire range of SBC for fast bath but only in the strong coupling regime for slow bath. The variational method is capable of interpolating between these two methods and is valid over a much broader range of parameters. Further, the non-canonical properties of the equilibrium states is revealed and the eigenbasis in the polaron frame are considered as the preferred basis for decoherence.

We then applied the polaron transformed Redfield equation to solve the steady states of non-equilibrium open systems. (i) In a one-dimensional disordered chain, the diffusion coefficient is shown to be linearly proportional to the exciton-phonon coupling strength in the weak coupling limit, while in the strong coupling limit, the diffusion coefficient depends on the phonon bath relaxation time which is the character of the hopping transport behavior. (ii) The heat transfer through a two-level quantum dot which connects with two separate baths was also investigated. The non-monotonic energy flux and differential thermal conductance were calculated following a similar polaron approach. (iii) When the three-level system is connected with three different heat baths, a heat engine model is thus constructed to study the steady state energy transfer flux and energy conversion efficiency. The steady state coherence and population inversion affect the efficiency obviously. In both the weak and strong coupling limits, the PTRE is coincidence with the Redfield equation and the Fermi's golden rule, which further verifies the validity of the polaron approach.

Acknowledgements D. Xu and J. Cao acknowledge the National Science Foundation (NSF) of the US (Grant No. CHE-1112825).

Appendix A Correlation functions in Eq. (18)

The non-vanishing bath correlation functions in Eq. (18) are

$$C_{xx}(\tau) = \frac{\Delta_\kappa^2}{8} \left(e^{\phi(\tau)} + e^{-\phi(\tau)} - 2 \right), \quad (A1)$$

$$C_{yy}(\tau) = \frac{\Delta_\kappa^2}{8} \left(e^{\phi(\tau)} - e^{-\phi(\tau)} \right), \quad (A2)$$

$$C_{zz}(\tau) = \int_0^\infty \frac{d\omega}{\pi} J(\omega) [1 - F(\omega)]^2 \frac{\cosh((\beta - 2\tau)\omega/2)}{\sinh(\beta\omega/2)}, \quad (A3)$$

$$C_{zy}(\tau) = -C_{yz}(\tau)$$

$$= i\Delta_\kappa \int_0^\infty \frac{d\omega}{\pi} \frac{J(\omega)}{\omega} F(\omega) [1 - F(\omega)] \frac{\sinh((\beta - 2\tau)\omega/2)}{\sinh(\beta\omega/2)}, \quad (A4)$$

where

$$\phi(\tau) = 4 \int_0^\infty \frac{d\omega}{\pi} \frac{J(\omega)}{\omega^2} F(\omega)^2 \frac{\cosh((\beta - 2\tau)\omega/2)}{\sinh(\beta\omega/2)}. \quad (A5)$$

The correlation functions in the off-diagonal parts of the RDM are given by

$$S_x(\tau) = \frac{\Delta_\kappa^2}{2\Lambda^2} + \frac{\epsilon \operatorname{sech}(\beta\Lambda/2)}{2\Lambda^2} \left\{ \epsilon \cosh\left[\frac{\Lambda}{2}(\beta - 2\tau)\right] + \Lambda \sinh\left[\frac{\Lambda}{2}(\beta - 2\tau)\right] \right\}, \quad (A6)$$

$$S_y(\tau) = -\frac{i}{2} \operatorname{sech}(\beta\Lambda/2) \left\{ \cosh\left[\frac{\Lambda}{2}(\beta - 2\tau)\right] + \frac{\epsilon}{\Lambda} \sinh\left[\frac{\Lambda}{2}(\beta - 2\tau)\right] \right\}. \quad (A7)$$

The bath correlation functions are $K_x(\tau) = 2C_x(\tau)/\Delta$ and $K_y(\tau) = 2iC_y(\tau)/\Delta$. Note that the first-order correction here is again linked with the above-defined bath correlation function $C_{nn}(\tau)$. So, by construction, our perturbation theory for off-diagonal elements of RDM works even better for stronger SBC coupling.

Appendix B Redfield tensor in Eqs. (42) and (43)

The Redfield tensor in Eqs. (42) and (43) are given as

$$R_{\mu\nu,\mu'\nu'} = \Gamma_{\nu'\nu,\mu\mu'} + \Gamma_{\mu'\mu,\nu\nu'}^* - \delta_{\nu\nu'} \sum_\kappa \Gamma_{\mu\kappa,\kappa\mu'} - \delta_{\mu\mu'} \sum_\kappa \Gamma_{\nu\kappa,\kappa\nu'}^*, \quad (B1)$$

$$\Gamma_{\mu\nu,\mu'\nu'} = \sum_{mnm'n'} J_{mn} J_{m'n'} \langle \mu | m \rangle \langle n | \nu \rangle \langle \mu' | m' \rangle \langle n' | \nu' \rangle \times K_{mn,m'n'}(\omega_{\nu'\mu'}), \quad (B2)$$

where $K_{mn,m'n'}(\omega)$ is the half-Fourier transform of the bath correlation function

$$K_{mn,m'n'}(\omega) = \int_0^\infty e^{i\omega t} \langle V_{mn}(t) V_{m'n'}(0) \rangle_{\tilde{H}_B} dt. \quad (B3)$$

Appendix C Details in non-equilibrium energy flux of Eq. (48)

The relaxation rate in Eq. (48) can be rewritten as

$$\phi_{e(o)}(\omega) = (2\pi)^{-1} \int_{-\infty}^{\infty} d\omega' C_{e(o)}(\omega, \omega'). \quad (C1)$$

The corresponding kernel functions are given by

$$C_e(\omega, \omega') = \frac{1}{2} \sum_{\sigma=\pm} C_L^\sigma(\omega - \omega') C_R^\sigma(\omega') - \delta(\omega'), \quad (C2)$$

$$C_o(\omega, \omega') = \frac{1}{2} \sum_{\sigma=\pm} \sigma C_L^\sigma(\omega - \omega') C_R^\sigma(\omega'), \quad (C3)$$

where

$$C_v^\pm(\omega') = \int_{-\infty}^{\infty} d\tau e^{i\omega'\tau \pm Q_v(\tau)} \quad (C4)$$

describes the rate density of the v th bath absorbing (emitting) energy $\omega(-\omega)$, obeying the detailed balance relation as $C_v^\pm(\omega')/C_v^\pm(-\omega') = e^{\beta_v\omega'}$. And

$$Q_v(\tau) = \int_0^\infty d\omega \frac{J_\nu(\omega)}{\pi\omega^2} [\cos(\omega\tau) \coth(\beta_\nu\omega/2) - i \sin(\omega\tau)]. \quad (C5)$$

References

1. A. G. Redfield, The theory of relaxation processes, *Adv. Magn. Reson.* 1, 1 (1965)
2. G. Lindblad, On the generators of quantum dynamical semigroups, *Commun. Math. Phys.* 48(2), 119 (1976)
3. H. P. Breuer and F. Petruccione, *The Theory of Open Quantum Systems*, New York: Oxford University Press, 2002
4. J. Cao, A phase-space study of Bloch–Redfield theory, *J. Chem. Phys.* 107(8), 3204 (1997)
5. S. A. Crooker, J. A. Hollingsworth, S. Tretiak, and V. I. Klimov, Spectrally resolved dynamics of energy transfer in quantum-dot assemblies: Towards engineered energy flows in artificial materials, *Phys. Rev. Lett.* 89(18), 186802 (2002)
6. D. Kim, S. Okahara, M. Nakayama, and Y. Shim, Experimental verification of Förster energy transfer between semiconductor quantum dots, *Phys. Rev. B* 78(15), 153301 (2008)
7. S. I. E. Vulto, M. A. de Baat, R. J. W. Louwe, H. P. Permentier, T. Neef, M. Miller, H. van Amerongen, and T. J. Aartsma, Exciton simulations of optical spectra of the FMO complex from the green sulfur bacterium *Chlorobium tepidum* at 6 K, *J. Phys. Chem. B* 102(47), 9577 (1998)
8. T. Brixner, J. Stenger, H. M. Vaswani, M. Cho, R. E. Blankenship, and G. R. Fleming, Two-dimensional spectroscopy of electronic couplings in photosynthesis, *Nature* 434(7033), 625 (2005)
9. G. S. Engel, T. R. Calhoun, E. L. Read, T. Ahn, T. Manical, Y. C. Cheng, R. E. Blankenship, and G. R. Fleming, Evidence for wavelike energy transfer through quantum coherence in photosynthetic systems, *Nature* 446(7137), 782 (2007)
10. J. Wu, F. Liu, Y. Shen, J. Cao, and R. J. Silbey, Efficient energy transfer in light-harvesting systems (I): optimal temperature, reorganization energy and spatial–temporal correlations, *New J. Phys.* 12(10), 105012 (2010)
11. Y. Tanimura, Stochastic Liouville, Langevin, Fokker–Planck, and master equation approaches to quantum dissipative systems, *J. Phys. Soc. Jpn.* 75(8), 082001 (2006)
12. R. X. Xu and Y. J. Yan, Dynamics of quantum dissipation systems interacting with bosonic canonical bath: Hierarchical equations of motion approach, *Phys. Rev. E* 75(3), 031107 (2007)
13. N. Makri and D. E. Makarov, Tensor propagator for iterative quantum time evolution of reduced density matrices (I): Theory, *J. Chem. Phys.* 102(11), 4600 (1995)
14. J. Prior, A. W. Chin, S. F. Huelga, and M. B. Plenio, Efficient simulation of strong system–environment interactions, *Phys. Rev. Lett.* 105(5), 050404 (2010)
15. S. Tornow, R. Bulla, F. B. Anders, and A. Nitzan, Dissipative two-electron transfer: A numerical renormalization group study, *Phys. Rev. B* 78(3), 035434 (2008)
16. H. D. Meyer, U. Manthe, and L. Cederbaum, The multi-configurational time-dependent Hartree approach, *Chem. Phys. Lett.* 165(1), 73 (1990)
17. M. Thoss, H. Wang, and W. H. Miller, Self-consistent hybrid approach for complex systems: Application to the spin-boson model with Debye spectral density, *J. Chem. Phys.* 115(7), 2991 (2001)
18. M. Moix, Y. Zhao, and J. Cao, Equilibrium-reduced density matrix formulation: Influence of noise, disorder, and temperature on localization in excitonic systems, *Phys. Rev. B* 85(11), 115412 (2012)
19. J. Moix, J. Ma, and J. Cao, Förster resonance energy transfer, absorption and emission spectra in multichromophoric systems (III): Exact stochastic path integral evaluation, *J. Chem. Phys.* 142(9), 094108 (2015)
20. H. Fröhlich, Electrons in lattice fields, *Adv. Phys.* 3, 325 (1954)
21. T. Holstein, Studies of polaron motion, *Ann. Phys.* 8(3), 325 (1959)
22. R. Silbey and R. A. Harris, Variational calculation of the dynamics of a two level system interacting with a bath, *J. Chem. Phys.* 80(6), 2615 (1984)
23. R. A. Harris and R. Silbey, Variational calculation of the tunneling system interacting with a heat bath (II): Dynamics of an asymmetric tunneling system, *J. Chem. Phys.* 83(3), 1069 (1985)
24. M. Grover and R. Silbey, Exciton migration in molecular crystals, *J. Chem. Phys.* 54(11), 4843 (1971)
25. S. Jang, Y. C. Cheng, D. R. Reichman, and J. D. Eaves, Theory of coherent resonance energy transfer, *J. Chem. Phys.* 129(10), 101104 (2008)
26. A. Nazir, Correlation-dependent coherent to incoherent transitions in resonant energy transfer dynamics, *Phys. Rev. Lett.* 103(14), 146404 (2009)

27. D. P. S. McCutcheon and A. Nazir, Quantum dot Rabi rotations beyond the weak exciton–phonon coupling regime, *New J. Phys.* 12(11), 113042 (2010)
28. C. K. Lee, J. M. Moix, and J. Cao, Coherent quantum transport in disordered systems: A unified polaron treatment of hopping and band-like transport, *J. Chem. Phys.* 142(16), 164103 (2015)
29. C. K. Lee, J. Moix, and J. Cao, Accuracy of second order perturbation theory in the polaron and variational polaron frames, *J. Chem. Phys.* 136(20), 204120 (2012)
30. C. K. Lee, J. Cao, and J. Gong, Noncanonical statistics of a spin-boson model: Theory and exact Monte Carlo simulations, *Phys. Rev. E* 86(2), 021109 (2012)
31. H. Dong, S. Yang, X. F. Liu, and C. P. Sun, Quantum thermalization with couplings, *Phys. Rev. A* 76(4), 044104 (2007)
32. D. Z. Xu, S. W. Li, X. F. Liu, and C. P. Sun, Noncanonical statistics of a finite quantum system with non-negligible system-bath coupling, *Phys. Rev. E* 90(6), 062125 (2014)
33. C. Wang, J. Ren and J. Cao, Nonequilibrium energy transfer at nanoscale: A unified theory from weak to strong coupling, *Scientific Reports* 5, 11787 (2015)
34. D. Z. Xu, C. Wang, Y. Zhao, and J. Cao, Polaron effects on the performance of light-harvesting systems: A quantum heat engine perspective, *New J. Phys.* 18(2), 023003 (2016)
35. A. Ishizaki and G. R. Fleming, On the adequacy of the Redfield equation and related approaches to the study of quantum dynamics in electronic energy transfer, *J. Chem. Phys.* 130(23), 234110 (2009)
36. L. A. Pachón and P. Brumer, Computational methodologies and physical insights into electronic energy transfer in photosynthetic light-harvesting complexes, *J. Phys. Chem. Lett.* 2, 2728 (2011), arXiv: 1203.3978
37. H. J. Carmichael, *Statistical Methods in Quantum Optics*, Springer, 1999
38. A. J. Leggett, S. Chakravarty, A. T. Dorsey, M. P. A. Fisher, A. Garg, and W. Zwerger, Dynamics of the dissipative two-state system, *Rev. Mod. Phys.* 59(1), 1 (1987)
39. U. Weiss, *Quantum Dissipative Systems*, Singapore: World Scientific, 2008
40. J. Cao, Effects of bath relaxation on dissipative two-state dynamics, *J. Chem. Phys.* 112(15), 6719 (2000)
41. A. W. Chin, J. Prior, S. F. Huelga, and M. B. Plenio, Generalized polaron ansatz for the ground state of the sub-ohmic spin-boson model: An analytic theory of the localization transition, *Phys. Rev. Lett.* 107(16), 160601 (2011)
42. Q. J. Tong, J. H. An, H. G. Luo, and C. H. Oh, Quantum phase transition in the delocalized regime of the spin-boson model, *Phys. Rev. B* 84(17), 174301 (2011)
43. D. P. S. McCutcheon, N. S. Dattani, E. M. Gauger, B. W. Lovett, and A. Nazir, A general approach to quantum dynamics using a variational master equation: Application to phonon-damped Rabi rotations in quantum dots, *Phys. Rev. B* 84(8), 081305 (2011)
44. D. Ruelle, *Statistical Mechanics: Rigorous Results*, New York: Benjamin, 1969
45. R. P. Feynman, *Statistical Mechanics. A set of lectures*, Longman: Addison Wesley, 1998
46. M. D. Girardeau and R. M. Mazo, *Advances in Chemical Physics*, Vol. 24, New York: Wiley, 1973
47. R. Kubo, M. Toda, and N. Hashitsume, *Statistical Physics (II): Nonequilibrium Statistical Mechanics*, Berlin: Springer-Verlag, 1983
48. A. Nitzan, *Chemical Dynamics in Condensed Phases: Relaxation, Transfer and Reactions in Condensed Molecular Systems*, Oxford: Oxford University Press, 2006
49. R. P. Feynman and F. L. Jr Vernon, The theory of a general quantum system interacting with a linear dissipative system, *Ann. Phys.* 24, 118 (1963)
50. W. H. Zurek, Decoherence, einselection, and the quantum origins of the classical, *Rev. Mod. Phys.* 75(3), 715 (2003)
51. J. P. Paz and W. H. Zurek, Quantum limit of decoherence: Environment induced superselection of energy eigenstates, *Phys. Rev. Lett.* 82(26), 5181 (1999)
52. D. Braun, F. Haake, and W. T. Strunz, Universality of decoherence, *Phys. Rev. Lett.* 86(14), 2913 (2001)
53. W. G. Wang, J. B. Gong, G. Casati, and B. Li, Entanglement-induced decoherence and energy eigenstates, *Phys. Rev. A* 77(1), 012108 (2008)
54. C. Gogolin, Environment-induced super selection without pointer states, *Phys. Rev. E* 81(5), 051127 (2010)
55. E. N. Zimanyi and R. J. Silbey, Theoretical description of quantum effects in multi-chromophoric aggregates, *Philos. Trans. R. Soc. A* 370(1972), 3620 (2012)
56. A. Troisi and G. Orlandi, Charge-transport regime of crystalline organic semiconductors: Diffusion limited by thermal off-diagonal electronic disorder, *Phys. Rev. Lett.* 96(8), 086601 (2006)
57. T. Sakanoue and H. Sirringhaus, Band-like temperature dependence of mobility in a solution-processed organic semiconductor, *Nat. Mater.* 9(9), 736 (2010)
58. J. Singh, E. R. Bittner, D. Beljonne, and G. D. Scholes, Fluorescence depolarization in poly[2-methoxy-5-((2-ethylhexyl)oxy)-1,4-phenylenevinylene]: Sites versus eigenstates hopping, *J. Chem. Phys.* 131(19), 194905 (2009)
59. M. Bednarz, V. A. Malyshev, and J. Knoester, Temperature dependent fluorescence in disordered Frenkel chains: Interplay of equilibration and local band-edge level structure, *Phys. Rev. Lett.* 91(21), 217401 (2003)
60. J. Moix, J. Wu, P. Huo, D. Coker, and J. Cao, Efficient energy transfer in light-harvesting systems (III): The influence of the eighth bacteriochlorophyll on the dynamics and efficiency in FMO, *J. Phys. Chem. Lett.* 2(24), 3045 (2011)
61. G. T. de Laissardière, J. P. Julien, and D. Mayou, Quantum transport of slow charge carriers in quasicrystals and correlated systems, *Phys. Rev. Lett.* 97, 026601 (2006)

62. V. Coropceanu, J. Cornil, D. A. da Silva Filho, Y. Olivier, R. Silbey, and J. L. Bredas, Charge transport in organic semiconductors, *Chem. Rev.* 107(4), 926 (2007)
63. F. Ortman, F. Bechstedt, and K. Hannewald, Theory of charge transport in organic crystals: Beyond Holstein's small-polaron model, *Phys. Rev. B* 79(23), 235206 (2009)
64. S. Ciuchi, S. Fratini, and D. Mayou, Transient localization in crystalline organic semiconductors, *Phys. Rev. B* 83(8), 081202 (2011)
65. Y. Cheng and R. J. Silbey, A unified theory for charge-carrier transport in organic crystals, *J. Chem. Phys.* 128(11), 114713 (2008)
66. J. M. Moix, M. Khasin, and J. Cao, Coherent quantum transport in disordered systems (I): The influence of dephasing on the transport properties and absorption spectra on one-dimensional systems, *New J. Phys.* 15(8), 085010 (2013)
67. C. Chuang, C. K. Lee, J. M. Moix, J. Knoester, and J. Cao, Quantum diffusion on molecular tubes: Universal scaling of the 1D to 2D transition, arXiv: 1511.01198 (2015)
68. A. O. Niskanen, Y. Nakamura, and J. P. Pekola, Information entropic superconducting microcooler, *Phys. Rev. B* 76(17), 174523 (2007)
69. K. Le Hur, Kondo resonance of a microwave photon, *Phys. Rev. B* 85(14), 140506 (2012)
70. M. Galperin, M. A. Ratner, and A. Nitzan, Molecular transport junctions: Vibrational effects, *J. Phys.: Condens. Matter* 19(10), 103201 (2007)
71. J. C. Cuevas and E. Scheer, *Molecular Electronics: An Introduction to Theory and Experiment*, Singapore: World Scientific, 2010
72. D. Segal and A. Nitzan, Spin-boson thermal rectifier, *Phys. Rev. Lett.* 94(3), 034301 (2005)
73. D. Segal, Stochastic pumping of heat: Approaching the Carnot efficiency, *Phys. Rev. Lett.* 101(26), 260601 (2008)
74. J. Ren, P. Hänggi, and B. Li, Berry-phase-induced heat pumping and its impact on the fluctuation theorem, *Phys. Rev. Lett.* 104(17), 170601 (2010)
75. A. Caldeira and A. J. Leggett, Influence of dissipation on quantum tunneling in macroscopic systems, *Phys. Rev. Lett.* 46(4), 211 (1981)
76. N. B. Li, J. Ren, L. Wang, G. Zhang, P. Hänggi, and B. Li, Phononics: Manipulating heat flow with electronic analogs and beyond, *Rev. Mod. Phys.* 84(3), 1045 (2012)
77. L. Zhu, S. Kirchner, Q. M. Si, and A. Georges, Quantum critical properties of the Bose–Fermi Kondo model in a large- N limit, *Phys. Rev. Lett.* 93(26), 267201 (2004)
78. K. Saito and T. Kato, Kondo signature in heat transfer via a local two-state system, *Phys. Rev. Lett.* 111(21), 214301 (2013)
79. A. Ishizaki and G. R. Fleming, Quantum coherence in photosynthetic light harvesting, *Annu. Rev. Condens. Matter Phys.* 3(1), 333 (2012)
80. J. L. Wu, R. J. Silbey, and J. Cao, Generic mechanism of optimal energy transfer efficiency: A scaling theory of the mean first-passage time in exciton systems, *Phys. Rev. Lett.* 110(20), 200402 (2013)
81. S. F. Huelga and M. B. Plenio, Vibrations, quanta and biology, *Contemp. Phys.* 54(4), 181 (2013)
82. M. Esposito, U. Harbola, and S. Mukamel, Nonequilibrium fluctuations, fluctuation theorems, and counting statistics in quantum systems, *Rev. Mod. Phys.* 81(4), 1665 (2009)
83. T. V. Tscherbul and P. Brumer, Long-lived quasistationary coherences in a V-type system driven by incoherent light, *Phys. Rev. Lett.* 113(11), 113601 (2014)
84. J. Olsina, A. G. Dijkstra, C. Wang, and J. Cao, Can natural sunlight induce coherent exciton dynamics? arXiv: 1408.5385 (2014)
85. H. T. Quan, Y. X. Liu, C. P. Sun, and F. Nori, Quantum thermodynamic cycles and quantum heat engines, *Phys. Rev. E* 76(3), 031105 (2007)
86. M. O. Scully, K. R. Chapin, K. E. Dorfman, M. B. Kim, and A. Svidzinsky, Quantum heat engine power can be increased by noise-induced coherence, *Proc. Natl. Acad. Sci. USA* 108(37), 15097 (2011)
87. K. E. Dorfman, D. V. Voronine, S. Mukamel, and M. O. Scully, Photosynthetic reaction center as a quantum heat engine, *Proc. Natl. Acad. Sci. USA* 110(8), 2746 (2013)
88. H. E. D. Scovil and E. O. Schulz-DuBois, Three-level masers as heat engines, *Phys. Rev. Lett.* 2(6), 262 (1959)
89. J. E. Geusic, E. O. Schulz-DuBios, and H. E. D. Scovil, Quantum equivalent of the carnot cycle, *Phys. Rev.* 156(2), 343 (1967)
90. E. Geva and R. Kosloff, The quantum heat engine and heat pump: An irreversible thermodynamic analysis of the three-level amplifier, *J. Chem. Phys.* 104(19), 7681 (1996)
91. E. Boukobza and D. J. Tannor, Three-level systems as amplifiers and attenuators: A thermodynamic analysis, *Phys. Rev. Lett.* 98(24), 240601 (2007)
92. D. Gelbwaser-Klimovsky and A. Aspuru-Guzik, Strongly coupled quantum heat machines, *J. Phys. Chem. Lett.* 6(17), 3477 (2015)
93. J. Cao and R. J. Silbey, Optimization of exciton trapping in energy transfer processes, *J. Phys. Chem. A* 113(50), 13825 (2009)
94. C. Wang, J. Ren, and J. Cao, Optimal tunneling enhances the quantum photovoltaic effect in double quantum dots, *New J. Phys.* 16(4), 045019 (2014)
95. A. G. Dijkstra, C. Wang, J. Cao, and G. R. Fleming, Coherent exciton dynamics in the presence of underdamped vibrations, *J. Phys. Chem. Lett.* 6(4), 627 (2015)

Polaron effects on the performance of light-harvesting systems: a quantum heat engine perspective

This content has been downloaded from IOPscience. Please scroll down to see the full text.

2016 New J. Phys. 18 023003

(<http://iopscience.iop.org/1367-2630/18/2/023003>)

View [the table of contents for this issue](#), or go to the [journal homepage](#) for more

Download details:

IP Address: 137.132.22.253

This content was downloaded on 27/02/2016 at 07:27

Please note that [terms and conditions apply](#).



PAPER

Polaron effects on the performance of light-harvesting systems: a quantum heat engine perspective

OPEN ACCESS

RECEIVED

17 September 2015

REVISED

13 December 2015

ACCEPTED FOR PUBLICATION

17 December 2015

PUBLISHED

28 January 2016

Original content from this work may be used under the terms of the [Creative Commons Attribution 3.0 licence](#).

Any further distribution of this work must maintain attribution to the author(s) and the title of the work, journal citation and DOI.

Dazhi Xu^{1,2}, Chen Wang^{2,3}, Yang Zhao¹ and Jianshu Cao^{2,4}¹ School of Materials Science and Engineering, Nanyang Technological University, Singapore² Department of Chemistry, Massachusetts Institute of Technology, Cambridge, MA 02139, USA³ Department of Physics, Hangzhou Dianzi University, Hangzhou, Zhejiang 310018, People's Republic of China⁴ Singapore-MIT Alliance for Research and Technology, 1 CREATE Way, Singapore 138602, SingaporeE-mail: jianshu@mit.edu**Keywords:** quantum open system, heat engine, strong coupling**Abstract**

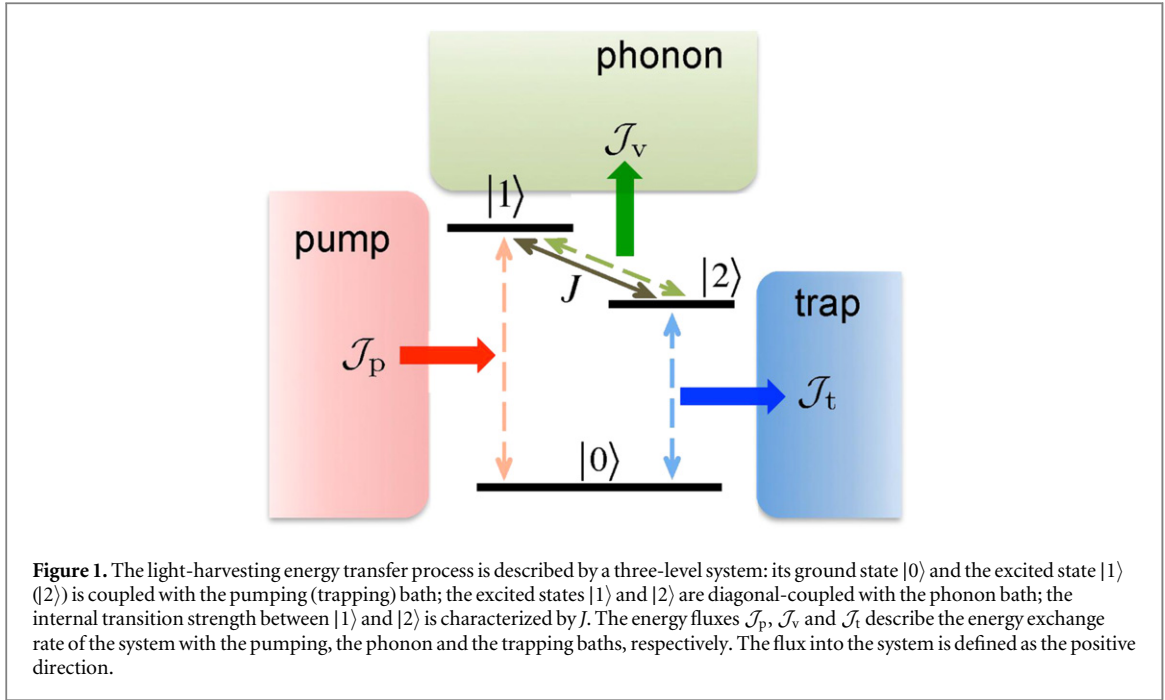
We explore energy transfer in a generic three-level system, which is coupled to three non-equilibrium baths. Built on the concept of quantum heat engine, our three-level model describes non-equilibrium quantum processes including light-harvesting energy transfer, nano-scale heat transfer, photo-induced isomerization, and photovoltaics in double quantum-dots. In the context of light-harvesting, the excitation energy is first pumped up by sunlight, then is transferred via two excited states which are coupled to a phonon bath, and finally decays to the reaction center. The efficiency of this process is evaluated by steady state analysis via a polaron-transformed master equation; thus the entire range of the system-phonon coupling strength can be covered. We show that the coupling with the phonon bath not only modifies the steady state, resulting in population inversion, but also introduces a finite steady state coherence which optimizes the energy transfer flux and efficiency. In the strong coupling limit, the steady state coherence disappears and the efficiency recovers the heat engine limit given by Scovil and Schultz-Dubois (1959 *Phys. Rev. Lett.* **2** 262).

1. Introduction

With the rapid developments in measurement and manipulation of microscopic systems, quantum effects such as coherence and entanglement are often utilized to enhance the performance of microscopic devices. Even in biological systems, both experiments [1] and theoretical models [2, 3] reveal that the long-lived quantum coherence may play an important role in highly efficient energy and electron transfer processes. How biological systems, such as light-harvesting complex, preserve such long-lived coherence and how nature benefits from the coherence are two key questions that define the emerging field of quantum biology.

Taking a three-level system as a generic theoretical model, many interesting mechanisms can be well demonstrated and understood. Recently, the sunlight-induced exciton coherence is studied in a V-configuration three-level model [4, 5]. An interesting idea is to consider the energy transfer process from the perspective of heat engine [6]. For example, the coherence introduced by an auxiliary energy level can enhance the heat engine power [7, 8]. The early work considering a three-level maser model as a Carnot engine was carried out by Scovil and Schulz-DuBois [9, 10], yielding the heat engine efficiency η_0 and its relation with the Carnot efficiency. Later papers elaborately reexamined the dynamics of this model by the Lindblad master equation and showed that the thermodynamic efficiency η_0 is achieved when the output light-field is strongly coupled with the three-level system [11–13]. The quantum heat engine provides us a heuristic perspective to better understand the basic physical processes in energy transfer and presents useful insight to enhance the efficiency and output power in small systems [14–17].

In this paper, we study the polaron effects of a phonon bath on the energy transfer flux and efficiency in a generic three-level model. The energy transfer efficiency is defined as the ratio between the trapping and pumping fluxes. The canonical distribution of a thermal equilibrium system requires a negligible coupling



between the system and its environment. As the coupling strength grows, the steady state of the system will no longer be canonical [18–22]. This non-canonical state actually introduces the steady state coherence into the system without refereeing to specific forms of light–matter interaction or designing exotic system configurations. The bath-induced coherent effect is investigated by the polaron-transformed Redfield equation (PTRE) [23, 24], which bridges both the weak and strong system–bath coupling regions. The difference between the steady state efficiency and strong coupling limit η_0 depends strongly on the phonon-induced coherence. Taking into account of the behavior of both the flux and efficiency, we are able to optimize coupling and temperature in designing optimal artificial energy transfer systems.

In this paper, we first introduce the three-level model and its non-equilibrium environment in section 2, and then formulate the PTRE in section 3. In section 4, the polaron effects of phonon-bath on the energy transfer flux and efficiency are studied in detail. We summarize our results in the last section. We leave the detailed derivation and properties of the PTRE in the appendix.

2. Three-level system model

2.1. Model system

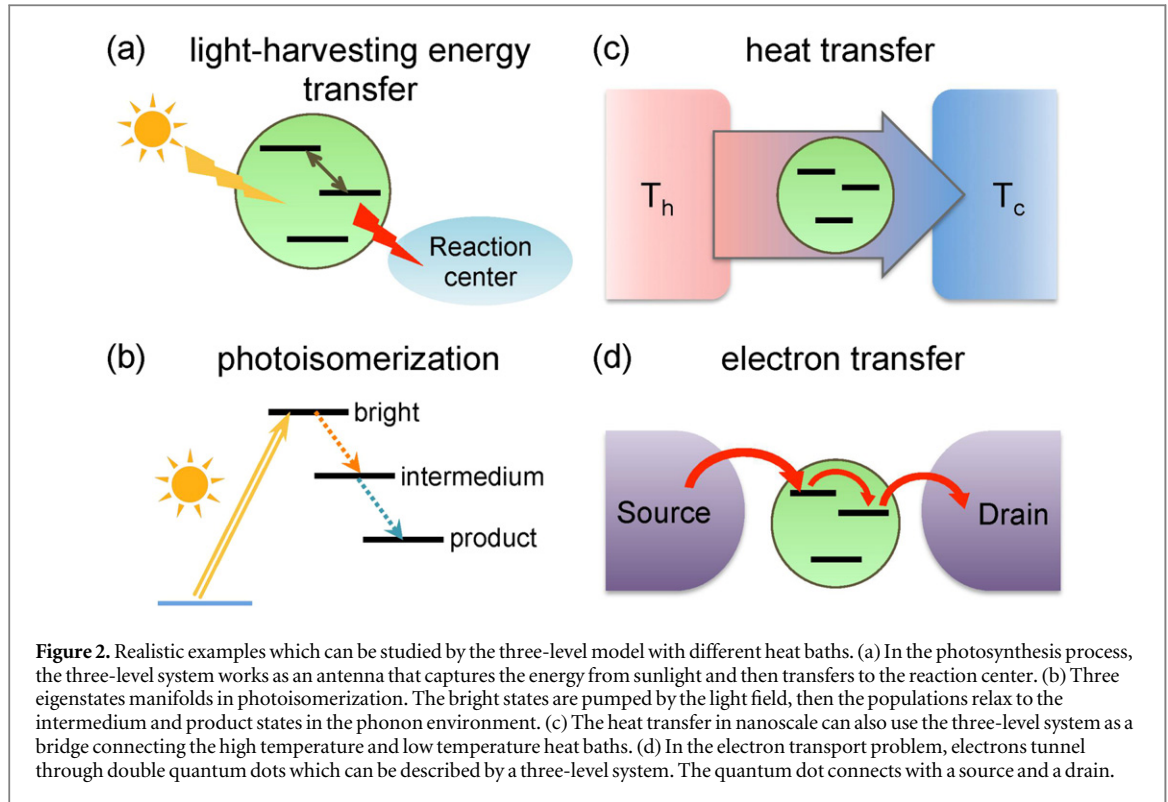
We consider the energy transfer process in the three-level system illustrated in figure 1. The site energy of the ground state $|0\rangle$ is set to zero. The two excited energy levels $|1\rangle$ and $|2\rangle$ form a two-level system (TLS, in the following the TLS is referred to the two excited states), with the corresponding site energy ϵ_1 and ϵ_2 . The transition due to the dipole–dipole interaction is characterized by J . Then the three-level system is modeled by the Hamiltonian H_0 as:

$$H_0 = \sum_{i=1,2} \epsilon_i |i\rangle \langle i| + \frac{J}{2} (|1\rangle \langle 2| + |2\rangle \langle 1|). \quad (1)$$

We are interested in the transfer process in the single excitation subspace: the three-level system is firstly excited to state $|1\rangle$ by a photon field, then the excitation is transferred to state $|2\rangle$ through J (mediated by phonon modes), and finally the excitation decays to the ground state $|0\rangle$ via spontaneous radiation. The pumping and trapping processes are modeled by the interaction with the two independent photon baths, which are coupled separately with two transitions $|0\rangle \leftrightarrow |1\rangle$ and $|0\rangle \leftrightarrow |2\rangle$. The Hamiltonian of the photon baths and their interactions with the three-level system are given by

$$H_p = \sum_k \omega_{pk} a_{pk}^\dagger a_{pk} + (g_{pk} a_{pk}^\dagger |0\rangle \langle 1| + \text{h.c.}), \quad (2)$$

$$H_t = \sum_k \omega_{tk} a_{tk}^\dagger a_{tk} + (g_{tk} a_{tk}^\dagger |0\rangle \langle 2| + \text{h.c.}), \quad (3)$$



where ω_{ik} ($i = p, t$) is the eigen frequency of the bath mode described by the creation (annihilation) operator a_{ik}^\dagger (a_{ik}), and its coupling strength to the excited state is g_{ik} . We note that the rotating wave approximation is applied in the system–bath interaction term. A phonon bath with creation and annihilation operators b_k^\dagger and b_k of the bath mode ω_{vk} is coupled to the TLS via diagonal interaction with the coupling strength of f_k . Thus, the phonon part is described by

$$H_v = \sum_k \omega_{vk} b_k^\dagger b_k + (|1\rangle\langle 1| - |2\rangle\langle 2|) \sum_k (f_k b_k^\dagger + \text{h.c.}). \quad (4)$$

This microscopic three-level system immersed in the non-equilibrium environment was studied as a quantum heat pump phenomenologically without considering the details of the system–bath coupling [10]. In the case that the phonon bath is replaced by a single driving mode strongly coupled to the system, the dynamic steady states have been solved and the efficiency is given by $\eta_0 = \epsilon_2/\epsilon_1$ [12, 13]. In reality, the three-level model can be realized in both nature and laboratory. Taking the energy transfer process in photosynthetic pigment for example (figure 2(a)), different baths could arise from different sources: the pumping light field (such as the sunlight photons) is considered as a high temperature boson bath; the trapping bath is formed by the surrounding electromagnetic environment which models the energy transfer to the reaction center; and the phonon bath with inverse temperature β_v describes the phonon modes coupled with the excited states. In addition, such a three-level (or more intermediate energy levels) system is used to describe photoisomerization (figure 2(b)), nanoscale heat transfer [25] (figure 2(c)) or photovoltaic current in double quantum dots [26] (figure 2(d)).

In this paper, we focus on the effects of the phonon modes on energy flux and efficiency. Usually when the system–phonon bath coupling strength is not weak, the Bloch–Redfield equation approach cannot be applied. Therefore, we will introduce the PTRE [23, 24], which gives reliable results from the weak to strong coupling region using super Ohmic bath spectrum with large cut-off frequency ω_c , to study the bath-induced coherent effects of this quantum system. The validity of the PTRE has been verified by comparing with the numerical path integral method [21] and time-convolutionless polaron master equation [27, 28].

2.2. Definitions of energy flux and transfer efficiency

We are interested in the energy transfer flux and efficiency of the three-level system at its non-equilibrium steady state. The steady state solution can be obtained by the master equation formally written as

$$\frac{d\rho(t)}{dt} = (\mathcal{L}_0 + \mathcal{L}_p + \mathcal{L}_v + \mathcal{L}_t)\rho(t), \quad (5)$$

which describes the dynamics of the reduced density matrix (RDM) $\rho(t)$ of the three-level system. The Liouville operator \mathcal{L}_0 denotes the non-dissipative term, \mathcal{L}_p , \mathcal{L}_v and \mathcal{L}_t denote the dissipation effects associated with the pumping, phonon coupling, and trapping, respectively.

To quantitatively investigate the energy transfer process, we define the steady state energy fluxes by calculating the energy change of the three-level system

$$\begin{aligned}\dot{E}(\infty) &= \text{Tr}_s \left[\frac{d\rho(t)}{dt} H_0 \right] \Big|_{t=\infty} = \sum_{i=p,v,t} \text{Tr}_s [\mathcal{L}_i [\rho(\infty)] H_0] \\ &\equiv \mathcal{J}_p + \mathcal{J}_v + \mathcal{J}_t.\end{aligned}\quad (6)$$

It can be shown that $\text{Tr}_s [\mathcal{L}_0 H_0] = 0$. The three energy fluxes \mathcal{J}_i , $i = p, v, t$ are defined with respect to their corresponding dissipation operator \mathcal{L}_i . These energy fluxes have clear physical meanings of the energy exchange rate with the pumping field, phonon environment, and trapping field, respectively. In this work, we are interested in the steady state, in equation (6) the fluxes are calculated with $\rho(\infty)$, which is obtained by solving $\dot{\rho}(t) = 0$. Straightforwardly, we define the energy transfer efficiency by

$$\eta = \left| \frac{\mathcal{J}_t(\infty)}{\mathcal{J}_p(\infty)} \right|, \quad (7)$$

which is the ratio between the output and the input energy fluxes.

Without losing generality, we assume the pumping (trapping) bath is weakly coupled with the system and can be described phenomenologically by the local Liouville operator of the Lindblad form

$$\begin{aligned}\mathcal{L}_i[\rho] &= \frac{\gamma_i}{2} [(n_i + 1)(2O_i^- \rho O_i^+ - \{O_i^+ O_i^-, \rho\}) \\ &\quad + n_i(2O_i^+ \rho O_i^- - \{O_i^- O_i^+, \rho\})],\end{aligned}\quad (8)$$

where $i = p, t$ refers to the two photon baths, γ_i and n_i are the corresponding decay rate and average photon number, and the system operators are defined as $O_p^+ = |1\rangle\langle 0|$, $O_t^+ = |2\rangle\langle 0|$. The system–phonon bath coupling will be treated more rigorously as we are interested in how this coupling affects the energy transfer over a broad range. To achieve this goal, we apply the PTRE equation, which will be introduced in the following section.

3. PTRE

The Redfield master equation is valid up to the second-order perturbation of the system–bath interaction. In order to go beyond this weak coupling limit, polaron transformation is introduced to incorporate the high-order system–bath interaction into the dynamics of the system. Here we focus on the coupling strength between the system and phonon bath, and the polaron transformation is only related to the two excited states. Therefore it is convenient to consider the TLS first, then the resulting Liouville operator describing the TLS dissipative process can be incorporated into the dynamics of the three-level system.

We employ the Pauli matrix $\sigma_x = |1\rangle\langle 2| + |2\rangle\langle 1|$ and $\sigma_z = |1\rangle\langle 1| - |2\rangle\langle 2|$, and define the polaron transformation

$$\tilde{H}' = e^{-i\sigma_z B/2} H' e^{i\sigma_z B/2} = \tilde{H}_0 + \tilde{H}_b + \tilde{V}, \quad (9)$$

where $H' = H_0 + H_v$ is the Hamiltonian of the TLS with the phonon bath, the collective bath operator is $B = 2i \sum_k (f_k b_k^\dagger - f_k^* b_k) / \omega_{vk}$ and

$$\tilde{H}_0 = \frac{\epsilon}{2} \sigma_z + \frac{J}{2} \kappa \sigma_x, \quad (10)$$

$$\tilde{H}_b = \sum_k \omega_{vk} b_k^\dagger b_k - \sum_k \frac{|f_k|^2}{\omega_{vk}}, \quad (11)$$

$$\tilde{V} = \frac{J}{2} [\sigma_x (\cos B - \kappa) + \sigma_y \sin B]. \quad (12)$$

The transformed system–bath interaction is \tilde{V} and $\epsilon = \epsilon_1 - \epsilon_2$. The expectation value of the bath operator

$$\begin{aligned}\kappa &= \text{Tr}_b [\rho_b' \cos B] \\ &= \exp \left[- \int_0^\infty d\omega \frac{J(\omega)}{\pi \omega^2} \left(n_v(\omega) + \frac{1}{2} \right) \right]\end{aligned}\quad (13)$$

is subtracted from \tilde{V} as a renormalization factor, with $\rho_b' = \exp(-\beta_v \tilde{H}_b) / \text{Tr}_b [\exp(-\beta_v \tilde{H}_b)]$ the thermal state of the phonon bath and $n_v(\omega) = [\exp(\beta_v \omega) - 1]^{-1}$ the average phonon number. The spectrum function is

chosen to be super-Ohmic as

$$J(\omega) = 4\pi \sum_k |f_k|^2 \delta(\omega - \omega_k) = \alpha \pi \omega^3 \omega_c^{-2} e^{-\omega/\omega_c}, \quad (14)$$

where ω_c is the cut-off frequency and α is a dimensionless parameter characterizing the system–bath coupling which is proportional to λ/ω_c (λ is the reorganization energy). It can be verified that the thermal average of \tilde{V} is zero, i.e., \tilde{V} is of the order of bath fluctuations and thus is a reliable perturbation parameter. Based on this consideration, the Born–Markov approximation is applied to derive the PTRE in the Schrodinger picture as

$$\begin{aligned} \frac{d\rho'_s(t)}{dt} = & -i[\tilde{H}_0, \rho'_s(t)] - \sum_{ij=z,\pm} [\Gamma_{ij}^+ \tau_i \tau_j \rho'_s(t) + \Gamma_{ji}^- \rho'_s(t) \tau_j \tau_i \\ & - \Gamma_{ji}^- \tau_i \rho'_s(t) \tau_j - \Gamma_{ij}^+ \tau_j \rho'_s(t) \tau_i]. \end{aligned} \quad (15)$$

Here, Γ_{ij}^\pm is defined by the bath correlation function. We denote ρ'_s (ρ_s) as the RDM of the TLS in the polaron (local) frame, and define a new set of Pauli operator

$$\tau_z = |+\rangle\langle+| - |-\rangle\langle-|, \quad (16)$$

$$\tau_+ = |+\rangle\langle-|, \tau_- = |-\rangle\langle+|, \quad (17)$$

where $\tilde{H}_0 | \pm \rangle = \epsilon_\pm | \pm \rangle$. The detailed derivation of the PTRE can be found in appendix A.

The PTRE was firstly introduced by Silbey and coworkers [23, 24], and has been widely used in solving the strong system–bath coupling problems. The validity of the PTRE in the whole range of coupling strength requires the bath cut-off frequency should be much larger than the internal coupling strength, $\omega_c \gg J$; if $\omega_c \lesssim J$, the PTRE only works well in the strong coupling regime [21]. To extend the valid regime of the polaron approach even for small ω_c , a variational polaron transformation can be applied, where f_k in the bath operator B is substituted with a variational parameter [21, 24, 29]. Moreover, it will be shown in B that the results given by PTRE are consistent with those given by the Redfield equation in the weak coupling limit and the Fermi's golden rule (or Frster theory) in the strong coupling limit [21, 25, 26]. Therefore, the PTRE smoothly connects the two limits, and provides a useful tool to study the intermediate coupling region where there are usually no reliable approximation methods.

For further discussion on the property of the entire three-level system with the other two weakly coupled photon baths, equation (15) for the two excited states is transformed back into the local basis and rewritten as $[\dot{\rho}'_s(t)]_{ij} = \sum_{mn} [\mathcal{L}_v]_{(ij, mn)} [\rho'_s(t)]_{mn}$. Then the expressions for the Liouville operator \mathcal{L}_v are obtained accordingly. The relations between the elements of $\rho'_s(t)$ and $\rho_s(t)$ are also given in appendix A.

The Bloch-form equation of the three-level system is derived following from equation (5). One thing should be noted, the population conservation of the TLS gives $[\rho_s(t)]_{11} + [\rho_s(t)]_{22} = 1$; while for the three-level system, the ground state population should be included and population conservation becomes $\rho_{00}(t) + \rho_{11}(t) + \rho_{22}(t) = 1$, where we denote $\rho_{ij}(t) = \langle i | \rho(t) | j \rangle$. The Liouville operator \mathcal{L}_v which considers the polaron effects has been obtained from the PTRE of the TLS. The effects of the pumping and trapping baths are described by the Lindblad operator \mathcal{L}_p and \mathcal{L}_t defined in equation (8). Therefore, the PTRE for the three-level system is given as

$$\frac{d}{dt} \begin{pmatrix} \rho_{11}(t) - \rho_{22}(t) \\ \rho_{11}(t) + \rho_{22}(t) \\ \Re[\rho_{12}(t)] \\ \Im[\rho_{12}(t)] \end{pmatrix} = -\bar{M} \begin{pmatrix} \rho_{11}(t) - \rho_{22}(t) \\ \rho_{11}(t) + \rho_{22}(t) \\ \Re[\rho_{12}(t)] \\ \Im[\rho_{12}(t)] \end{pmatrix} + \frac{J^2}{4} \begin{pmatrix} \gamma_p n_p - \gamma_t n_t \\ \gamma_p n_p + \gamma_t n_t \\ 0 \\ 0 \end{pmatrix}, \quad (18)$$

where the matrix \bar{M} is shown in appendix B. The equations for the off-diagonal terms $\rho_{01}(t)$ and $\rho_{02}(t)$ are decoupled from equation (18) and not related with the energy flux and transfer efficiency, thus will not involve in the following discussion.

4. Energy transfer flux and efficiency

4.1. Steady state flux

The steady state of the three-level system can be easily obtained from equation (18), which incorporates the polaron effects of the phonon bath. Then the steady state energy fluxes defined in equation (6) are straightforwardly given as

$$\mathcal{J}_p = \epsilon_1 \gamma_p [n_p \rho_{00} - (n_p + 1) \rho_{11}] - \frac{J \gamma_p}{2} (n_p + 1) \Re[\rho_{12}], \quad (19)$$

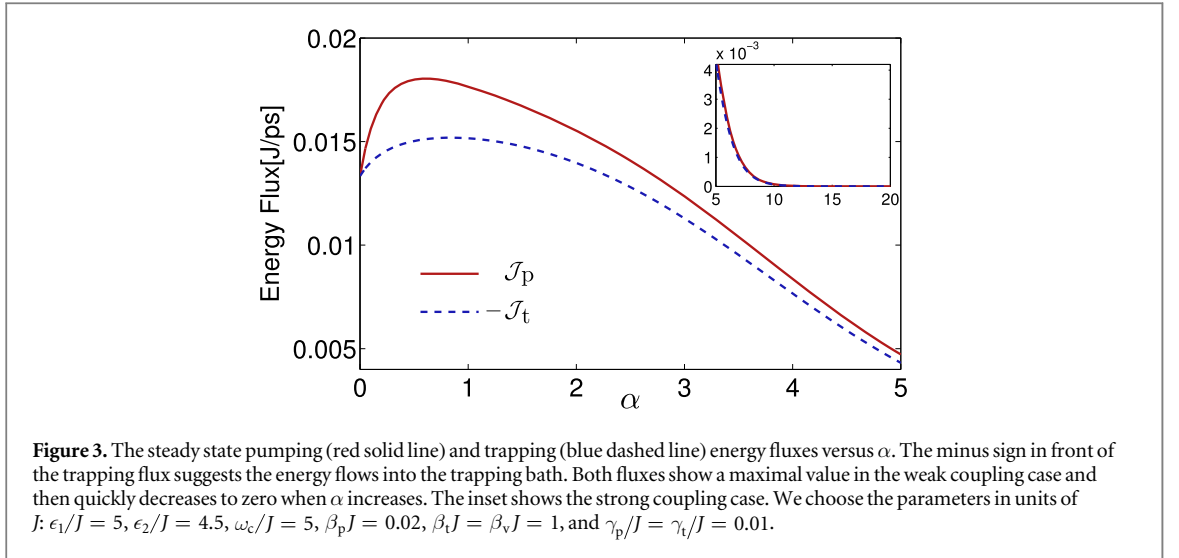


Figure 3. The steady state pumping (red solid line) and trapping (blue dashed line) energy fluxes versus α . The minus sign in front of the trapping flux suggests the energy flows into the trapping bath. Both fluxes show a maximal value in the weak coupling case and then quickly decreases to zero when α increases. The inset shows the strong coupling case. We choose the parameters in units of J : $\epsilon_1/J = 5$, $\epsilon_2/J = 4.5$, $\omega_c/J = 5$, $\beta_p J = 0.02$, $\beta_t J = \beta_v J = 1$, and $\gamma_p/J = \gamma_t/J = 0.01$.

$$\mathcal{J}_t = \epsilon_2 \gamma_t [n_t \rho_{00} - (n_t + 1) \rho_{22}] - \frac{J \gamma_t}{2} (n_t + 1) \Re[\rho_{12}], \quad (20)$$

where we denote the steady state elements of RDM by $\rho_{ij} = \langle i | \rho_s(\infty) | j \rangle$ for brevity. Figure 3 presents energy fluxes with respect to α . In the extreme case that the system bath coupling is switched off ($\alpha = 0$), there is no loss of excitation energy, which results in $\mathcal{J}_p = -\mathcal{J}_t$, suggesting the input energy flux from the pump completely flows into the trap through the three-level system (note that we chose the positive direction as that the flux flows into the system). When the coupling turns on, a portion of energy flux leaks into the phonon bath thus $\mathcal{J}_p > -\mathcal{J}_t$. Both the pumping and trapping energy fluxes reach their optimal values in the intermediate coupling region and decrease to zero when the coupling strength is strong.

In the context of heat engine, the trapping energy flux \mathcal{J}_t in our model corresponds to the output power and \mathcal{J}_p corresponds to the input power. Usually, the power of a heat engine is small when the efficiency is high. Particularly, at the maximal efficiency, all the processes are required to be quasi-static and take infinite time, and thus the power will be zero. To balance the conflict between the efficiency and power, much work has been done to study the efficiency at maximum power [30–32]. In the following, we will calculate the energy transfer efficiency of our system and show its competitive relation with the trapping flux, in analogy to the efficiency and power in the heat engine.

4.2. Steady state efficiency

Before presenting the result of efficiency defined in equation (7), we begin with the analysis of the limiting cases. The first term on the right side of equations (19) and (20) depends only on the populations of the three-level system, and the second term represents the contribution of the off-diagonal terms (coherence in the local basis). As we show in figure C1 of appendix C, the steady state coherence in the local bases ρ_{12} vanishes in the strong coupling limit, then the efficiency is completely determined by the populations. According to the steady state solution of the second equation in equation (18), we obtain the relation

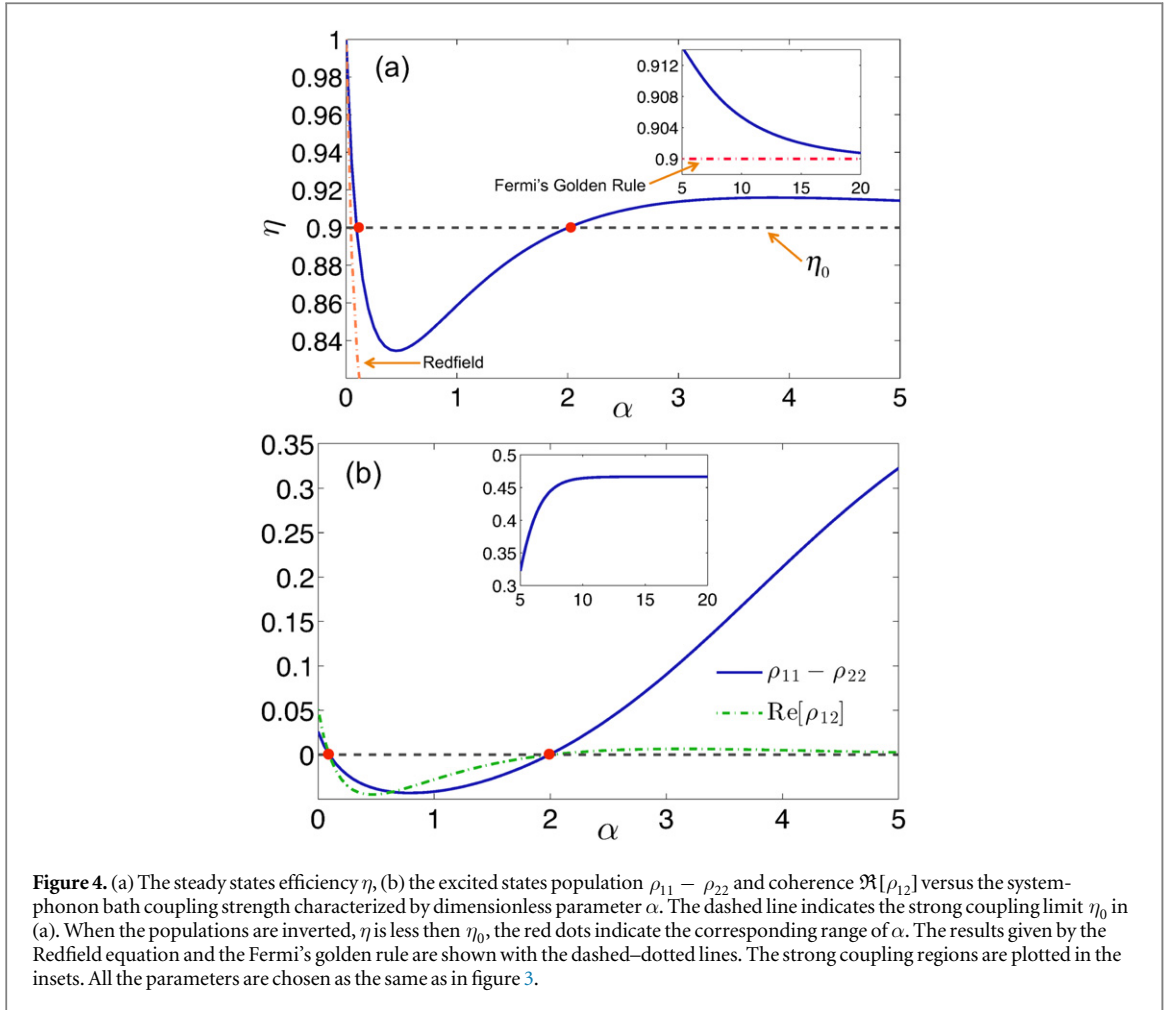
$$\gamma_p [n_p \rho_{00} - (n_p + 1) \rho_{11}] = \gamma_t [(n_t + 1) \rho_{22} - n_t \rho_{00}]. \quad (21)$$

With this relation, the efficiency in the strong coupling limit reads

$$\eta \approx -\frac{\epsilon_2 \gamma_t [(n_t + 1) \rho_{22} - n_t \rho_{00}]}{\epsilon_1 \gamma_p [(n_p + 1) \rho_{11} - n_p \rho_{00}]} = \frac{\epsilon_2}{\epsilon_1}. \quad (22)$$

This result indicates that when the coherence is negligible due to the strong system-phonon coupling, the energy transfer efficiency η approaches η_0 , which is consistent with the key result of [12]. We notice that equation (21) shows that the net rate of pumping one excitation to $|1\rangle$ equals to the net rate of trapping one excitation from $|2\rangle$ to $|0\rangle$. In general, the efficiency is closely related to the phonon bath induced coherence [33] of the excited states. If we require the system outputs positive energy, i.e., $\gamma_t (n_t + 1) \rho_{22} > \gamma_t n_t \rho_{00}$, then according to equations (19)–(21), $\Re[\rho_{12}] > 0$ leads to $\eta > \eta_0$ and vice versa.

According to our discussion of the flux in the last subsection, when the coupling strength $\alpha = 0$, the energy transfer efficiency $\eta = 1$ because there is no loss of energy flux. When the coupling strength gradually increases, the efficiency decreases. However, after reaching its minimum value, the efficiency starts to rise with α , which is shown in figure 4(a). The increase of efficiency assisted by noise was studied extensively in the context of energy transfer in light-harvesting systems [34–36]. As we further increase α , the efficiency grows beyond the strong



coupling limit η_0 and then gradually approaches this limit from above. The strong coupling region is plotted in the inset of figure 4(a).

Interestingly, we find population inversion of the two excited states in the regimes of $\eta > \eta_0$. We plot the population difference between states $|1\rangle$ and $|2\rangle$ in figure 4(b). In the intermediate coupling region indicated between the two red dots, the steady state population satisfies $\rho_{11} < \rho_{22}$ (the effective temperature associates with these two states is positive), the corresponding efficiency η is less than η_0 as shown in figure 4(a). On the contrary, outside this intermediate region, i.e., when the coupling is either very weak or very strong, the populations are inverted $\rho_{11} > \rho_{22}$ (the effective temperature is negative); meanwhile η increase beyond η_0 . In the local basis, the population and coherence are coupled with each other due to the polaron effects: the population inversion happens when $\Re[\rho_{12}] < 0$ (figure 4(b)). The fact that the population and coherence in the local basis have similar behavior can be explained from equation (A9) and equation (A10). Here, the coherence $\langle \tau_x(t) \rangle$ in the polaron basis is negligibly small (see the inset of figure C1 in appendix C) to have significant effects, then the terms $\langle \sigma_z \rangle = \rho_{11} - \rho_{22}$ and $\langle \sigma_x \rangle = 2\Re[\rho_{12}]$ are both determined by $\langle \tau_z \rangle$.

In figure 4(a), we also compare the efficiency η calculated by the PTRE method with those predicted by the Redfield equation and the Fermi's golden rule approaches. As we mentioned before, in the weak and strong coupling limits, the PTRE method agrees with the Redfield equation and the Fermi's golden rule, respectively, and it connects these two limits with a non-trivial minimum which is related to the coherence in the local basis.

4.3. Further discussions

4.3.1. Kinetic models

In the strong coupling regime, we can map this energy transfer process into a simple excitation kinetic model as shown in figure 5(a). Each step of energy transfer is described by an effective flux ($\mathcal{J}_p^{\text{eff}}$, $\mathcal{J}_v^{\text{eff}}$ and $\mathcal{J}_t^{\text{eff}}$). The relaxation of the two excited states is characterized by the rate γ_z , which is defined in equation (C2) of appendix C. As shown in figure 5(b), the effective transfer flux $\mathcal{J}_v^{\text{eff}}$ between the two excited states is approximately proportional to the relaxation rate γ_z . When $\mathcal{J}_v^{\text{eff}}$ (or γ_z) is smaller than the trapping flux $\mathcal{J}_t^{\text{eff}}$ (or γ_t), the excitation in excited states will be quickly captured by the trapping field without enough time to first get

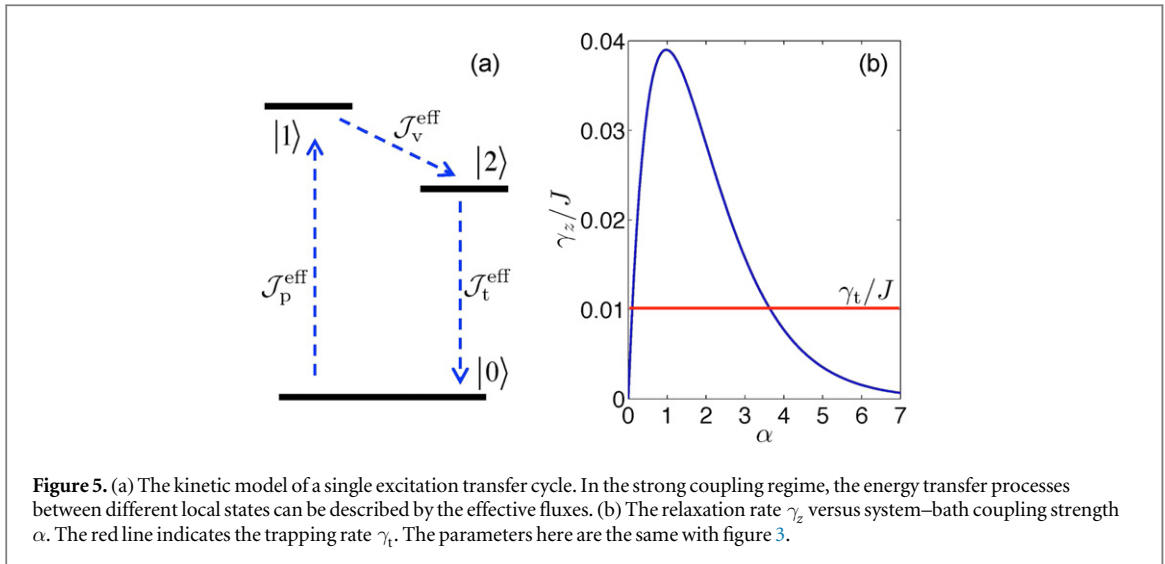


Figure 5. (a) The kinetic model of a single excitation transfer cycle. In the strong coupling regime, the energy transfer processes between different local states can be described by the effective fluxes. (b) The relaxation rate γ_z versus system–bath coupling strength α . The red line indicates the trapping rate γ_t . The parameters here are the same with figure 3.

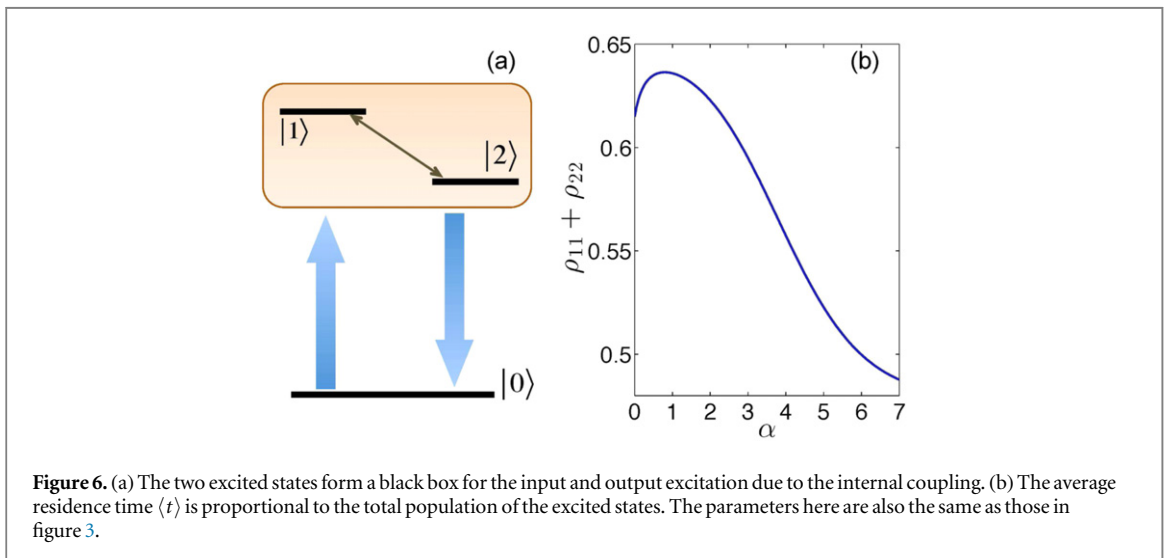


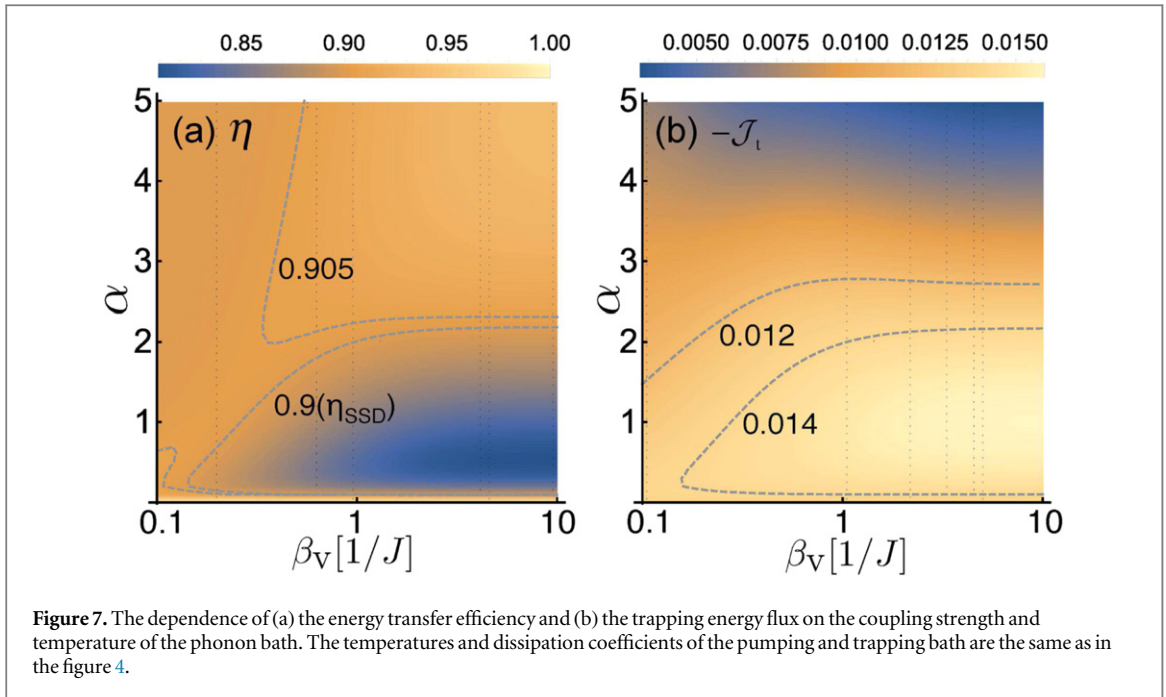
Figure 6. (a) The two excited states form a black box for the input and output excitation due to the internal coupling. (b) The average residence time $\langle t \rangle$ is proportional to the total population of the excited states. The parameters here are also the same as those in figure 3.

equilibrated with the phonon bath. Consequently, the populations of the two excited states are inverted and the real part of the coherence becomes negative. This phenomenological mechanism explains why the efficiency η is higher than η_0 in the strong coupling limit.

When the system–bath coupling strength becomes weaker, the local basis frame is no longer a good option for the kinetic picture. The two excited states couple with each other and can be together considered as an excited state manifold, as shown in figure 6(a). The single excitation carrying certain amount of energy passes through the excited states $|1\rangle$ and $|2\rangle$, and its average residence time $\langle t \rangle$ in the excited states is negatively correlated with the transfer efficiency (in analogy to the light-harvesting efficiency in [36, 37]): i.e., the longer the excitation stays in the excited states, the more energy will be lost to the phonon bath, and the lower energy transfer efficiency will be. During a cycle that the single excitation starts from $|0\rangle$ and finally returns to $|0\rangle$, the average residence time $\langle t \rangle$ is proportional to the excited states population $\rho_{11} + \rho_{22}$ at the steady states, as shown in figure 6(b). Though not quantitatively exact, this kinetic model qualitatively explains the local minimal of the efficiency η via the average residence time $\langle t \rangle \sim \rho_{11} + \rho_{22}$.

4.3.2. Temperature dependence

Besides the system–phonon bath coupling strength, the temperature of the phonon bath also affects the energy transfer process, as shown in the two-dimensional contours of energy transfer efficiency (figure 7(a)) and trapping energy flux (figure 7(b)). The efficiency behaves the same at the high phonon bath temperature as in the strong coupling. In the high temperature limit, even when the coupling strength is weak, the efficiency is still close to η_0 . As seen from equation (13), in either limit $\alpha \rightarrow \infty$ or $\beta_v \rightarrow 0$, the renormalization factor $\kappa \rightarrow 0$; therefore, except for the weak coupling and low temperature case, the efficiency η does not change obviously.



The trapping energy flux has a different temperature dependences for weak and strong system–bath couplings. The flux $-\mathcal{J}_t$ grows (goes down) with descending β_v when α is large (small). Moreover, $-\mathcal{J}_t$ does not sensitively depend on β_v with small α in contrast with the efficiency. When the coupling α is around 1, the flux $-\mathcal{J}_t$ changes no more than 20% in amplitude comparing with its maximum. The optimization of the efficiency and the trapping flux can be achieved in two different regimes: (1) The coupling strength is weak and the temperature of the phonon bath is high. (2) The coupling strength is medium ($\alpha \sim 2.5$) and the bath temperature is low ($\beta_v > 1$). The first regime corresponds to the high temperature classical limit, and the second regime corresponds to low-temperature quantum regime, where bath-induced coherence enhances the energy transfer process.

5. Conclusion

In this paper we use the PTRE to analyse the effects of the phonon bath on the energy transfer process in a generic three-level model. As a quantitative method, the PTRE can reliably describe the dependence of the steady state coherence on the system–bath coupling strength ranging from the weak to strong coupling regime. Our analysis shows that the steady state coherence between the two excited states is crucial to the energy transfer efficiency. When the effective temperature of the excited states is negative (populations are inverted), the coherence carries a positive real part and enhances the efficiency beyond the strong coupling limit η_0 . On the contrary, if the effective temperature is positive (populations are not inverted), the coherence carries a negative real part and is detrimental to the efficiency. The energy flux and efficiency compete with each other and cannot reach maximum simultaneously; however, the study of their behaviors with respect to the coupling strength and temperature provides the key information about how to make an optimal compromise between the two quantities. We will consider how to use quantum control to optimize the energy transfer process in the future study.

Acknowledgments

DX and YZ were supported by the National Research Foundation, Republic of Singapore, through the Competitive Research Program (CRP) under Project No. NRF-CRP5-2009-04. JC acknowledges the National Science Foundation (NSF) of the US (Grant No. CHE-1112825). CW has been supported by the Singapore-MIT Alliance for Research and Technology (SMART).

Appendix A. Secular-Markovian Redfield equation in the polaron frame

The two excited states coupled with the phonon bath is described by the Hamiltonian in equations (1) and (4), which is broadly studied as the spin-boson model. Via the polaron transformation given in equation (9), the system–bath coupling is effectively weakened to the order of the thermal-fluctuation, hence the second-order perturbation theory can be applied. With the secular-Markov approximation, the PTRE for spin-boson model in the interaction picture is given by

$$\frac{d\rho_s^{II}(t)}{dt} = - \int_0^\infty ds \text{Tr}_b \{ [\tilde{V}(t), [\tilde{V}(t-s), \rho_s^{II}(t) \otimes \rho_b']] \}, \quad (\text{A1})$$

which can be further written in the Schrodinger picture as equation (15)

$$\begin{aligned} \frac{d\rho_s'(t)}{dt} = & -i[\tilde{H}_0, \rho_s'(t)] - \sum_{i,j=z,\pm} [\Gamma_{ij}^+ \tau_i \tau_j \rho_s'(t) + \Gamma_{ji}^- \rho_s'(t) \tau_j \tau_i \\ & - \Gamma_{ji}^- \tau_i \rho_s'(t) \tau_j - \Gamma_{ij}^+ \tau_j \rho_s'(t) \tau_i]. \end{aligned}$$

Here, the Pauli operators τ_i defined by the eigenstates of \tilde{H}_0 are given in equations (16) and (17), and

$$|+\rangle = \cos \frac{\theta}{2} |1\rangle + \sin \frac{\theta}{2} |2\rangle, \quad (\text{A2})$$

$$|-\rangle = \sin \frac{\theta}{2} |1\rangle - \cos \frac{\theta}{2} |2\rangle, \quad (\text{A3})$$

where $\tan \theta = \kappa J / \epsilon$. The dissipation rates Γ_{ij}^\pm are related to the bath correlation functions

$$\Gamma_{ij}^\pm = \frac{\Delta_\kappa^2}{4} \int_0^\infty dt \langle \xi_i(\pm t) \xi_j(0) \rangle, \quad (\text{A4})$$

with

$$\xi_z(t) = \sin \theta [\cos B(t) - \kappa], \quad (\text{A5})$$

$$\xi_\pm(t) = -e^{\pm i \Delta_\kappa t} [\cos \theta [\cos B(t) - \kappa] \mp i \sin B(t)], \quad (\text{A6})$$

where $\Delta_\kappa = \sqrt{\epsilon^2 + (\kappa J)^2}$ and $B(t) = e^{i\tilde{H}_0 t} B e^{-i\tilde{H}_0 t}$.

To transform equation (15) back into the local frame, we express the elements of the RDM $\rho_s'(t)$ and $\rho_s(t)$ by the average of the Pauli operators $\langle \tau_{z,\pm}(t) \rangle \equiv \text{Tr}_s[\rho_s'(t) \tau_{z,\pm}]$ and $\langle \sigma_{z,\pm}(t) \rangle \equiv \text{Tr}_s[\rho_s(t) \sigma_{z,\pm}]$. As σ_z commutes with the polaron-transformation, the diagonal term $\langle \sigma_z(t) \rangle$ is easily to obtained from $\rho_s'(t)$,

$$\begin{aligned} \langle \sigma_z(t) \rangle &= \text{Tr}_{s+b}[\rho_{\text{tot}}(t) \sigma_z] = \text{Tr}_s[\rho_s(t) \sigma_z] \\ &= \text{Tr}_{s+b}[\rho_{\text{tot}}'(t) \sigma_z] = \text{Tr}_s[\rho_s'(t) \sigma_z], \end{aligned} \quad (\text{A7})$$

where $\rho_{\text{tot}}(t)$ is the total density matrix for the TLS and its bath, $\rho_s(t) = \text{Tr}_b[\rho_{\text{tot}}(t)]$ and $\rho_{\text{tot}}'(t) = e^{-i\sigma_z B/2} \rho_{\text{tot}}(t) e^{i\sigma_z B/2}$ is the polaron-transformed total density matrix. However, the polaron transformation operator and σ_x (σ_y) do not commute, thus the off-diagonal terms cannot be obtained exactly. This problem can be solved by using the Born approximation $\rho_{\text{tot}}'(t) \approx \rho_s'(t) \otimes \rho_b'$, which has already been used in deriving the PTRE. The polaron transformation reduces the system–bath coupling, thus makes the factorization of the density matrix in the polaron frame reasonable. Therefore, we have

$$\langle \sigma_{x,y}(t) \rangle = \text{Tr}_{s+b}[\rho_{\text{tot}}'(t) e^{-i\sigma_z B/2} \sigma_{x,y} e^{i\sigma_z B/2}] \approx \kappa \text{Tr}_s[\rho_s'(t) \sigma_{x,y}]. \quad (\text{A8})$$

Together with equations (A2) and (A3), it is straightforwardly to obtain

$$\langle \sigma_z(t) \rangle = \cos \theta \langle \tau_z(t) \rangle + \sin \theta \langle \tau_x(t) \rangle, \quad (\text{A9})$$

$$\langle \sigma_x(t) \rangle = \kappa \sin \theta \langle \tau_z(t) \rangle - \kappa \cos \theta \langle \tau_x(t) \rangle, \quad (\text{A10})$$

$$\langle \sigma_y(t) \rangle = -\kappa \langle \tau_y(t) \rangle \quad (\text{A11})$$

following which the expression for the Liouville operator \mathcal{L}_v of the TLS is derived.

Appendix B. Weak and strong coupling limits of PTRE

In this appendix, we would like to show that the PTRE in the weak (strong) coupling limit is exactly consistence with the Redfield equation (rate equation based on the Fermi's golden rule). In the weak coupling limit, we have $\kappa \approx 1$, thus the polaron basis $|\pm(\Delta_\kappa)\rangle$ approaches the eigenbasis of the TLS $|\pm(\Delta_0)\rangle$, where $\Delta_0 = \sqrt{\epsilon^2 + J^2}$. In this eigen frame, the PTRE equation (15) with secular approximation is reduced to the Redfield equation

$$\frac{d}{dt}[\rho_s]_{++} = -\Gamma[1 + n(\Delta_0)][\rho_s]_{++} + \Gamma n(\Delta_0)[\rho_s]_{--}, \quad (\text{B1})$$

$$\frac{d}{dt}[\rho_s]_{+-} = -\left[i\Delta + \frac{1}{2}\Gamma(1 + 2n(\Delta_0)) \right][\rho_s]_{+-}, \quad (\text{B2})$$

where $\Gamma = \frac{1}{2}J(\Delta_0)\sin^2\theta$.

In the strong coupling limit, the coherence is quickly destroyed by dissipation, thus we only need to consider the equations for the populations. Additionally, as $\kappa \approx 0$ with large α , the eigenbasis of \tilde{H}_0 are reduced to the local basis $|1\rangle$ and $|2\rangle$. As a result, equation (15) becomes a kinetic equation governing the populations $P_i \equiv [\rho_s]_{ii}$, which can be written as

$$\frac{d}{dt}P_1 = -\Gamma_{12}P_1 + \Gamma_{21}P_2, \quad (\text{B3})$$

where

$$\Gamma_{12} = \frac{1}{2}\kappa^2J^2 \int_0^\infty d\tau \Re[e^{i\epsilon\tau}(e^{Q(\tau)} - 1)], \quad (\text{B4})$$

$$\Gamma_{21} = \frac{1}{2}\kappa^2J^2 \int_0^\infty d\tau \Re[e^{-i\epsilon\tau}(e^{Q(\tau)} - 1)], \quad (\text{B5})$$

with

$$Q(\tau) = \int_0^\infty d\omega \frac{J(\omega)}{\pi\omega^2} [\cos(\omega\tau) \coth(\beta_v\omega/2) - i \sin(\omega\tau)]. \quad (\text{B6})$$

The above transition rates Γ_{12} and Γ_{21} are the same as those obtained from the Fermi's golden rule. In a word, the PTRE smoothly connects the weak and strong coupling limits, and provides a useful tool to study the intermediate coupling region where there is usually no reliable approximation methods.

Furthermore, following from equation (B3) the three-level system in the strong coupling limit can be understood from the perspective of population kinetics. The population transitions rate from state $|i\rangle$ to $|j\rangle$ is denoted by Γ_{ij} , then the net population flux from $|i\rangle$ to $|j\rangle$ is $\Gamma_{ij}P_i - \Gamma_{ji}P_j$. In the steady state, the net population fluxes between each two local states must be equal with each other due to population conservation, which means there is a circulation F in the three-level system:

$$F = \Gamma_{12}P_1 - \Gamma_{21}P_2 = \Gamma_{20}P_2 - \Gamma_{02}P_0 = \Gamma_{01}P_0 - \Gamma_{10}P_1. \quad (\text{B7})$$

Then the energy flux from $|i\rangle$ to $|j\rangle$ is just the population flux F times the corresponding energy gap, $\mathcal{J}_{i \rightarrow j} = F(\epsilon_i - \epsilon_j)$, which directly leads to the efficiency $\eta_0 = \epsilon_2/\epsilon_1$. With straightforward calculation, we obtain the steady state population $P_i = D_i/D$ from the kinetic equation (B7), where

$$D_1 = \Gamma_{01}\Gamma_{20} + \Gamma_{02}\Gamma_{21} + \Gamma_{21}\Gamma_{01}, \quad (\text{B8})$$

$$D_2 = \Gamma_{02}\Gamma_{10} + \Gamma_{01}\Gamma_{12} + \Gamma_{12}\Gamma_{02}, \quad (\text{B9})$$

$$D_0 = \Gamma_{10}\Gamma_{20} + \Gamma_{20}\Gamma_{12} + \Gamma_{21}\Gamma_{10}, \quad (\text{B10})$$

$$D = D_1 + D_2 + D_0. \quad (\text{B11})$$

In the case of low temperature trapping bath, the transition rate Γ_{02} can be neglected comparing with Γ_{20} . Then we have $D_1 \approx \Gamma_{01}(\Gamma_{20} + \Gamma_{21})$ and $D_2 \approx \Gamma_{01}\Gamma_{12}$, then the population inversion $P_1 > P_2$ requires $\Gamma_{20} + \Gamma_{21} - \Gamma_{12} > 0$. In the strong coupling limit, the transition rates between the two excited states are almost the same $\Gamma_{12} \approx \Gamma_{21}$, thus $P_1 - P_2 \approx \Gamma_{01}\Gamma_{20}/D > 0$ is established, which is consistent with the results obtained from the PTRE.

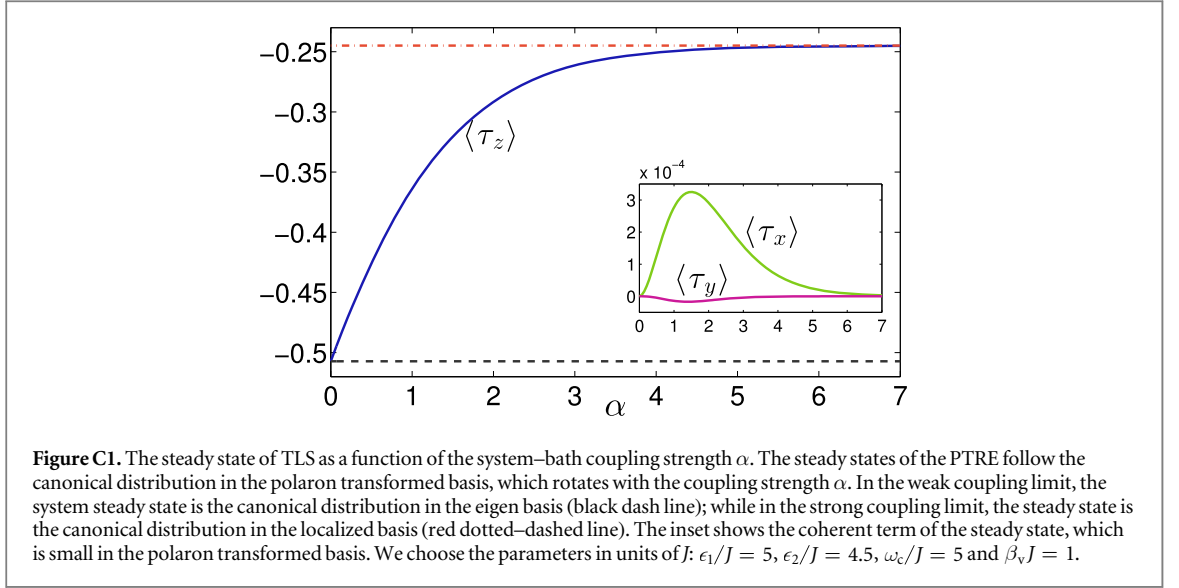
Appendix C. Steady state of the TLS in polaron frame

For convenience, we rewrite equation (15) in the form of the Bloch equation

$$\frac{d}{dt}\langle \vec{\tau}(t) \rangle = -M\langle \vec{\tau}(t) \rangle + \vec{C}. \quad (\text{C1})$$

Here $\langle \vec{\tau}(t) \rangle^T = [\langle \tau_z(t) \rangle, \langle \tau_x(t) \rangle, \langle \tau_y(t) \rangle]$. The transition matrix M and the constant term $\vec{C}^T = (C_z, C_x, C_y)$ are

$$M = \begin{pmatrix} \gamma_z & \gamma_{zx} & 0 \\ \gamma_{xz} & \gamma_x & \Delta_\kappa + \gamma_{xy} \\ \gamma_{yz} & -\Delta_\kappa + \gamma_{yx} & \gamma_y \end{pmatrix}, \quad (\text{C2})$$



$$\vec{C}^T = (C_z, C_x, C_y), \quad (\text{C3})$$

the expressions of the matrix elements are given in appendix D.

The time evolution of $\langle \vec{\tau}(t) \rangle$ is straightforwardly given by

$$\langle \vec{\tau}(t) \rangle = e^{-Mt} [\langle \vec{\tau}(0) \rangle - M^{-1}\vec{C}] + M^{-1}\vec{C}, \quad (\text{C4})$$

with the steady state $\langle \vec{\tau}(\infty) \rangle = M^{-1}\vec{C}$. In the following we will neglect time argument ∞ when referring to the steady state for convenience. The population difference $\langle \tau_z \rangle$ varies with the coupling strength as shown in figure C1. In the weak coupling limit, the TLS steady state distribution is canonical in the eigenbasis, i.e.,

$$\lim_{\alpha \rightarrow 0} \langle \tau_z \rangle = -\tanh\left(\frac{1}{2}\beta_v \Delta_0\right), \quad (\text{C5})$$

which is just the thermodynamic equilibrium state. When the system–bath coupling gradually increases, the system distribution deviates from ρ_e^{can} and follows the Boltzmann distribution

$$\langle \tau_z \rangle = -\tanh\left(\frac{1}{2}\beta_v \Delta_\kappa\right), \quad (\text{C6})$$

with respect to the energy gap Δ_κ between the eigenvalues of $|+\rangle$ and $|-\rangle$ in the polaron frame. Furthermore, when goes into the strong coupling limit, we have

$$\lim_{\alpha \rightarrow \infty} \langle \tau_z \rangle = -\tanh\left(\frac{1}{2}\beta_v \epsilon\right), \quad (\text{C7})$$

which is the Boltzmann distribution with respect to the local site energies ϵ_1 and ϵ_2 . The deviation from the canonical state ρ_s^{can} due to the strong system–bath coupling has been studied via the cumulant expansion method in the polaron-transformed thermodynamic distribution [20, 21] and from the view point of energy shell deformation [18, 19, 22].

Appendix D. Elements of the matrixes M and \vec{M}

The quantities defined in equations (C2) and (C3) are determined by the superposition of the correlation functions equation (A4) following from equations (15) and (C1). By defining the functions

$$f(t) = \cosh[Q(t)] + \cosh[Q(-t)] - 2, \quad (\text{D1})$$

$$g(t) = \sinh[Q(t)] + \sinh[Q(-t)], \quad (\text{D2})$$

it is straightforwardly to obtain

$$\gamma_z = \frac{1}{2}\kappa^2 J^2 \int_0^\infty dt \cos(\Delta_\kappa t) [f(t) \cos^2 \theta + g(t)], \quad (\text{D3})$$

$$\gamma_x = \frac{1}{2}\kappa^2 J^2 \int_0^\infty dt [f(t) \sin^2 \theta + \cos(\Delta_\kappa t) g(t)], \quad (\text{D4})$$

$$\gamma_y = \frac{1}{2}\kappa^2 J^2 \int_0^\infty dt f(t) [\cos^2 \theta \cos(\Delta_\kappa t) + \sin^2 \theta], \quad (\text{D5})$$

$$\gamma_{zx} = \frac{1}{4}\kappa^2 J^2 \sin 2\theta \int_0^\infty dt f(t), \quad (\text{D6})$$

$$\gamma_{xz} = \frac{1}{4}\kappa^2 J^2 \sin 2\theta \int_0^\infty dt f(t) \cos(\Delta_\kappa t), \quad (\text{D7})$$

$$\gamma_{xy} = \frac{1}{2}\kappa^2 J^2 \int_0^\infty dt g(t) \sin(\Delta_\kappa t), \quad (\text{D8})$$

$$\gamma_{yx} = -\frac{1}{2}\kappa^2 J^2 \cos^2 \theta \int_0^\infty dt f(t) \sin(\Delta_\kappa t), \quad (\text{D9})$$

$$\gamma_{yz} = \frac{1}{4}\kappa^2 J^2 \sin 2\theta \int_0^\infty dt f(t) \sin(\Delta_\kappa t), \quad (\text{D10})$$

$$C_z = -\frac{i}{2}\kappa^2 J^2 \int_{-\infty}^\infty dt \sin(\Delta_\kappa t) \times [\cos^2 \theta \cosh[Q(t)] + \sinh[Q(t)]], \quad (\text{D11})$$

$$C_x = -\frac{i}{4}\kappa^2 J^2 \sin 2\theta \int_{-\infty}^\infty dt \sin(\Delta_\kappa t) \cosh[Q(t)], \quad (\text{D12})$$

$$C_y = -\frac{i}{4}\kappa^2 J^2 \sin 2\theta \int_0^\infty dt [1 - \cos(\Delta_\kappa t)] \times [\cosh[Q(t)] - \cosh[Q(-t)]]. \quad (\text{D13})$$

The Liouville operator \mathcal{L}_v for the three-level system is obtained from equation (C1) with the expressions given above. Here the relation $\rho_{00} + \rho_{11} + \rho_{22} = 1$ for the three-level system should be used to substitute $[\rho_s]_{11} + [\rho_s]_{22} = 1$ for the TLS. Taking the contributions of the Lindblad terms \mathcal{L}_p and \mathcal{L}_t defined in equation (8) into consideration, the elements of the matrix \bar{M} in equation (18) are

$$\bar{M}_{11} = \gamma_z \cos^2 \theta + \gamma_x \sin^2 \theta + \frac{1}{2}(\gamma_{xz} + \gamma_{zx}) \sin 2\theta + \frac{1}{2}[\gamma_p(n_p + 1) + \gamma_t(n_t + 1)], \quad (\text{D14})$$

$$\bar{M}_{12} = -C_z \cos \theta - C_x \sin \theta + \frac{1}{2}[\gamma_p(3n_p + 1) - \gamma_t(3n_t + 1)], \quad (\text{D15})$$

$$\bar{M}_{13} = \kappa^{-1} \left[\gamma_{xz} \sin^2 \theta - \gamma_{zx} \cos^2 \theta + \frac{1}{2}(\gamma_z - \gamma_x) \sin 2\theta \right], \quad (\text{D16})$$

$$\bar{M}_{14} = -\kappa^{-1}(\Delta_\kappa + \gamma_{xy}) \sin \theta, \quad (\text{D17})$$

$$\bar{M}_{21} = \frac{1}{2}[\gamma_p(n_p + 1) - \gamma_t(n_t + 1)], \quad (\text{D18})$$

$$\bar{M}_{22} = \frac{1}{2}[\gamma_p(3n_p + 1) + \gamma_t(3n_t + 1)], \quad (\text{D19})$$

$$\bar{M}_{23} = \bar{M}_{24} = 0, \quad (\text{D20})$$

$$\bar{M}_{31} = \kappa \left[\gamma_{zx} \sin^2 \theta - \gamma_{xz} \cos^2 \theta + \frac{1}{2}(\gamma_z - \gamma_x) \sin 2\theta \right], \quad (\text{D21})$$

$$\bar{M}_{32} = \kappa(C_x \cos \theta - C_z \sin \theta), \quad (\text{D22})$$

$$\bar{M}_{33} = \gamma_x \cos^2 \theta + \gamma_z \sin^2 \theta - \frac{1}{2}(\gamma_{xz} + \gamma_{zx}) \sin 2\theta + \frac{1}{2}[\gamma_p(n_p + 1) + \gamma_t(n_t + 1)], \quad (\text{D23})$$

$$\bar{M}_{34} = (\Delta_\kappa + \gamma_{xy}) \cos \theta, \quad (\text{D24})$$

$$\bar{M}_{41} = \kappa [(\Delta_\kappa - \gamma_{yx}) \sin \theta - \gamma_{yz} \cos \theta], \quad (\text{D25})$$

$$\bar{M}_{42} = \kappa C_y, \quad (\text{D26})$$

$$\bar{M}_{43} = -(\Delta_\kappa \gamma_{yx}) \cos \theta - \gamma_{yz} \sin \theta, \quad (\text{D27})$$

$$\bar{M}_{44} = \gamma_y + \frac{1}{2}[\gamma_p(n_p + 1) + \gamma_t(n_t + 1)]. \quad (\text{D28})$$

References

- [1] Engel G S, Calhoun T R, Read E L, Ahn T-K, Mancal T, Cheng Y-C, Blankenship R E and Fleming G R 2007 *Nature* **446** 782
- [2] Ishizaki A and Fleming G R 2009 *Proc. Natl Acad. Sci.* **106** 7255
- [3] Cao J and Silbey R J 2009 *J. Phys. Chem. A* **113** 13826
- [4] Tscherbul T V and Brumer P 2014 *Phys. Rev. Lett.* **113** 113601
- [5] Olšna J, Dijkstra A G, Wang C and Cao J 2014 arXiv:1408.5385
- [6] Quan H T, Liu Y X, Sun C P and Nori F 2007 *Phys. Rev. E* **76** 031105
- [7] Scully M O, Chapin K R, Dorfman K E, Kim M B and Svidzinsky A 2011 *Proc. Natl Acad. Sci.* **108** 15097
- [8] Dorfman K E, Voronine D V, Mukamel S and Scully M O 2011 *Proc. Natl Acad. Sci.* **110** 2746
- [9] Scovil H E D and Schulz-DuBois E O 1959 *Phys. Rev. Lett.* **2** 262
- [10] Geusic J E, Schulz-DuBois E O and Scovil H E 1967 *Phys. Rev.* **156** 343
- [11] Geva E and Kosloff R 1996 *J. Chem. Phys.* **104** 7681
- [12] Boukobza E and Tannor D J 2006 *Phys. Rev. A* **74** 063823
- [13] Boukobza E and Tannor D J 2007 *Phys. Rev. Lett.* **98** 240601
- [14] Linden N, Popescu S and Skrzypczyk P 2010 *Phys. Rev. Lett.* **105** 130401
- [15] Levy A and Kosloff R 2012 *Phys. Rev. Lett.* **108** 070604
- [16] Rahav S, Harbola U and Mukamel S 2012 *Phys. Rev. A* **86** 043843
- [17] Correa L A, Palao J P, Alonso D and Adesso G 2014 *Sci. Rep.* **4** 3949
- [18] Dong H, Yang S, Liu X F and Sun C P 2007 *Phys. Rev. A* **76** 044104
- [19] Dong H, Liu X F and Sun C P 2010 *Chin. Sci. Bull.* **55** 3256
- [20] Lee C K, Cao J and Gong J B 2012 *Phys. Rev. E* **86** 021109
- [21] Lee C K, Moix J and Cao J 2012 *J. Chem. Phys.* **136** 204120
- [22] Xu D Z, Li S W, Liu X F and Sun C P 2014 *Phys. Rev. E* **90** 062125
- [23] Grover M and Silbey R J 1971 *J. Chem. Phys.* **54** 4843
- [24] Silbey R J and Harris T 1984 *J. Chem. Phys.* **80** 2615
- [25] Wang C, Ren J and Cao J 2015 *Sci. Rep.* **5** 11787
- [26] Wang C, Ren J and Cao J 2014 *New J. Phys.* **16** 045019
- [27] Zimanyi E N and Silbey R J 2012 *Phil. Trans. R. Soc. A* **370** 3620
- [28] Lee C K, Moix J M and Cao J 2015 *J. Chem. Phys.* **142** 164103
- [29] McCutcheon Dara P S and Nazir A 2011 *J. Chem. Phys.* **135** 114501
- [30] Curzon F and Ahlborn B 1975 *Am. J. Phys.* **43** 22
- [31] Van den Broeck C 2005 *Phys. Rev. Lett.* **95** 190602
- [32] Esposito M, Lindenberg K and Van den Broeck C 2009 *Phys. Rev. Lett.* **102** 130602
- [33] Dijkstra A G, Wang C, Cao J and Fleming G R 2015 *J. Phys. Chem. Lett.* **6** 627
- [34] Caruso F, Chin A W, Datta A, Huelga S F and Plenio M B 2009 *J. Chem. Phys.* **131** 105106
- [35] Rebentrost P, Mohseni M, Kassar I, Lloyd S and Aspuru-Guzik A 2009 *New J. Phys.* **11** 033003
- [36] Wu J L, Liu F, Shen Y, Cao J and Silbey R J 2010 *New J. Phys.* **12** 105012
- [37] Wu J, Silbey R J and Cao J 2013 *Phys. Rev. Lett.* **110** 200402